# Development and Investigation of a High Pulse Rate Planar Inductive Pulsed Plasma Thruster

Curtis L. Promislow

A dissertation
submitted in partial fulfillment of the
requirements for the degree of

Doctor of Philosophy

University of Washington

2024

Reading Committee:
Justin M. Little, Chair
Kurt A. Polzin
Uri Shumlak
Robert Breidenthal

Program Authorized to Offer Degree:
Aeronautics and Astronautics

University of Washington

## Abstract

Development and Investigation of a High Pulse Rate Planar Inductive Pulsed Plasma Thruster

Curtis L. Promislow

Chair of the Supervisory Committee:
Associate Professor Justin M. Little
William E. Boeing Department of Aeronautics and Astronautics

Planar inductive pulsed plasma thrusters promise to offer efficient, high thrust density electric spacecraft propulsion at moderate to high specific impulse. Unlike many other types of electric propulsion, they can be readily throttled while maintaining optimal performance and can operate on a wide range of propellants, including those that are reactive or molecular. A combination of theoretical work and experimental results from other pulsed thrusters has suggested that operation of planar inductive pulsed plasma thrusters at high pulse rates, which are defined here as rates in excess of 1 kHz, could simplify the operation and improve the performance of these devices. To be viable in the near to medium term, however, a high pulse rate planar inductive pulsed plasma thruster would have to operate at much lower discharge energies ($\lesssim 10\,\mathrm{J}$) than previous, lower pulse rate ($\lesssim 10\,\mathrm{Hz}$) designs. To investigate whether efficient thruster operation remained possible at these lower discharge energies, a compact planar inductive pulsed plasma thruster, along with a supporting power processing unit, was built and tested.

A highly modular prototype power processing unit based on a paralleled boost converter design has been developed for recharging the capacitor bank of inductive pulsed plasma thrusters operating at pulse rates of 1 kHz to 10 kHz. Operation at these rates, which are one to two orders of magnitude higher than in previous designs, has been hypothesized to allow for efficient quasi-steady thruster operation while also improving lifetime and reliability. Benchtop testing of a prototype unit has demonstrated successful operation at pulse rates from 1 kHz to 10 kHz, voltage gain as high as 25.5, power handling of 1 kW to 9.1 kW, and electrical efficiency up to 70%. Quasi-steady operation has been achieved up to 20 pulses and the design has been shown to maintain functionality in the event of a simulated component failure. Theoretical and circuit simulator models of the prototype were developed and leveraged to identify the dominant loss mechanisms. The efficiency was determined to be primarily constrained by high switching losses, which were estimated to account for over 70% of total unit losses in the cases investigated. Scaling laws for the efficiency of the design were developed using simple linearized circuit equations and indicated thruster performance was primarily dependent on the ratio of the input and output voltages, the inductive recapture ratio of the thruster, and ratios of the relevant charging and switching timescales.

The evolution of the current sheet is fundamental to the understanding and operation of planar inductive pulsed plasma thrusters. Methods for experimentally determining the time-varying mutual inductance and plasma resistance associated with the current sheet are presented. From these, time-histories of the resistive heating in and electromagnetic acceleration of the sheet are found. Analysis of experimental data obtained from a compact, low discharge energy inductive pulsed plasma thruster shows that current sheet evolution is well described by three phases: ionization, formation, and acceleration. Evidence is provided for the plasma current and resistive heating becoming localized near the upstream edge of the current sheet as the sheet forms. The influence of initial propellant density and pre-ionization on the characteristics of the sheet are examined. Both higher propellant densities and increased pre-ionization are found to produce current sheets which exhibit greater magnetic impermeability. Higher densities cause the sheet to form closer to the coil face, improving coupling, while stronger pre-ionization leads to more rapid resistive heating, causing the sheet to form earlier in time.

Formation of a well-defined, magnetically impermeable current sheet is central to the operation of planar inductive pulsed plasma thrusters. Existing scaling laws for these devices, however, are primarily derived from models that either overlook or greatly simplify the current sheet formation process. Data obtained from a compact, low discharge energy planar inductive pulsed plasma thruster were used to gain insight into the fundamental physics governing current sheet formation in these devices. It was found that maximum inductive coupling and current density in the sheet scaled with the ratio of the resistive diffusion to ionization timescales. The ratio of these timescales was shown to describe the combined role of diffusion and ionization in influencing the electron population within the current sheet. When the ionization timescale was fast relative to the diffusive timescale, the thruster discharge was found to be much more effective at concentrating current in the sheet. A connection between the strength of the current sheet and the thruster design and operational parameters was also established and used to explore the parameter space over which efficient thruster operation was possible. Evidence was found that it was difficult to form a magnetically impermeable current sheet at low discharge energies and mass bits, which strongly suggests that the process of current sheet formation cannot be neglected when investigating the performance of planar inductive pulsed plasma thrusters operating in this parameter space.

# TABLE OF CONTENTS

# LIST OF FIGURES

# LIST OF TABLES

# ACKNOWLEDGMENTS

At this time I would like to acknowledge the numerous people who have made this dissertation possible and whom I've had the pleasure of knowing over my years in graduate school. First and foremost, I would like to thank my advisor, Justin Little. What a journey it has been. From that first phone interview to the late nights at MSNW to the founding of the SPACE lab to building the lab from the ground up, and now, far too many years later, here we are. It has been a privilege to not only be one of your first students but to have watched your parallel journey firsthand. Your guidance over these years has been invaluable and has helped me grow both as an academic and as a person. Your understanding, patience, and kindness throughout my various struggles have not gone unnoticed. Thank you for believing in me from the beginning and throughout my time here in your lab, perhaps most of all when I was not sure I believed in myself.

To my labmates and fellow students throughout the years, it has been a joy to share this experience with you all. To Peter "Ski-ter" Thoreau, I could not have asked for a better friend and colleague with whom to share my time in graduate school. From the adventures to the shenanigans, the ski tours to the backyard pizza nights, it's been quite the ride. To Jared "That goes" Smythe, your friendship these past few years has been something I'm truly grateful for. To my fellow SPACE Lab pre-founding members Charlie "Yung Viz" Kelly and Anna "Volume to 11" Sheppard: I'm proud to say we've all made it out! Charlie, I think I still owe you a muffin. And thanks for going easy on me with those vocabulary quizzes. Anna, thanks for blabbing to Justin about me after the visit day; I probably wouldn't have made it here otherwise. And thanks for introducing me to the UW A&A grad community when I was a fledgling graduate student. To the PIT crew: Arvindh Sharma, Gordon McCulloh, and Cameron Marsh, it was a pleasure working with you all to advance inductive pulsed plasma thrusters. Thanks in particular to Cameron for his assistance in constructing many of the diagnostics used to collect the data presented in this dissertation.

To all the fantastic teachers and mentors I've been fortunate enough to encounter, I wouldn't be where I am today without your guidance. To Uri Shumlak, thank you for my first introduction to the world of plasma physics and for stepping in as my temporary advisor during the transition period between labs. To Kurt Polzin and Adam Martin, thank you both for your mentorship and support during my time at NASA Marshall Spaceflight Center and for making my internships there such wonderful experiences. And thank you as well for the many insightful conversations on inductive pulsed plasma thrusters. You two are truly the giants on whose shoulders I have stood.

To my family and friends outside of grad school, I am forever grateful for your continued support. To my mom and dad, thanks for all you have done to allow me the opportunity to pursue my academic ambitions. To my sister, thanks for all the long phone conversations when I needed someone to talk to. To the Seattle West Coast Swing community, thanks for all the dances and for helping me stay sane these last couple of years.

Finally, I would like to thank the various funding sources that made my graduate school journey financially possible. First, I would like to thank NASA Marshall Spaceflight Center for funding for power processing unit development under Collaborative Agreement Notice No. 80MSFC18N0002. Thanks in particular to Dr. Kurt Polzin and Dr. Adam Martin for managing the project on the NASA side of the collaboration and for their input and assistance during the design and testing process. Second, I thank the Department of Defense Defense Innovation Unit for supporting part of this work under contract 000-002-SOW-001-A, Funding Action no. FA211606, and Avalanche Energy and Park Cover for management of this contract. And third, I thank the Defense Advanced Research Projects Agency (DARPA) for supporting parts of this work under Agreement No. HR00112490390A and Dr. Susan

Swithenbank for managing this contract.

# Chapter 1

# INTRODUCTION

Electric propulsion (EP) is a type of spacecraft propulsion wherein electrical energy is used to accelerate a propellant that is expelled from the craft to produce thrust[1, 2]. Inductive Pulsed Plasma Thrusters (IPPTs) are a sub-class of electromagnetic EP devices that ionize a propellant substance into a plasma and then inductively accelerate this plasma to high velocities to produce thrust[3]. IPPTs are distinguished from other electromagnetic devices in that they require no electrodes in direct contact with the plasma and in that the plasma generation and acceleration processes occur in discrete pulses rather than continuously. Figure 1.1 provides a simplified hierarchical diagram of where IPPTs fit in the context of EP.

Generally speaking, most IPPTs are based around the following three primary components: an inductive coil through which current is driven to produce strong, time-varying electromagnetic fields; a capacitor bank for storing and rapidly discharging electrical energy; and a switching mechanism that controls the connection between the capacitor bank and inductive coil. Since IPPTs operate on the principle of induced fields, their operation is fundamentally due to a combination of Ampere's and Faraday's laws, which are expressed in differential form as:

$$\nabla \times \vec{B} = \mu_0 \vec{J} \tag{1.1a}$$

$$\nabla \times \vec{E} = -\frac{\partial \vec{B}}{\partial t} \tag{1.1b}$$

Here, $\vec{E}$ and $\vec{B}$ are the electric and magnetic field vectors, respectively, $\vec{J}$ is the current density, and $\mu_0$ is the permeability of free space. From Equation (1.1a), we observe that a current density necessitates the existence of an orthogonal magnetic field. If this current

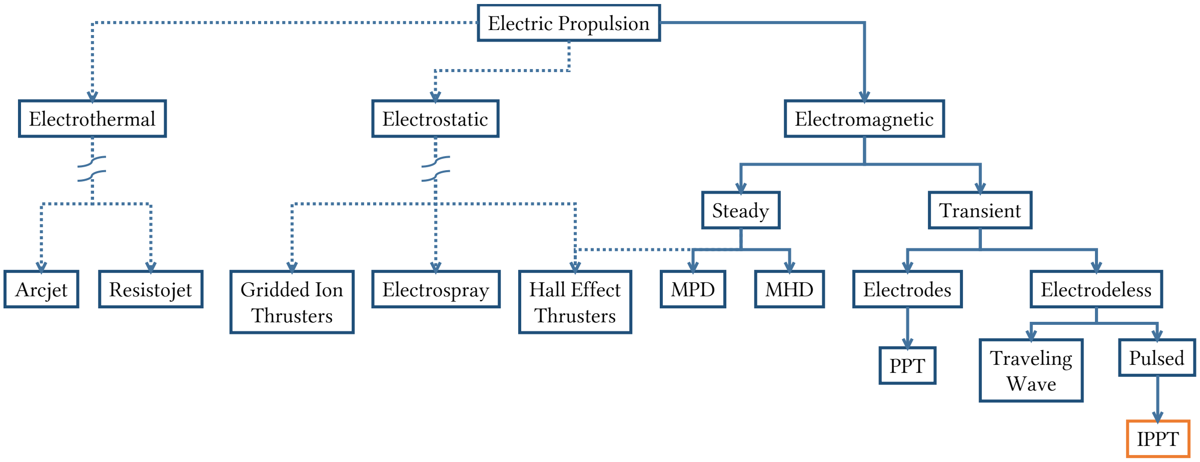

**Figure 1.1:** Simplified hierarchical diagram illustrating where IPPTs fall in the broader taxonomy of EP.

density varies rapidly with time, Equation (1.1b) shows that a time-dependent electric field in the direction opposite the current density will result. Any conductive body subjected to this electric field will then develop a current in the direction opposite to the original $\vec{J}$. An alternative but equivalent way of understanding this phenomenon is provided by Lenz's law, which describes how the current induced in a conductor subjected to a time-varying magnetic field opposes the change in magnetic flux through the conductor.

A wide range of IPPT designs may be found in the literature[3]. At a high level, IPPT designs may be classified by whether the magnetic flux produced by the plasma currents is open or closed/self-contained. Figure 1.2 shows diagrams of the three most studied configurations. These are, from left to right, the planar, conical, and field reverse configuration (FRC) devices. Planar and conical IPPTs are both considered open flux devices, while the current in FRC IPPTs forms self-contained, closed field lines. While there are potential merits to each design, this dissertation focuses on planar IPPTs (see Figure 1.2(a)), wherein the inductive drive coil is more or less contained in a flat plane.

The operation of a planar IPPT over the course of a single pulse is illustrated in Figure 1.3. In this diagram, $C$ is the capacitor bank, $S$ is the switch, and $L_c$ is the inductive drive coil

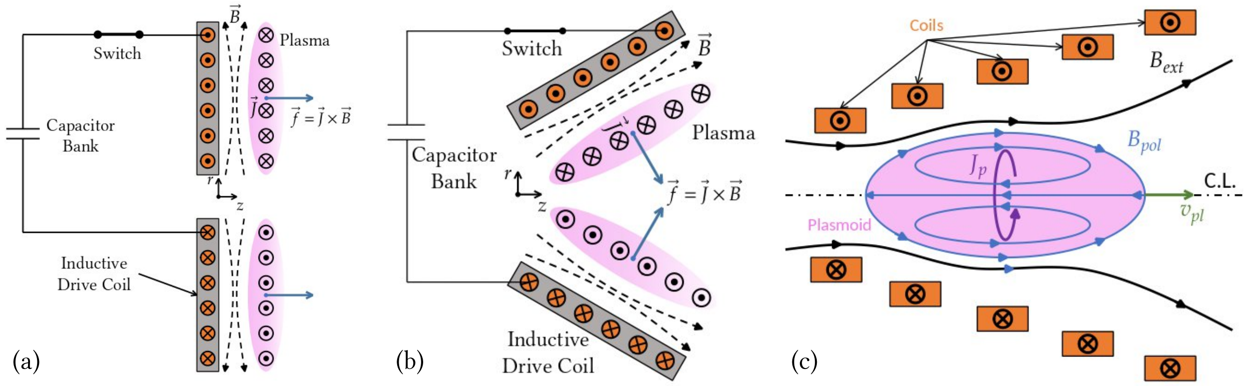

**Figure 1.2:** Simplified diagrams showing three of the most studied IPPT configurations: (a) planar, (b) conical, and (c) FRC IPPTs.

(in orange), represented here as an idealized simple flat planar spiral. $I_c$ is the time-varying current that flows through the drive circuit once the capacitor has been connected to the drive coil. Areas in gray are meant to represent dielectric material.

First, propellant, usually a neutral gas, is injected over the region above the inductive drive coil. This is shown in Figure 1.3(a), where we have ignored for simplicity the specifics of how said propellant injection is actually accomplished. Ideally, the distribution of propellant over the coil face is radially and azimuthally uniform. Additionally, it should be axially contained within the electromagnetic decoupling distance, $z_{dc}$. This distance represents the characteristic length scale over which the drive coil can electromagnetically interact with and accelerate the propellant. Before any acceleration can occur, however, the propellant must be broken down and ionized into a plasma (Figure 1.3(b)). This is often primarily accomplished by the azimuthal electric field induced in the initial stages of the discharge but can be aided by an external device.

The inductive acceleration process for the case of an IPPT with a planar spiral coil is shown in Figure 1.3(c). When the switch closes and connects the capacitor to the coil, a time-varying current is driven through the coil. This produces an azimuthal current density, $J_\theta$,

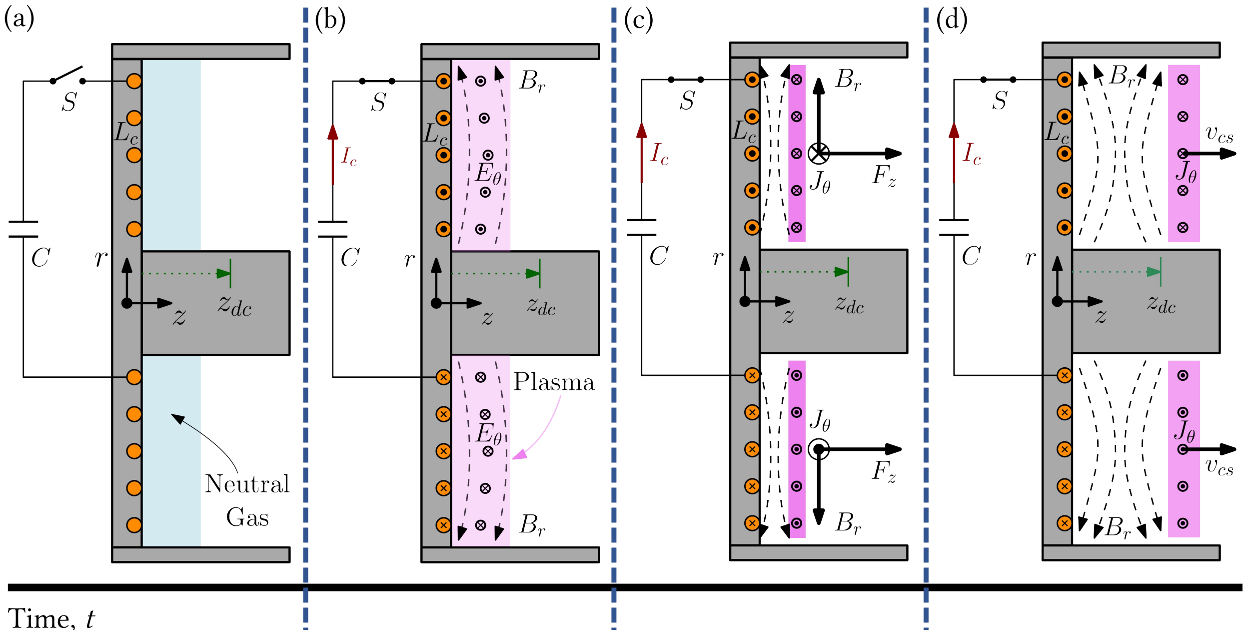

**Figure 1.3:** Diagram of a planar IPPT illustrating simplified, idealized operation of the device for a single pulse. Shown are (a) propellant injection, (b) propellant ionization, (c) current sheet formation and acceleration, and (c) current sheet detachment.

and, accordingly, a radially directed, time-varying magnetic field, $B_r$, in the region between the coil and plasma. As a consequence of Equation (1.1b), an azimuthal electric field, $E_\theta$, will then be produced in response to this $B_r$. Assuming the plasma is close enough to the coil face, this induced electric field will drive a $J_\theta$ in the plasma in the direction opposite to the current in the inductive coil. Ideally, $J_\theta$ becomes concentrated in a thin layer of plasma known as a "current sheet".

The generation of thrust may be explained in several equivalent ways. First, it may be said that the counter-rotating currents in the coil and plasma repel each other electromagnetically, resulting in thrust. Another interpretation is that growing $B_r$ increases the magnetic pressure in the region between the coil and plasma, pushing the plasma away from the thruster. Finally, one can reference the so-called "$\vec{J} \times \vec{B}$" force. This is a mathematical description of how charged particles in the plasma accelerated in the azimuthal (or anti-azimuthal) direction by $E_\theta$ are redirected in the axial direction by the presence of $B_r$.

Eventually, the current sheet from the drive coil moves beyond $z_{dc}$ and decouples from the drive coil (Figure 1.3(c)). At this stage, the force on the current sheet is relatively small, and the sheet continues its axial motion until it eventually exits the device. Assuming there are not a significant number of downstream particles, the velocity of the current sheet, $v_{cs}$, at this point is largely constant and represents the characteristic exit velocity of the thruster. After the current sheet exits the thruster, the cycle is considered complete. While Figure 1.3 depicts a single pulse, the process shown may be repeated as frequently as the gas injection and drive circuit allow.

## *1.1 Motivation*

R. G. Jahn consolidated many of the challenges inherent in the operation of pulsed electromagnetic EP devices in his seminal book on the physics of EP[1]. In this work, Jahn also identified two challenges that are unique to IPPTs. For one, the drive circuitry used to generate the time-varying current in the inductive coil does not require the presence of a plasma to be complete. In the absence of a plasma, the energy stored in the capacitor bank is either lost via Ohmic heating in the drive circuit resistance or is radiated away. It is therefore critical that the plasma be formed rapidly after the switch, $S$, is closed.

Complicating matters further is the nature of the inductive coupling between the plasma and drive coil. Fundamentally, the coupling of two current loops is a function of the mutual inductance between them, which, in turn, is a strong inverse function of the distance between the loops. As the plasma is accelerated, the distance between it and the drive coil is increased, and the electromagnetic coupling between the plasma and drive coil current loops is weakened. As such, efficient IPPT operation requires that most of the energy transfer between the drive circuit and plasma occur while the plasma is as close to the drive coil as possible.

Jahn also listed a series of events that must occur during each cycle for efficient operation of pulsed EP devices. Drawing heavily from this list and using basic first principles arguments, we construct a similar list for planar IPPTs:

1. Sufficient electrical energy must be stored to drive the required current and at the required rate. The storage device must be capable of delivering the stored energy with minimal losses and great speed.
2. Propellant must be injected in a manner that leads to an optimal distribution over the face of the coil. Propellant injection must be well timed with the initiation of the electrical discharge such that significant mass is not lost before or after the discharge and mass utilization remains high.
3. Breakdown of the propellant must occur rapidly and result in plasma that remains close to the drive coil. The energy used to ionize the propellant must be small relative to the total stored energy.
4. Following gas breakdown and initial plasma formation, the plasma must be rapidly organized into a well-formed current sheet free of significant instabilities. This sheet should form close to the drive coil and should be magnetically impermeable. The current sheet should also not dissipate excessive energy as heat, since we require the dominant acceleration mechanism to be electromagnetic.
5. The mass utilization of the current sheet should remain high. This requires either that most of the injected propellant participate in sheet formation or that the sheet is able to effectively push or entrain any downstream propellant as it translates.
6. The sheet must be ejected with minimal thermal, i.e., frozen flow, and electromagnetic losses. Moreover, the dynamical efficiency of the ejection process should be high. For example, during ejection, the plasma should not strongly diverge or be tied to the magnetic field lines.
7. The cycle should complete in sufficient time that it does not adversely affect the dynamics of later pulses. Any significant excess electrical energy not used in the acceleration of the plasma should be recaptured for use in the next cycle.

It is evident even from the abridged list above that the requirements for efficient IPPT operation are numerous and complex. One may reasonably wonder why we should bother to develop such devices at all, especially when other types of EP devices, e.g., Hall and gridded ion thrusters, have already demonstrated thrust efficiencies in excess of 60%[2]. To motivate the development of IPPTs, we begin by considering the advantages of electromagnetic over electrothermal and electrostatic EP devices. In a continuum perspective, the electromagnetic body force responsible for thrust in electromagnetic EP devices, i.e., the $\vec{v} \times \vec{B}$ term of the Lorentz force, becomes a $\vec{J} \times \vec{B}$ force density. When the magnetic field is due primarily to the plasma current, the force density is found to scale roughly as $J^2$. This scaling points towards one of the main draws of electromagnetic devices: high thrust density, particularly at high power and propellant mass flow rates.

Because electromagnetic devices accelerate the plasma directly using electromagnetic body forces, high $I_{sp}$ may be achieved without the extreme temperatures and the associated materials challenges found in electrothermal thrusters. Moreover, the plasma in electromagnetic devices can be accelerated in a quasi-neutral fashion, which avoids the space charge limitations on thrust density found in purely electrostatic devices. This quasi-neutral acceleration also precludes the need for a separate neutralizer, such as a hollow cathode.

Having laid out the appeal of electromagnetic devices in general, we now turn to a discussion of the merits of pulsed electromagnetic devices over their steady-state counterparts. Drawing again from Jahn, three potential advantages of pulsed devices are as follows:

1. The observed $J^2$ scaling of thrust for self-field devices suggests that, for the same average current, a pulsed device may be able to achieve higher average thrust. In addition, data has suggested that the efficiency of electromagnetic devices scales with the current density[1]. Hence it stands to reason that pulsed devices may be able to achieve higher thrust to power ratios and overall thrust efficiencies than steady-state devices.

2. If the pulse is sufficiently fast, the electrons may not have time to reach thermal

equilibrium with the ions. This could improve device efficiency by reducing energy losses due to inelastic collisions (e.g. ionization), radiation, and frozen flow losses. This may also reduce the heat flux to plasma-facing surfaces, thereby alleviating cooling and materials requirements.

3. Certain transient electromagnetic effects only seen in pulsed devices may prove beneficial for device operation. One such example, as noted by Jahn, is the skin effect, wherein current becomes concentrated in a thin layer of plasma due to opposing eddy currents within the plasma. In addition to potentially improving the coupling between the accelerating fields and plasma, this could also lead to an increase in the current density and, by extension, device efficiency.

An additional advantage of pulsed devices not explicitly commented on by Jahn is also worth mentioning. Because the performance of pulsed thrusters is largely dependent on the intra-pulse dynamics, constant specific impulse, $I_{sp}$, and thrust efficiency, $\eta_t$, may thus be achieved over a wide range of input power levels by simply adjusting the pulse rate. This means that pulsed devices, in principle, are able to throttle both thrust and power consumption while maintaining optimal or near-optimal performance. We note that this holds only so long as the pulses may be assumed to not significantly interact with each other and that the pulse rate is not constrained by other operational requirements. In addition, the degree of throttle-ability will depend on the range over which the pulse rate may be varied, with a wider range of pulse rates increasing the available range of thrust and power. This unique attribute could make pulsed EP systems compatible with a wide variety of spacecraft and also enables significant mission flexibility.

Finally, the inductive nature of IPPTs offers some potential advantages over other pulsed devices. Inductive plasma formation and acceleration eliminate the need for electrodes in direct contact with the plasma. This allows for fully "electrodeless" operation, which eliminates thruster lifetime issues associated with electrode erosion. Electrodeless operation also affords greater flexibility in regards to propellant selection since there are no concerns about the compatibility of the electrode material and propellant or plasma. This makes electrodeless thrusters ideal for missions that aim to leverage multi-mode[4] or in-situ resource utilization[5] with molecular or reactive propellants. Electrodeless thrusters are also well suited for air-breathing EP[6][7], since oxidation of the electrodes is no longer of concern.

In summary, IPPTs promise to offer efficient, high thrust density EP at moderate to high specific impulse. Their pulsed nature grants them potential advantages in thrust density and efficiency over steady-state electromagnetic EP devices, while also enabling significant mission flexibility. In addition, their lack of electrodes makes them compatible with a wide range of propellants, making IPPTs well-suited for in-situ resource utilization, multi-mode propulsion, and air-breathing EP. Thus, despite their inherent complexities, the unique benefits of IPPTs present a strong case for their development.

## *1.2 Review of Previous Work*

We now briefly examine a selection of relevant previous IPPT research and development efforts in order to contextualize the work presented in this thesis. For a more complete review of IPPT development efforts, both planar and otherwise, the reader is directed to work by Polzin[8] and Polzin et al.[3].

### *1.2.1 Experimental*

Early work on planar IPPTs largely focused on understanding the internal structure of the current sheet as well as the mechanisms by which it was accelerated[9, 10, 11]. Applying a generalized Ohm's law interpretation to their data, Dailey and Lovberg concluded that the measured azimuthal current density in their device was carried solely by the electrons. They asserted that the azimuthal force on the ions due to the induced $E_\theta$ was counteracted by a collisional drag force resulting from interaction with the current carrying electrons and that, as a result, the ions were not accelerated downstream by a $J_\theta B_r$ force. Instead, they found that the forward (downstream) region of the current sheet contained a large electron current density that, when accelerated by $J_\theta B_r$, resulted in an axial polarization electric

**Table 1.1:** Nominal operational parameters and performance metrics for selected IPPTs.

| Thruster | $d_{\text{coil}}$ [cm] | $L_{\text{coil}}$ [nH] | $C_{mb}$ [µF] | $V_0$ [kV] | $E_0$ [J] | $I_{sp}$ [s] | $\eta_t$ [%] | Ref. |
|---|---|---|---|---|---|---|---|---|
| Dailey 10 | 10 | 127 | 2.64 | 10 | 132 | - | - | [10] |
| Dailey 20 | 20 | 460 | 1.75, 3.9 | 12 | 126, 285 | 1500 | 10 | [12] |
| Dailey 30 | 30 | 680 | 6 | 12 | 675 | 500-1500 | 4-18 | [13] |
| PIT MK I | 100 | 770 | 10, 20 | 20 | 2000, 4000 | 1000-2700 | 15-32 | [14] |
| PIT MK Va | 100 | 680 | 9 | 30 | 4000 | 3000-7000 | 30-58 | [15] |
| FARAD | 20 | 20 | 39.2 | 2 | 78.5 | - | - | [16] |
| MSFC | 27 | 705 | 10 | 3 | 20 | - | - | [17] |

field, $E_z$, due to charge separation from the ions. This axial electric field was then claimed to be responsible for acceleration of the ions, which were found to accelerate to the sheet velocity and concentrate in a thin mass layer near the center of the sheet. The axial electron pressure gradient was determined to contribute to the strength of $E_z$ near the leading edge and counteract the $J_\theta B_r$ force at the trailing edge of the sheet.

Initial performance measurements of planar IPPTs were conducted using a 20 cm and 30 cm device[12, 13]. Static fill results showed that the 30 cm device achieved a thrust efficiency of 17% at an $I_{sp}$ of 1430 s, outperforming the 20 cm device. Experiments performed with pulsed gas injection showed decreased performance relative to the static fill cases. This was attributed to the gas distribution over the coil face being less uniform which in turn led to a weaker, less uniform current sheet being formed in these cases. Additional tests were conducted when using pulsed gas injection to determine the influence of PI on thruster performance. For the practical PI methods tested, no improvement was observed over the case where no PI was used.

Continued development of planar IPPTs by Dailey and Lovberg eventually resulted in the pulsed inductive thruster (PIT) series of devices[8]. Notably, the inductive drive coil of these devices was scaled up to 1 m in order to increase both the coil inductance and the electromagnetic decoupling distance. This design decision appears to have been motivated by theoretical work suggesting that the efficiency of the device scaled with these values[18]. Earlier performance measurements, which showed an increase in performance for the 30 cm IPPT over the 20 cm device, may have also played a role. While the initial PIT MK I version of the device was found to be a significant improvement over the 20 cm and 30 cm devices in terms of performance, the PIT MK Va variant of this device is widely considered the state-of-the-art planar IPPT at the time of writing. This device demonstrated thrust efficiencies in excess of 50% at specific impulses ranging from around 3000 s to 7000 s[15, 3].

From the initial development and testing of the PIT series of devices, it became clear that a well-formed current sheet was a prerequisite for achieving high thruster performance. Several empirical insights were gained regarding the relationship between current sheet formation and the operation of the device. First, it was found that too low of a current rise rate in the discharge circuit, i.e., $dI_c/dt$, resulted in incomplete or non-uniform breakdown of the propellant and prohibited the formation of a strong, well-defined current sheet[14]. The rise rate was maximized by increasing the loop voltage applied to the drive coil as well as keeping the stray inductance in the circuit to a minimum.

Second, the discharge energy was found to affect current sheet formation. Below a certain energy, it was found that it was difficult to consistently form a uniform, magnetically impermeable current sheet[8]. This phenomenon, which was not well understood at the time, may have been related to the observed trends in thrust efficiency with specific energy, i.e., the ratio between the discharge energy and mass bit. Above a certain discharge energy, thrust efficiency was found to be relatively constant across a wide range of specific energies. Below this threshold value, however, thrust efficiency was found to decrease as the specific energy was increased. Moreover, the falloff in performance was found to steepen as the discharge energy was lowered. This suggested a minimum discharge energy for magnetically impermeable current sheet formation and that device scaling to lower discharge energies could not be accomplished by simply reducing the injected propellant mass bit.

Later development of the PIT focused on upgrading the PIT MK Va design to address a number of known shortcomings. In particular, it was known that the spark-gap switches used in the earlier PIT designs eroded over time and would ultimately limit the life of the thruster. To address this issue, work focused on evaluating various solid-state switching replacements. A stack of five silicon-controller rectifiers (SCRs) was demonstrated to successfully conduct the required current at an appropriate current rise rate[19]. Later testing of the SCR stack, however, resulted in the devices failing after only a few pulses[20]. Gate-commutated thyristor (GTO) switches were also investigated in an effort to implement inductive energy recapture. In this mode, the current waveform is interrupted during either the first or second zero-crossing, allowing some of the initial stored energy to be recovered back onto the capacitor bank and improving efficiency. Testing discovered, however, that these devices were not able to interrupt the discharge current at either of the first two zero-crossings during nominal thruster operation[19].

More recent work on planar IPPTs has been performed on devices that are smaller in size and lower in discharge energy. The Faraday accelerator with radio-frequency assisted discharge (FARAD) thruster developed by Polzin and Choueiri [22, 16] used a centrally located RF discharge as a source of PI and relied on an externally applied magnetic field to direct this seed plasma over the coil face. The discharge energies in initial FARAD testing were $\leq 100\,\mathrm{J}$; well below the 4 kJ of the PIT Mk Va. At these discharge energies (and for the selected circuit parameters), it was found that the neutral gas could not be broken down without the aid of the PI system. Measurements confirming the formation of current sheets during FARAD thruster testing indicated that PI could be used to significantly lower the discharge energy and current rise rate required for current sheet formation in an IPPT.

A 27 cm diameter thruster was developed by researchers at NASA's Marshall Space Flight Center to test repetitive operation of IPPT subsystems at moderate jet powers of 1 kW to 5 kW and pulse rates up to 30 Hz[17]. Systems testing included a thyristor-based solid state switch, pulsed gas injection valve, and DC glow discharge PI. While preliminary operation

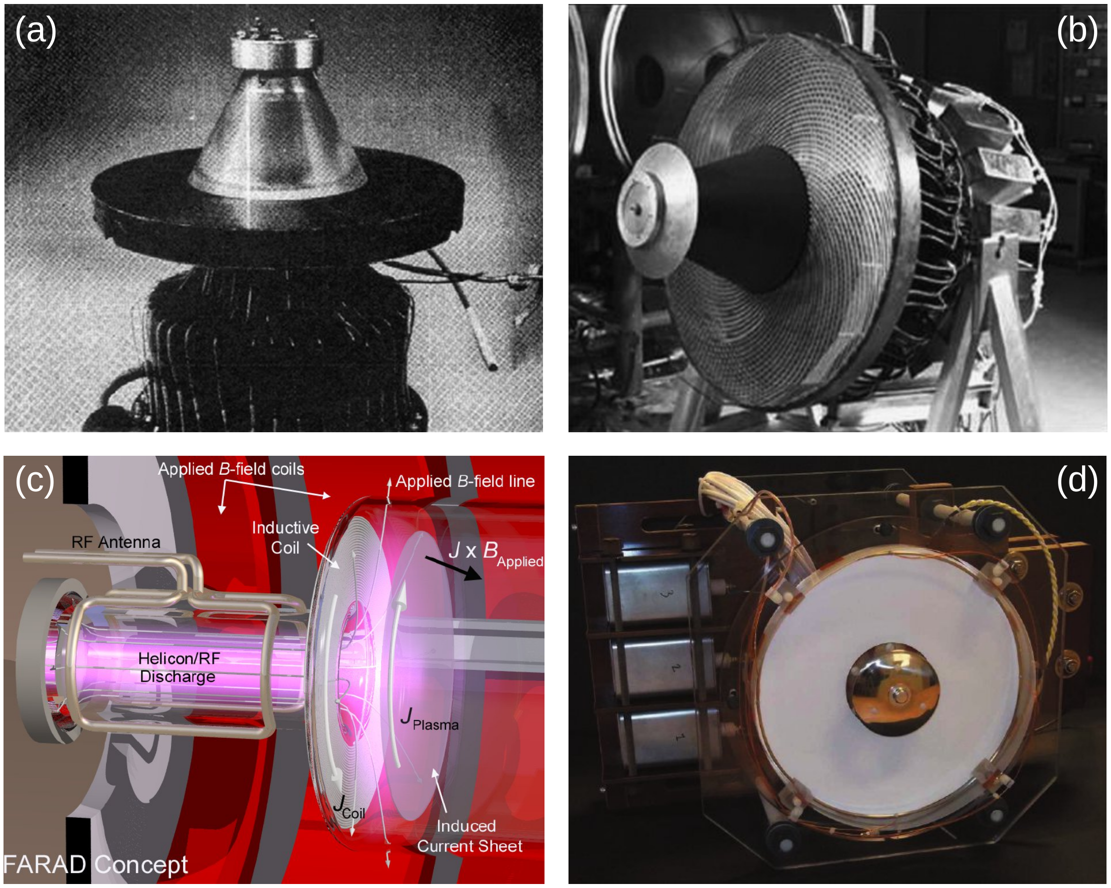

**Figure 1.4:** Images of the (a) 20cm[12], (b) PIT MK V[21], (c) FARAD[16], and (d) MSFC[17] IPPTs.

of the thruster was reported, no detailed plasma diagnostics or thruster performance measurements have been published for this device to date.

A brief summary of the key findings from IPPT experiments thus far is as follows:

1. **Current Sheet Physics:** The azimuthal current density in the sheet, $J_\theta$, is carried predominantly by the electrons and was measured to be largest near the leading (downstream) edge of the current sheet[11]. Axial acceleration of the ions was proposed to be due to the formation of an axial electric field, $E_z$, as a result of charge separation

from the electrons that were axially accelerated via the $J_\theta B_r$ force.

2. **Gas Injection:** The uniformity of the initial gas distribution over the coil face was found to impact the uniformity of the current sheet that was formed. Less uniform current sheets were found to correspond to a decrease in thruster performance.
3. **Current Sheet Formation:** Empirical evidence from the PIT line of devices suggested the existence of a minimum discharge energy and current rise rate required to form a well-defined current sheet that was impermeable to both the accelerating magnetic field and downstream propellant. Work by Polzin[16, 23] indicated that these minimum values could be lowered through the use of PI.
4. **Thruster Performance:** Optimal performance was achieved when the discharge and sheet acceleration timescales were roughly matched. Larger drive coils were found to improve thruster performance due to possessing larger electromagnetic coupling distances.

### *1.2.2 Theoretical Modeling*

A number of theoretical models describing planar IPPT operation have been developed by various authors, ranging from simple 1D models[18] to 2D magnetohydrodynamic (MHD) codes[24, 25, 26]. The most widely used is a lumped-element circuit model coupled to a 1D plasma model that describes the dynamics and evolution of the current sheet. Figure1.5(a) shows the circuit model for the common case of an $RLC$ discharge circuit. Here, $C_{mb}$ is the energy storage capacitor bank, which is connected to the inductive drive coil, $L_c$, by switch $S$. $R_c$ and $L_s$ are the parasitic (or stray) resistance and inductance in the circuit, respectively. The inductive interaction between the discharge circuit and plasma is modeled as a transformer, where the plasma is assumed to posses some inductance, $L_p$. Ohmic heating of the plasma is captured by the plasma resistance, $R_p$. It is often mathematically convenient to model the transformer action using a Thévenin-equivalent representation, as shown in Figure1.5(b), such that the mutual inductance, $M$, between the drive coil and plasma appears directly in the circuit model.

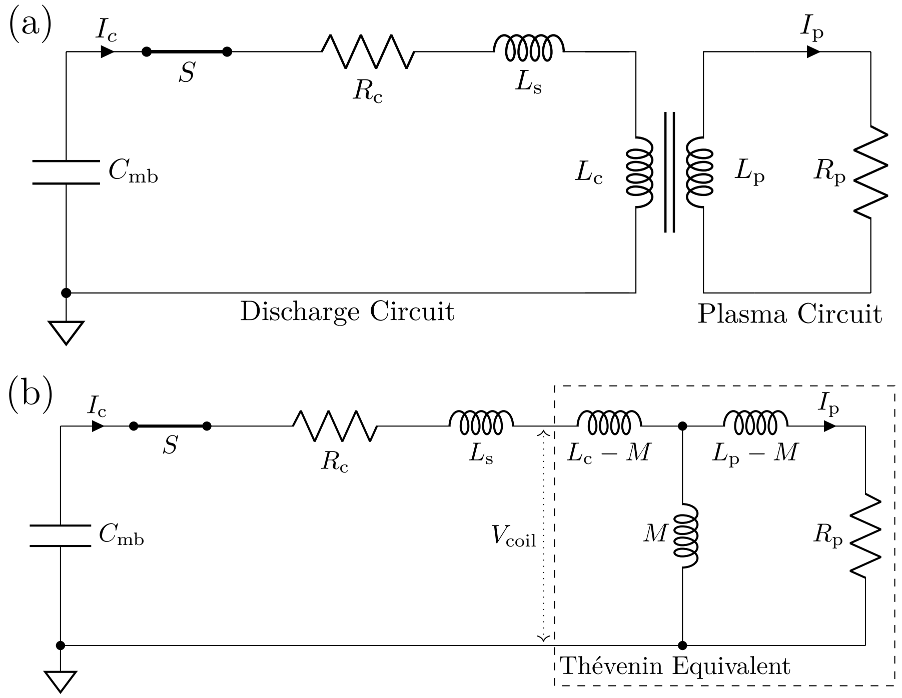

**Figure 1.5:** Basic circuit diagram of a series *RLC* IPPT discharge circuit. Shown are lumped element representations with (a) physically representative mutually coupled inductors (i.e. transformer) and (b) Thévenin-equivalent representation.

While the foundations of the model were originally developed to describe the operation of parallel-plate accelerators[1], the model was first applied to IPPTs by Lovberg and Dailey [18, 15]. Dailey and Lovberg adopted a "snowplow" model for the plasma dynamics, which assumed the current sheet was impermeable to all downstream plasma/propellant. The plasma resistance in this model was calculated by either assuming a fixed temperature or a temperature profile or by prescribing a plasma resistivity based on empirical data[27, 18]. Despite the relative simplicity of this model, its results for thruster performance were found to be in reasonable agreement with experimental measurements. Two important predictions were made by this model. First, it was indicated that thruster performance would remain relatively constant across a range of operational parameters. Second, performance was found to be optimized when the characteristic timescales for the electrical discharge and current sheet acceleration were similar. Both of these results were later supported by experimental data[8].

Non-dimensionalization of the model by Polzin and Choueiri[28, 16] revealed a set of scaling parameters for IPPT performance that were analogous to those found for parallel-plate accelerators[1]. These were the inductance ratio, $L_s/L_c$, the damping ratios of the discharge and plasma circuits, $\Phi_1$ and $\Phi_2$, respectively, and the dynamic impedance parameter, $\alpha$. Several useful design rules were found from these parameters. First, an inductance ratio much less than unity was found to be necessary for efficient device operation. Second, an underdamped circuit, i.e., one where the average of the damping ratios was less than one, was found to produce higher efficiency and exhaust velocities. Third, the value of the dynamic impedance that optimized device performance was found to be achieved when the electromagnetic and plasma acceleration timescales were roughly equal. This provided physical insight into the prior results of Lovberg and Dailey[21], which showed the same phenomena.

Various researchers have attempted to refine the model by increasing the fidelity of the plasma model or extending it to higher dimensions. Work by Polzin *et al*[29] used a 1D MHD plasma model that allowed the energy and state variables, e.g., temperature, inside the current sheet to evolve self-consistently in time. Simulations with this updated plasma model showed that the partitioning of energy between thermal/internal, magnetic, and kinetic modes varied with the dynamic impedance parameter, $\alpha$. While the primary conclusions drawn from the previous model using fixed plasma parameters were found to remain valid, differences in the predicted performance were observed. These differences were attributed primarily to heating of the plasma not being properly accounted for in versions of the model that assumed constant plasma properties. Differences in predicted performance were most apparent at lower values of $\alpha$, where a greater portion of the stored energy was driven into heating of the gas rather than accelerating it.

Martin investigated the effects of coil angle on thruster performance by extending the plasma model to 2D[30]. The plasma model used by Martin was also refined to account for non-equilibrium between the ions and electrons and allow for deformation of the plasma volume in both the radial and axial dimensions. While the electron temperature was assumed constant, the ions were treated as either isothermal, adiabatic, or shock-heated, depending on the computed radial velocity. Martin found that, although certain coil angles produced a local maximum, a planar design, i.e., a coil angle of 90° produced the highest overall performance.

Most recently, work by Little et al.[31] incorporated a more sophisticated plasma model to investigate gas ionization and current sheet formation in planar IPPTs. Their plasma model included the effects of gas ionization, non-equilibrium between the electron and ion species, charge exchange collisions, and finite permeability of the current sheet to both particles and the accelerating magnetic field. Using this model, Little et al. found that current sheets exhibiting the slug or snowplow-like dynamics assumed in previous versions of the model were only formed under certain conditions. They suggested that the central factor was the evolution of the electron temperature over time, positing that this was governed primarily by a competition between Ohmic heating and cooling due to inelastic collisions, i.e., ionization, early on in the discharge.

More complex 2D MHD IPPT models have also been developed by various authors. Mikellides et al. presented an axisymmetric 2D model using the multi-block arbitrary coordinate hydromagnetic (MACH) code. This model considered thermal non-equilibrium between the ions and electrons and included the effects of propellant ionization. Simulation results showed that the plasma remained fairly radially uniform as it evolved, suggesting that the assumption of radial uniformity made in the 1D model is largely justified. Initial modeling of the PIT MK V and MK Va showed good agreement with experimental data for helium and argon propellants[32]. Simulations of thruster operation on ammonia found that the predicted performance was comparable with experimental values at lower discharge energies but underestimated the experimental values for discharge energies beyond $E_0 \approx 2\,\mathrm{kJ}$[25].

Nonetheless, the simulated results for ammonia at lower energy levels suggested that its higher performance relative to argon and helium was due to a decrease in radiative losses compared to these propellants.

The results of Mikellides et al. also provided insight into the experimental observation that the thruster performance tended to decrease above a certain specific energy. By examining the energy partitioning in their model, Mikellides et al. found that deposition of energy into internal, e.g. ionization, modes increased substantially once a critical specific energy value had been exceeded[32]. This finding was also supported by a later iteration of the model that included plasma coupling effects and self-consistent evolution of the plasma resistance and inductance[33].

In addition to the PIT MK V and MK Va devices, Mikellides et al. also modeled operation of planar IPPTs at lower ($\sim 100\,\mathrm{J}$) discharge energies[26]. Thrust efficiencies over 50% were reported when the simulation was initialized with the gas radially constricted to a region near the mean radius of the annulus, suggesting that efficient device operation was possible even at lower discharge energies. Like the higher discharge energy cases previously investigated, a decrease in performance was observed when the energy density exceeded the critical value. This was again attributed to an increase in the fraction of the initial energy spent on ionization. While the simulations used an overdamped $RLC$ driving current waveform, use of an energy recapture scheme was noted to be expected to provide improved performance. Finally, it was found that PI was most effective when used to ionize an thin layer near the coil face rather than the entire injected propellant.

Che et al. also investigated IPPT operation using an axisymmetric 2D MHD model[34]. Notably, their model differed from that of Mikellides et al. in that the ions and electrons were assumed to be in thermal equilibrium, ionization was not considered, and the effects of radiation were not included. Their simulation results led to several primary findings. First, secondary current sheets were found to form during later half-cycles of the discharge and contributed significantly to the overall thrust of the device. Second, relatively constant thruster performance could be achieved across a range of mass bit and discharge energies by keeping the specific energy constant. Third, in agreement with previous experimental results (e.g. [12, 13]), compression of the initial plasma against the coil face and achieving high radial uniformity were found to improve thruster performance.

## *1.3 High Pulse Rate IPPTs*

In his discussion of pulsed accelerators, Jahn noted that there may be certain advantages to operating at "very high frequency pulse repetitions"[1]. Operation of IPPTs in this mode presents a number of compelling benefits:

1. **Steady propellant injection:** If the pulse rate is high enough that propellant injected into the device does not flow beyond the decoupling distance in the time between pulses, it is possible that propellant could be injected in steady or quasi-steady state while retaining high mass utilization and thruster efficiency. This would eliminate the need for complex, failure-prone mechanical pulse valves that are typically used in pulsed devices.
2. **Pulse interactions:** Beneficial interactions between pulses could arise if the time between them is short enough that a subsequent pulse interacts to some degree with the wake/remnants of the preceding pulse. For example, trace plasma left over from the preceding pulse could assist in the breakdown of gas during the subsequent pulse. This would alleviate to some degree the difficulties of achieving rapid gas breakdown during each pulse or, alternatively, preclude the need for a separate PI system. It may also be possible that propellant not fully accelerated during the preceding pulse may be entrained and accelerated during the subsequent pulse, boosting propellant utilization.
3. **Lower discharge energies:** For a given thruster input power, the per-pulse discharge energy will scale inversely with the pulse rate. Lower discharge energies tend to correlate with lower peak voltages and currents. Lower voltages could reduce the overall system mass by reducing electrical insulation requirements. Similarly, lowering the current during each pulse could reduce Ohmic losses. Lower voltages and currents may

also allow for the use of solid-state switches in the discharge circuit, enabling longer thruster lifetimes.

4. **Wider impulse range:** For a fixed target total impulse, the impulse bit also scales inversely with the pulse rate. This suggests that high pulse rate IPPTs could span a wide range of impulses, potentially enabling a single thruster to be responsible for both primary propulsion and precision spacecraft maneuvers.

The IPPTs discussed thus far were all designed either as research devices to be operated in a single-pulse mode or as low pulse rate devices with repetition rates $\lesssim 100\,\text{Hz}$. While no experimental results for a high pulse rate planar IPPT have been reported at the time of writing, a combination of theoretical work and experimental results from high pulse rate PPTs and field reverse configuration (FRC) thrusters suggests that such a device may not only be practical but also exhibit high performance.

Experimental work by Ziemer et al. characterized a gas-fed PPT operated at discharge repetition rates up to 5000 kHz for short bursts of pulses[35]. This high repetition rate was enabled by a solid-state modulator comprised of an insulated gate bipolar transistor (IGBT) commutator in conjunction with a magnetic switch. Per-pulse discharge energies for this device ranged from 2 J to 7 J. This thruster was operated in a “burst” mode wherein gas was injected in quasi-steady pulses that were long relative to the discharge repetition rate. Ziemer et al. measured thruster efficiency as high as 50% on argon and attributed this efficiency, at least in part, to a significant improvement in the mass utilization over previous designs that relied on pulsed gas injection.

Considerable work has also been invested in the development of high pulse rate FRC thrusters. Development of these devices has largely centered around the electromagnetic plasmoid thruster (EMPT)[36] and electrodeless Lorentz force (ELF) thruster[37, 38]. High pulse rates were achieved in both of these devices through the use of solid-state switching technology, namely IGBTs, in the discharge circuit. The EMPT was a 500 W to 5000 W device designed to operate continuously with steady gas injection. The nominal pulse rate was 2800 Hz with characteristic pulse energies of 2 J in single pulse mode and 12.7 J in multi-pulse operation. Impulse bits of 13 µN s were measured in multi-pulse mode. The ELF was a higher power (10 kW to 100 kW) RMF-FRC thruster that, similar to the EMPT, was designed to operate in a high pulse rate ($\geq$ 1 kHz) mode with steady gas injection. Due to PPU constraints, however, test data was only presented for single-shot operation. For these tests, the average discharge energy was 46 J. The impulse bit of this device was found to be about 400 µN s from momentum flux sensor data, while a separate calculation estimated the thrust efficiency to be $\approx$ 8%.

On the theoretical front, Martin[30] used a numerical model to explore the potential performance of a high pulse rate IPPT in greater detail. In this work, Martin considered a relatively compact thruster (18 cm outer drive coil diameter) that discharged a 10 µF capacitor bank at a rate of 1 kHz. The nominal energy stored in this bank ranged from 5 J to 20 J. In addition to the standard “full-ringdown” mode, wherein the discharge circuit is allowed to freely oscillate until the initial energy stored on the capacitor bank is completely dissipated, he also considered two “inductive recapture” modes of operation. In these modes, the discharge waveform is interrupted at either the first or second zero-crossing of the discharge current, respectively, e.g., by closing the discharge switch at the appropriate time. For $I_{sp}$ in the 3000 s to 5000 s range, he found that, while efficiencies as high as 42% could be achieved in the standard full-ringdown mode of operation, efficiencies in excess of 70% could be achieved in each of the recapture modes. Moreover, Martin’s results indicated that efficiencies above 60% could still be achieved even with charging voltages and current rise rates much lower than the optimal values.

As we have seen, there are promising signs that operating IPPTs at high pulse rates may provide advantages over previous low pulse rate designs. Given the lack of experimental data for these devices, however, there are a number of open questions that require investigation. Central to many of these questions is the tendency of higher pulse rate operation to result in lower discharge energies and, by extension, current rise rates. For a pulsed device operating at a fixed power, the per-pulse discharge energy scales inversely with the repetition rate. To estimate the expected pulse rates, we can use the requirement for high mass utilization that the injected propellant must not escape the decoupling distance between pulses. Assuming a noble gas propellant such as argon and noting that $z_{dc} \leq 10\,\text{cm}$ in previous planar IPPTs, we estimate required pulse rate to be in the kilohertz range. This value is in line with the pulse rates reported in previous high pulse rate PPT[35] and FRC[39] devices.

As an example, we consider the Nuclear-Electric Pulsed Inductive Thruster (NuPIT) mission, which investigated operating a version of the PIT operated from a 200 kW nuclear generator. At this power, a thruster operating at $\gtrsim 1\,\text{kHz}$ would have a per-pulse discharge energy $\leq 200\,\text{J}$, which is more than an order of magnitude below the nominal 4000 J discharge energy of the later PIT designs. For a high-pulse rate thruster to obtain comparable discharge energy, megawatts of power would be required. This would limit the use of high-pulse-rate IPPTs primarily to future interplanetary or deep space missions using advanced nuclear power systems. To be feasible in the near, or even medium, term, it is clear that high pulse rate IPPTs will need to operate with lower discharge energies than previous lower pulse rate designs.

For the 1 kW to 10 kW power systems commonly found on today's higher power spacecraft, the discharge energy may only be on the order of a few Joules. At these discharge energies, which would be significantly lower than any previously reported in the literature, questions about effective gas breakdown, ionization, current sheet formation, and acceleration become pertinent. While Polzin[16, 23] demonstrated that propellant pre-ionization (PI) can be used to reduce the current rise rates and, by extension, discharge energy required to form a current sheet, the sheets that were formed were observed to be at least partially permeable. Since no thruster performance measurements were reported for FARAD, this leaves open the possibility that only weak sheets that are unable to support efficient thruster operation were formed. Moreover, the mechanisms by which PI improves current sheet formation were not conclusively identified, and, as such, it is not known if there is a lower limit beyond which PI can no longer facilitate current sheet formation.

Although Martin's work suggests that it should be feasible to operate IPPTs efficiently in the 5 J to 20 J range of discharge energies, the plasma model he used contained several simplifications[30]. Most notably, the process of current sheet formation was neglected, and the sheet was simply assumed to exist at initiation of the discharge. While a comparison of the performance estimates from Martin's model with data from the PIT MK V [8] indicated that this assumption may be acceptable for such high discharge energy devices, it is possible that it is less applicable at lower discharge energies.

Indeed, the results of Little et al.[31] showed that the current sheet became more permeable once the discharge energy fell below a threshold value. This behavior was explained in terms of the dimensionless "formation parameter", which described the balance between ohmic heating of the electrons and cooling due to inelastic collisions early in the discharge. Lower discharge energies were found to reduce ohmic heating during this period, thereby resulting in smaller formation parameters. Nonetheless, Little et al. predicted that efficiencies in excess of 65% could be achieved for discharge energies as low as 25 J.

Although the models of Martin and Little et al. suggest that efficient high pulse rate IPPTs in the $\sim 10\,\mathrm{kW}$ range should be possible, neither has been validated against relevant experimental measurements due to lack of data. This highlights the need for experimental work to validate the models and advance the development of high-pulse rate IPPTs.

### *1.3.1 Power Processing Units*

Absent from the discussion thus far have been the systems required to operate IPPTs at high pulse rates. Central to this endeavor is the circuitry used to rapidly recharge the capacitor bank of the IPPT to its nominal discharge voltage. Fundamentally, this circuitry takes on the role of a capacitor charging power supply (CCPS). CCPSs that are compatible with common spacecraft bus voltage and power requirements are a key part of the power processing unit (PPU) for IPPTs. As shown in Figure 1.6, the primary function of an IPPT PPU is to serve as an electrical interface between the spacecraft bus and IPPT discharge circuit, performing, among others, the task of stepping up the relatively low voltage supplied by the spacecraft bus to the higher voltages typically required by IPPTs.

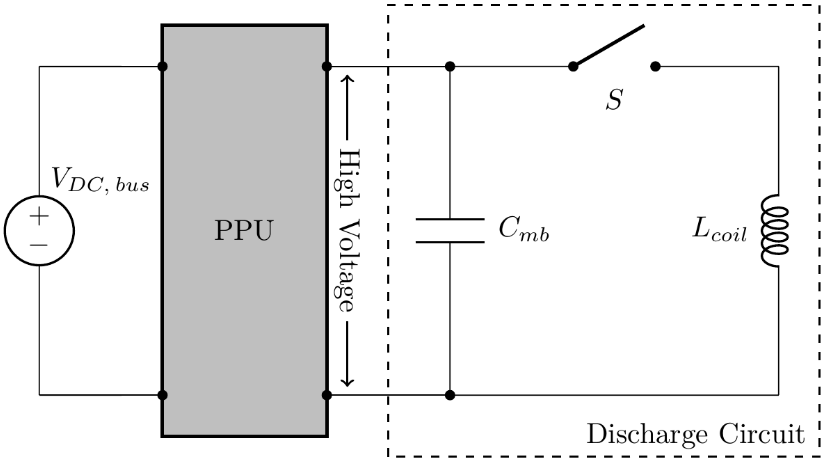

**Figure 1.6:** Diagram illustrating the location and role of the PPU in stepping-up the voltage for an IPPT capacitor bank.

PPUs with pulse charging capabilities have been developed and tested with the EMPT[36] and ELF thrusters [40, 41, 42] in continuous operation. The basic circuit topology of these PPUs, shown in Figure1.7, relies on the resonant charging of a capacitor via an inductor. The primary advantages of this method are its relative simplicity, low parts count, and use of passive, rather than active, components to perform the charging process.

Various versions of the EMPT and ELF PPU have been reported, with pulse rates as high as 2.8 kHz, average power up to 15 kW, and converter voltage gain greater than 10 reported[36, 40, 41]. Input voltages varied from 24 V to 300 V, which is generally within the range of common spacecraft bus voltages[43]. Successful operation for over $10^9$ discharges and 100 hrs was demonstrated, as was steady-state thermal operation in vacuum. High power operation was achieved by paralleling several lower power modules. Thermal testing of the PPU revealed that heat was mostly generated in the pulse charging/discharge switch, indicating that switching losses were the dominant energy loss mechanism and that a distributed switch array was highly beneficial for PPU thermal management.

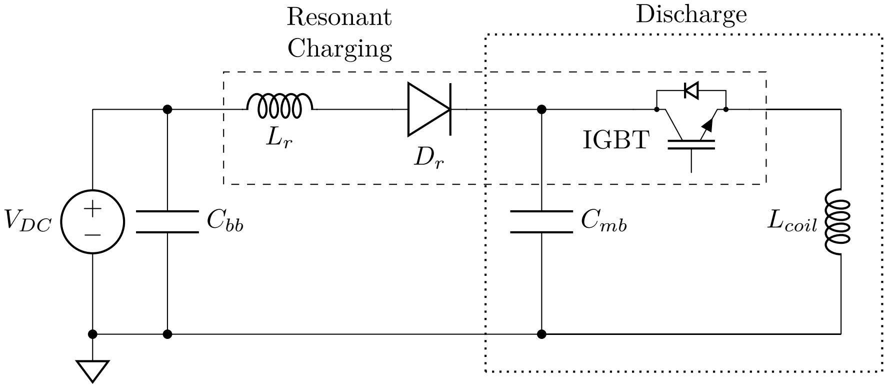

**Figure 1.7:** Discharge coupled resonant charging circuit diagram. Note that the IGBT responsible for discharging the main capacitor bank also controls the resonant charging time.

"Proto-flight" versions of the ELF PPU have been developed for power levels of 1 kW and 5 kW[42]. Circuit schematics and an assembled version of the 5 kW "J6" PPU are shown in Figure 1.8. Having been successfully operated for more than 1 billion discharges, the ELF PPUs are the most extensively tested IPPT PPUs. In addition to power throughput and longevity, the ELF PPUs demonstrated steady thermal operation in vacuum and were subjected to vibration, thermal, and radiated EMI testing as part of an effort to advance the readiness level of the ELF thruster system[42]. Both PPUs retained nominal functionality with no mechanical failures during three-axis vibration testing, indicating that the PPUs were capable of withstanding launch-like vibrational loads. Preliminary in-atmosphere thermal testing of the J6 PPU revealed that component temperatures remained well within the tolerable range after several minutes of continuous operation. Overall PPU efficiency was estimated at 88%[42], which is $\leq$ 10% below comparable PPUs designed for gridded ion and Hall thrusters[44].

The implementation of the resonant charging used in the PPU developed for the EMPT and ELF thrusters, however, limits their ability to power a wider range of high pulse rate IPPTs. Because the charging circuit shares a switch with the discharge circuit (see Fig-

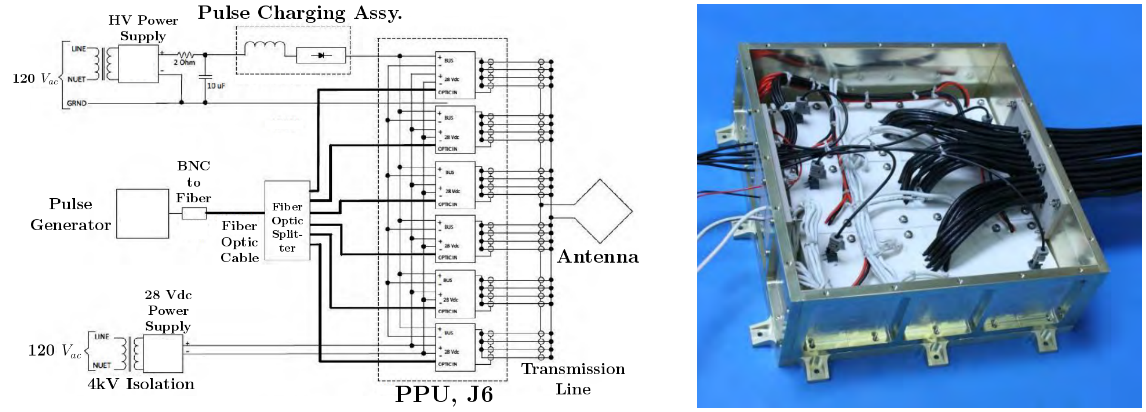

**(a)** J6 PPU configuration **(b)** Assembled J6 PPU

**Figure 1.8:** The ELF J6 PPU (from [42]).

ure 1.7), charging and discharging are coupled events. In other words, resonant charging only occurs while the discharge switch is closed. This largely prevents these PPUs from being used to power IPPTs implementing inductive recapture since the charging time would be prohibitively short. In addition, the concurrency of the charging and discharging presents a challenge for very high pulse rate operation ($\gtrsim 10\,\text{kHz}$). At these rates, the required charging current could become comparable to the discharge current and distort the discharge waveform. As such, the development of a PPU design that can support inductive energy recapture across a wide range of pulse rates is a key milestone for high pulse rate IPPTs.

## *1.4 Dissertation Outline*

Having discussed the motivations for developing high pulse rate IPPTs, we now turn to the objectives of the present work. The primary aim of this dissertation is to lay the groundwork for future development and testing of high pulse rate planar IPPTs by investigating several key questions that are fundamental to their operation:

1. What might a PPU capable of powering a wide range of high pulse rate IPPTs, in-

cluding those using inductive energy recapture, look like and how might it scale?

2. How does the current sheet evolve, particularly at lower discharge energies?
3. What are the primary factors influencing current sheet formation and how do these values scale with the thruster operational parameters?

To gain insight into these questions, a compact planar IPPT was developed to serve as a testbed. The experimental data collected from testing this device are intended to both shed light on the three primary questions posed above as well as serve as a test case for existing and future theoretical models.

With our introduction complete, the remaining chapters of this dissertation are as follows. In chapter 2, the operation and performance of a PPU for IPPTs operating at high pulse rates is presented. Chapter 3 explores the question of current sheet evolution in planar IPPTs using experimental measurements from the testbed IPPT. Chapter 4 uses the data presented in chapter 3 to investigate the fundamental physics governing current sheet formation in a planar IPPT and attempts to predict how these factors might scale with key IPPT operational parameters. Finally, chapter 5 summarizes the main conclusions of this work and briefly outlines several potential avenues for future development of high pulse rate planar IPPTs.

## Chapter 2

# A POWER PROCESSING UNIT FOR IPPTS OPERATING AT HIGH REPETITION RATES

In this chapter we present the design and testing of a prototype PPU intended to power a wide range of high pulse rate IPPTs, including those using inductive energy recapture, from a nominal spacecraft bus. This PPU is designed to support pulse rates up to 10 kHz and input power up to 10 kW. We discuss the criteria used to select the PPU circuit topology, and then present the basic theory of its operation. Through measurements of the device when operated in a burst mode, we are able to characterize the performance of the prototype PPU. Finally, we conduct an analysis of the measurements and use our results to investigate the scaling of the PPU as well as identify areas of improvement. [1]

### *2.1 Introduction*

Inductive pulsed plasma thrusters (IPPTs) are a type of electric propulsion (EP) device which generate thrust by ionizing a gaseous propellant and then inductively accelerating the resulting plasma to high velocities via the magnetic component of the Lorentz force [3]. IPPTs have two primary advantages over non-inductive EP devices, such as Hall or ion thrusters. First, inductive plasma acceleration eliminates the need for electrodes in direct contact with the plasma. This allows for fully electrode-less operation, which can significantly reduce contamination and thruster lifetime issues and affords greater flexibility in propellant selection [8]. Second, because the power of a pulsed device scales with the pulse rate, assuming the other operating parameters remain unchanged, constant specific impulse

---

[1] This chapter contains results from Curtis Promislow and Justin Little. Operation and performance of a power processing unit for inductive pulsed plasma thrusters operating at high repetition rates. IEEE Transactions on Plasma Science, 50(9):3065–3076, 2022.[45].

and thrust efficiency may be achieved over a wide range of input power levels [23].

IPPTs have traditionally been designed to operate at nominal pulse rates on the order of 1 Hz to 100 Hz [3]. At these rates, pulsed gas injection using high speed pulse valves becomes necessary to prevent propellant from escaping unaccelerated in the time between pulses and keep the mass utilization and overall thruster efficiency high. If the pulse rate is sufficiently high that injected propellant does not move beyond the coil coupling distance in between pulses, however, it has been hypothesized that high mass utilization could be achieved with steady propellant injection. This opens the possibility of eliminating the pulse valve from the gas injection system, which would reduce system complexity, enhance reliability, extend lifetime, and, in the event that mass utilization is improved, increase overall thruster performance. Based on coupling distances reported in literature [18, 46, 23], the required pulse rate is expected to be on the order of 1 kHz to 10 kHz for a planar IPPT operating on noble gases such as argon or xenon. Theoretical modeling and simulations have indicated that efficiencies in excess of 60% could be achieved when such high pulse rate IPPTs are operated in an inductive energy recapture mode [30]. For a given power, higher pulse rates also lead to lower per-pulse discharge energies. These lower energies can, in turn, lead to reduced voltage and current in the IPPT discharge circuitry and help ease the transition from previously used spark gap switches to modern solid-state switching technologies. Such a transition is expected to be necessary for increasing IPPT lifetimes [15, 47].

IPPTs require some form of power processing unit (PPU) to convert electrical power from the spacecraft power bus into a form usable by the propulsion system. The primary function of the PPU when powering an IPPT is to fully recharge the main capacitor banks, $C_{mb}$, of the thruster discharge circuit in the time between pulses (Figure 2.1). As such, the PPU essentially acts as a spacecraft bus-compatible capacitor charging power supply (CCPS). We note that while Figure 2.1 depicts a standard IPPT discharge circuit consisting of $C_{mb}$, switch, $S$, and drive coil, $L_{coil}$, alternative topologies have been proposed [48].

The PPU must also step up the voltage from the spacecraft bus voltage to the multiple kilovolts typically required for efficient IPPT operation. Since the bus voltage is usually no

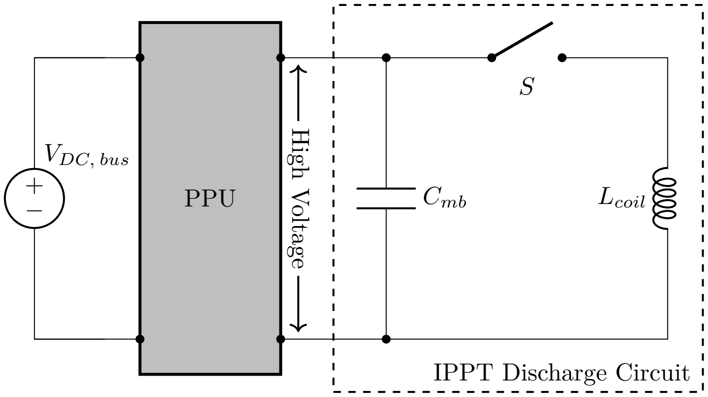

**Figure 2.1:** Block diagram of an IPPT with a PPU for supplying power from a spacecraft DC bus.

more than $\sim 100\,\mathrm{V}$ even for large spacecraft [43], voltage gain of $\gtrsim 10$ is required. With the energy for propulsion in an EP system coming from the spacecraft bus, the electrical efficiency of the power conversion process becomes an important component of the overall thruster efficiency. Electrical efficiency is thus a key metric for any EP system PPU. Operation on a spacecraft also imposes some unique constraints on PPU design. Mass and volume are usually very limited, making high energy density and efficient use of space essential. Moreover, repair of systems on-board the spacecraft is usually impractical, making redundancy and robustness to fault critical PPU attributes.

While PPUs designed to power a high pulse rate planar IPPT have not been reported in the literature, PPUs for high pulse rate field reversed configuration (FRC) IPPTs have been developed previously [41, 42] and represent the present state of the art[3]. In these PPUs, however, charging of $C_{mb}$ can only take place while the discharge switch, $S$, is closed. If $S$ is only closed for a short time, as is typical when operating in the inductive recapture mode, the available charging time is also short, making the required charging current impractically large. Consequently, these PPU are generally incompatible with IPPTs seeking to use inductive recapture.

Here, we present a PPU designed to support operation of 1 kW to 10 kW class IPPTs to pulse rates up to 10 kHz. Our PPU design is unique in that it is intended to function as an isolated, stand-alone CCPS, making it compatible with a wide range of IPPTs, including those using inductive energy recapture. In addition, the PPU circuit topology is highly modular, allowing for potential scaling of the design to higher power levels while also providing natural redundancy and fault tolerance.

## ***2.2 Circuit Topology, Theory, Modeling, and Operation***

### *2.2.1 Circuit Topology*

When powering an IPPT, the PPU is, in essence, a spacecraft bus compatible CCPS. A wide variety of CCPS designs may be found in the literature for terrestrial applications, including particle accelerators, pulsed lasers, and railguns [49, 50, 51, 52, 53]. A comparison of common CCPS topologies found in literature led to the selection of a boost converter based topology for the prototype PPU. A design using two paralleled boost cells was selected as a compromise between complexity, performance, scalability, and PPU volume and mass. While series resonant, parallel resonant, and series-parallel resonant (e.g. LLC, LCC) CCPS topologies were also considered, preliminary SPICE modeling suggested that the relatively low input voltage (120 V to 200 V) would result in large recirculating currents on the primary side when operating at high power, leading to significant conduction losses. We note, however, that only fixed duty cycle, fixed frequency switching was used in our models.

A high level circuit diagram of this paralleled boost converter circuit topology is shown in Figure 2.2. In this diagram, a DC power supply is used to represent the spacecraft bus. A large “backing” capacitor bank ($C_{bb}$) is charged by the spacecraft bus and is used to supply the large surge currents required by the circuit during operation. If the bus is capable of supplying the peak currents on its own, this capacitor is not needed. From here, two “boost cells” are connected in parallel. Each cell contains an insulated-gate bipolar transistor (IGBT) switch ($S_{sw}$), inductor ($L_b$), and diode ($D_b$). It should be noted the boost

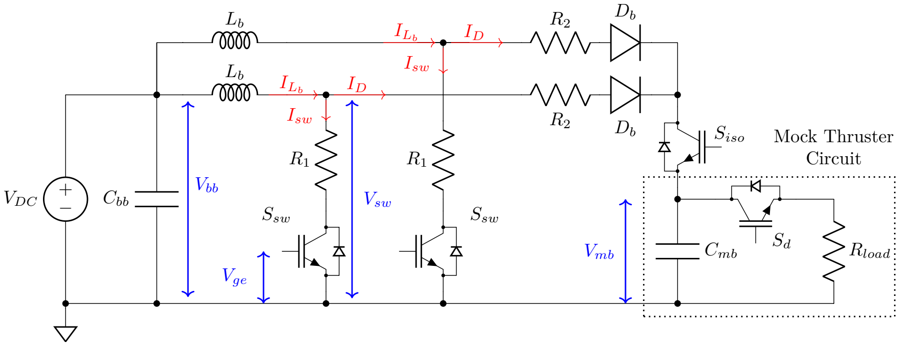

**Figure 2.2:** High level circuit diagram of paralleled boost converter design selected for the PPU circuit topology.

inductors and diodes in Figure 2.2 are representative lumped elements and may be comprised of multiple sub-elements in series or parallel.

The output of the boost cells is connected to the output or “main” capacitor bank, $C_{mb}$, via an isolation switch, $S_{iso}$. This switch isolates the PPU from the main bank when it is discharged and prevents the discharge circuit from interfering with the charging functionality of the PPU or vice versa. A mock thruster discharge circuit was used to simulate the energy taken from the main bank to form and accelerate the plasma propellant in an actual IPPT. This mock thruster circuit consisted of a high side IGBT, $S_d$, for discharging the main capacitor bank as well as a resistive load, $R_{load}$. Closing $S_d$ allowed energy stored on $C_{mb}$ to be dissipated in $R_{load}$. After a specified amount of energy was drained, $S_d$ could be opened to retain some fraction of the original stored energy on $C_{mb}$, mimicking energy recovery by inductive recapture. Since the PPU is agnostic to the method by which $C_{mb}$ is discharged due to $S_{iso}$, this method of partially discharging $C_{mb}$ was used to circumvent the complexities associated with implementing an inductive recapture system and simulated plasma load.

### *2.2.2 Theory of Operation*

On-off timings of the boost cell, isolation, and discharge switches are shown in Figure 2.3a, represented by their respective gate-emitter voltages. Note that $V_{ge,sw}$ indicates the gate-emitter voltage of both boost cell switches. In this idealized diagram, we have, for simplicity, ignored the finite switching times of the IGBTs and represent the transition between the on and off states as instantaneous. When the voltage is low, the associated switch may be assumed to be open, i.e., off. Upon transition to the upper-level voltage, the switch is considered closed, i.e., on. We define the start of the cycle as the moment that the boost cell switches are activated. The on-time of the switch, $\tau_{on}$, is defined as the product of the switch duty cycle, $D_{on}$, and the PPU period, $T$, where $T$ is simply the inverse of the recharging pulse rate, $f_p$.

Operation of the PPU may be broken down into three main phases. The first phase begins when the boost cell switches are activated. During this phase, current begins to flow from $C_{bb}$ through the boost cell inductors and switches, as shown in Figure 2.3b. These currents are labeled $I_L$ and $I_{sw}$, respectively, and are equivalent in this phase. Current continues to rise until the boost cell switches are turned off, which marks the end of phase 1 and the beginning of phase 2. At the moment of switch turn-off, both $I_{sw}$ and $I_L$ are at their maximum, denoted as $I_{peak}$.

During phase 2, highlighted by the blue region in Figure 2.3b, the induced voltage that forms across $L_b$ pushes current $I_D$ through $D_b$ onto $C_{mb}$. This results in the rapid increase in $V_{mb}$ observed in Figure 2.3c. Meanwhile, $I_{sw}$ decays rapidly at the start of phase 2 due to the turn-off of $S_{sw}$. In Figure 2.3 this decay is shown as instantaneous but in a real circuit $I_{sw}$ will fall over some finite period of time. Dissipation of $I_{sw}$ in $S_{sw}$ as the switch is turned off results in so-called switching losses. Switch $S_{iso}$ is closed just before the end of phase 1 to enable recharging of $C_{mb}$.

Once the flow of current onto $C_{mb}$ has ceased, $S_{iso}$ is opened and we move into the third, or discharge, phase of operation. The time elapsed between the closing and opening of $S_{iso}$ is

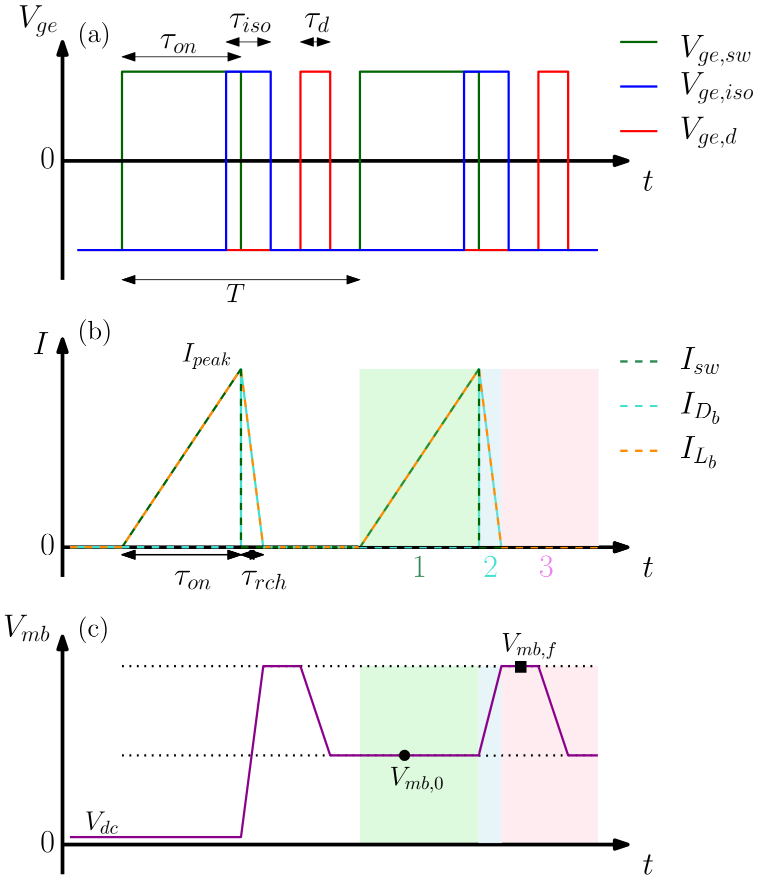

**Figure 2.3:** Idealized (a) gate voltages indicating switch timings, (b) boost inductor, switch, and diode currents, and (c) main capacitor bank voltage over two pulses.

referred to as $\tau_{iso}$. The main bank voltage remains constant until the closing of $S_d$ to initiate the mock discharge. This discharge may take place at any time between when $S_{iso}$ is opened and the start of the next cycle and has duration of $\tau_d$. While $S_d$ is on, $V_{mb}$ falls exponentially in an $RC$-type decay with resistance $R_{load}$ and capacitance $C_{mb}$. Once $S_d$ is opened, this decay stops and $V_{mb}$ is held constant. In cycles after the first, $C_{mb}$ will be recharged from this value, labeled in Figure 2.3c as $V_{mb,0}$, rather than $V_{dc}$.

### 2.2.3 Theoretical Model

A theoretical model of a simplified circuit was developed to gain insight into PPU operation. For deriving this model we first considered a single boost cell and ignored $C_{bb}$ and the mock thruster circuit. In the first phase, the circuit is modeled as a an $RL$ circuit connected to a constant voltage DC supply. Using this simple model, we find that the boost inductor current in phase 1 rises according to

$$I_{L_b,1} = \frac{V_{dc}}{R_1}\left(1 - e^{-2\alpha_1 t}\right) , \tag{2.1}$$

where $V_{dc}$ is the bus or backing bank voltage, $R_1$ is the lumped element circuit resistance in phase 1, $L_b$ is the effective boost inductance, and $t$ is the time elapsed since the boost cell switches reached the on state. Variable $\alpha_1$ is the damping coefficient of the phase 1 circuit given by $\alpha_1 = R_1/(2L_b)$. If the $L/R$ time is sufficiently large that the product $\alpha_1 t \ll 1$, we can use the power series approximation for the exponential function to argue that

$$I_{L_b,1} \approx \frac{V_{dc}}{L_b} t \, . \tag{2.2}$$

The current through the boost inductors during phase 1 is therefore expected to grow in a linear fashion with a slope of approximately $(V_{dc}/L_b)$.

Following a similar procedure to phase 1, we model the PPU in phase 2 as a series $RLC$ circuit with a diode. Under this simplified model, we find that the boost inductor current may be expressed as shown in equation (2.3).

$$\begin{split} I_{L_b,2} = I_0 e^{(-\alpha_2 (t-\tau_{on}))} \Bigg[ \frac{1}{\omega_d} \left( \alpha_2 + \frac{V_{dc} - V_{mb,0} - I_0 R_2 - V_{df}}{L_b I_0} \right) \sin\left(\omega_d \left(t - \tau_{on}\right)\right) \\ + \cos\left(\omega_d \left(t - \tau_{on}\right)\right) \Bigg] \end{split} \tag{2.3}$$

In equation (2.3), $\omega_d$ is the damped frequency and $\alpha_2$ is the damping coefficient of the $RLC$ circuit formed by $L_b$, $C_{mb}$, and the equivalent lumped element resistance in phase 2, $R_2$. $V_{df}$ is the forward voltage drop across the boost cell diodes. Note that there is a separate effective resistance for each phase since the current flows through different components. The initial conditions are $I_0$, which is $I_{L_b,peak}$ from phase 1, and $V_{mb,0}$, which is simply the voltage left on the main capacitor bank after the previous discharge. While the decay of $I_{L_b}$ and $I_D$ and the rise of $V_{mb}$ are shown as linear in Figure 2.3b for simplicity, equation (2.3) indicates that they are actually non-linear. If, however, $R_2$, $L_b$, and $C_{mb}$ are such that $\omega_d\left(t-\tau_{on}\right) \ll 1$ and $\alpha_2\left(t-\tau_{on}\right) \ll 1$, by making use of the small angle approximations for the sine and cosine terms we find that equation (2.3) reduces to the linear form

$$I_{L_b,2} \approx I_{L_b,peak} - \frac{V_{mb,0}-V_{dc}}{L_b}\left(t-\tau_{on}\right) \ . \tag{2.4}$$

Here, we have also assumed that resistive and diode forward voltage drops are small compared with $V_{mb,0}$ and $V_{dc}$. Note that while this model was derived for a single boost cell, it may be extended to multiple paralleled cells by appropriately scaling $I_{L_b,peak}$, $L_b$, and the two resistances by the number of boost cells, $N_b$.

### *2.2.4 SPICE Model*

The theoretical model presented in section 2.2.3 assumes the transition between phase 1 and 2 is near instantaneous and, by extension, that switching losses are negligible. Since the boost switches are hard switched at maximum current, this assumption requires further scrutiny. To gain an improved understanding of the energy losses in the system, the PPU circuit was simulated in SPICE. Rather than using a formal IGBT SPICE model, such as those reviewed in [54], the boost cell IGBTs were instead modeled as time varying resistors with resistance of the form

$$R_{sw} = R_{sw,0} + R_{fit}\, e^{\alpha_{sw}\left(t-\tau_{on}+\tau_{adj}\right)} \ , \tag{2.5}$$

where $R_{sw,0}$ is an effective saturation resistance (in Ohms) and $\tau_{adj}$ and $\alpha_{sw}$ are empirically determined parameters that control switch turn-off timing and the speed at which switching occurs, respectively. $R_{fit}$ is a fitting resistance which was used to scale the exponential term. For simplicity, we set $R_{fit} = 1\,\Omega$ in this work. Equation (2.5) is intended to capture the rapid rise in resistance that occurs when the IGBT is turned off during the transition between phases 1 and 2. We note that a diode was placed in anti-parallel with each $R_{sw}$ to model the effect of the freewheeling diode found in many IGBT modules.

Another limitation of the theoretical model is that it does not account for the role of parasitic elements in the circuit behavior. The SPICE model accounted for various stray capacitances, including the parasitic capacitances of the boost inductors, $C_L$, diodes, $C_d$, and switches, $C_{sw}$. $RCD$ snubbers placed in parallel with the boost cell switches to control turn-off switching transients were also modeled, with their capacitance denoted as $C_{snub}$. The output capacitance of both the isolation and discharge switches were also considered, with values estimated from their respective datasheets.

For comparison with the experimental results, measured values were used for $C_{bb}$, $C_{mb}$, $L_b$, $V_{bb,0}$, and $V_{mb,0}$. The values of the stray capacitances, effective resistances, and switching parameters, i.e., $t_{adj}$ and $\alpha_{sw}$, were left as free parameters which could be adjusted to match the model output to the experimental waveforms. Initial values for $C_d$ and $C_{sw}$ were obtained from the datasheets of the boost diodes and switch, respectively, while the measured value of 2.2 nF was used as a starting point for $C_{snub}$. For the modeling results presented here, $R_{sw,0}$ was set to zero, with the switch on-state effective resistance accounted for as part of $R_1$.

## *2.3 Experimental Setup*

A benchtop implementation of the circuit in Figure 2.2 was constructed to investigate the performance of the PPU. A DC power supply was used to slowly charge a large film capacitor ($C_{bb} = 1460\,\mu\text{F}$), which served as the backing bank, to a nominal voltage between 120 V to 200 V. This voltage range was selected to mimic the range of bus voltages that might be available on a large spacecraft [43].

Three different values were used for the boost inductance in the course of testing. The building block of the boost inductors were air-core Brooks' coil inductors wound from 150/33 Litz wire (equivalent to 12 AWG) with a nominal inductance of 108 µH. Effective boost inductor values of 54 µH and 216 µH were achieved by connecting two of these coils in parallel and series, respectively. Air cores were used to avoid core saturation at high peak currents. The Brooks' coil configuration was chosen so that the mass and resistivity of the inductors for a given inductance would be minimized[55].

The diodes used in each of the boost cells were 1700 V, 182 A silicon carbide (SiC) Schottky diodes (GeneSiC, GB2X50MPS17-227). Two of these diodes were connected in series to allow for blocking up to 3400 V. SiC Schottky diodes were used due to the absence of a reverse recovery current and the superior thermal characteristics of silicon carbide. Two 6500 V, 200 A (Infineon, FZ200R65KF2) NPT IGBTs were used for the boost cell switches and were controlled via custom gate driver boards. These driver boards were designed to have very low stray inductance and supply up to 30 A peak drive current for fast switching times and reduced switching losses. Low stray inductance in the driver board was found to be crucial for avoiding overvoltaging the switch during turn-off of the boost inductors. It should be noted that 6500 V switches were used in the boost cells instead of 3300 V switches due to their higher $dI/dt$ rating, which was found to be critical to avoiding failure of the switches at turn-off. The isolation switch was not turned off or on while current was running through it, and so a lower rated, single 3300 V, 800 A IGBT (ABB 5SNA 0800N330100) was used for this switch.

The main capacitor bank was a $C_{mb} = 0.328\,\mu\text{F}$ film snubber capacitor (WIMA, FKP1X023307G) optimized for high frequency, high pulse current applications. A second 3300 V, 800 A IGBT (ABB 5SNA 0800N330100) in a high side configuration was used as the discharge switch, $S_d$. Finally, non-inductive, high voltage rated 200 Ω ceramic resistors (Ohmite, 254AS201KDS) were used for the resistive load. For most tests, two of these resistors were paralleled to achieve an effective 100 Ω load. It should be noted that these resistance values are not meant to be analogous to the resistivity of the plasma in an IPPT. They were instead sized based on the $RC$ time constant needed to achieve energy losses similar to that experienced in an IPPT implementing inductive recapture over a similar discharge timescale [30].

Wherever possible, connections between circuit elements were made using wide, 0.035 inch thick copper busbar. The outgoing and return lines were stacked and were typically separated by no more than a few millimeters in order to reduce the stray inductance in the system.

On the measurement side, high voltage differential probes with a 100 MHz bandwidth (Micsig DP20003 and Pintek, PT-8020) were used to record the voltage on the backing bank, main bank, and the gate voltages on both of the boost switches as well as the isolation and discharge switches. The total current through the each of the boost inductors, $I_{L_b}$, was measured using calibrated shielded current monitors with a 0.1 V/A sensitivity.

## ***2.4 Results and Discussion***

### *2.4.1 High Pulse Rate Operation*

The benchtop PPU prototype was tested at pulse rates of 1 kHz, 2 kHz, 5 kHz, and 10 kHz to investigate its performance across the full range of nominal pulse rates. The main and backing bank voltages and the current in each of the boost cells at $f_p = 10\,\text{kHz}$ are shown in Figure 2.4. For these tests, the DC power supply was isolated from the PPU using large resistors (1 kΩ) and the PPU was operated using only the energy stored in the backing bank. While this was done primarily to protect both the power supply and PPU in the event of a component failure, this method of operation may also have practical applications, such as on a spacecraft where the bus power is below the nominal PPU output power. For the experimental conditions tested, at least five to ten pulses were usually achievable before $V_{mb}$ fell below the target output voltage range of 2 kV to 3 kV.

Figure 2.4a shows successful charging of $C_{mb}$ to 3 kV and at 10 kHz pulse rates. Figure 2.4b suggests the approximation of a linear $I_{L_b}$ is appropriate in phase 1 and at the end of phase 2. Signs of non-linearity in $I_{L_b}$ early in phase 2, however, point towards a finite switching time. A gradual decrease in the achieved $V_{mb,f}$ is observed after the second pulse in Figure 2.4a. This is a byproduct of the gradual draining of the backing bank energy, which results in a lower $V_{bb,0}$ for each subsequent pulse in the train.

The negative current spike that follows turn-off of the boost cell switches in Figure 2.4b was found to be due to the stray capacitance in the circuit, collectively labeled as $C_{stray}$.

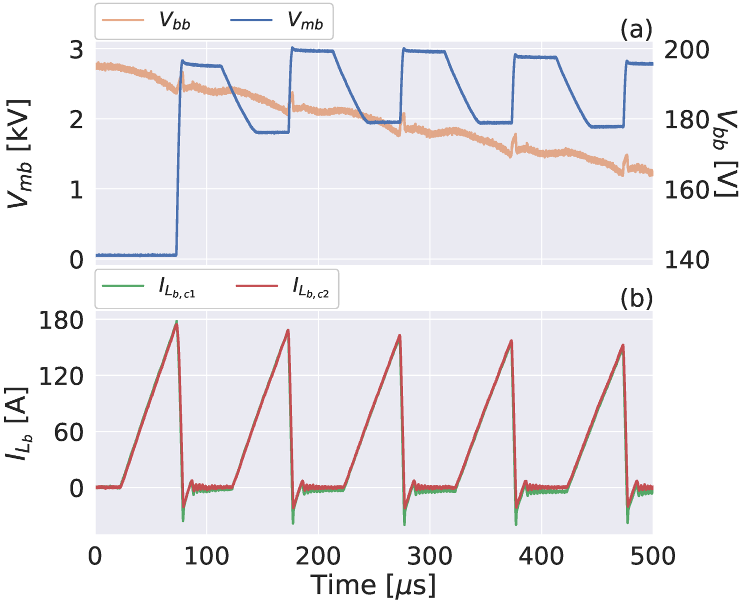

**Figure 2.4:** Demonstration of PPU operation at 10 kHz with 3 kV output. Shown are (a) $V_{bb}$ and $V_{mb}$ and (b) $I_{L_b}$ through each of the two boost cells during a 5 pulse train.

As a result, the amplitude and shape of the reverse current can be used to estimate $C_{stray}$ and characterize its effect on energy losses. Interestingly, the reverse current represents a recharging of $C_{bb}$ from energy stored in $C_{stray}$, indicating that not all energy stored in $C_{stray}$ is lost.

We also observe from Figure 2.4 that the currents in the two boost inductors, $I_{L_{b,c1}}$ and $I_{L_{b,c2}}$, are fairly well matched despite the lack of any active current balancing scheme. This indicates that the boost cells can be made to evenly share the charging current simply by matching the inductors and boost switch timings.

### *2.4.2 PPU Performance*

The PPU was tested under various conditions for each of the four pulse rates investigated. A summary of the tested conditions and the corresponding performance metrics is given in Table 2.1. Values with a "0" subscript represent initial values at the start of phase 1

**Table 2.1:** Brassboard PPU protoype performance measurements. The performance data shown was calculated for the second pulse in the pulse train.

| Case | $f_p$ | $D_{on}$ | $L_b$ | $V_{bb,0}$ | $V_{mb,0}$ | $V_{mb,f}$ | $\hat{E}_{rec}$ | $\hat{V}_{gain}$ | $I_{L_{b,peak}}$ | $P_{out}$ | $\eta_1$ | $\eta_2$ | $\eta$ |
|---|---|---|---|---|---|---|---|---|---|---|---|---|---|
| | [kHz] | | [μH] | [V] | [kV] | [kV] | | | [A] | [kW] | [%] | [%] | [%] |
| A | 1 | 0.052 | 54 | 193 | 1.27 | 2.93 | 0.19 | 15.2 | 179 | 1.1 | 99 | 57 | 59 |
| B | 1 | 0.070 | 108 | 194 | 1.26 | 2.94 | 0.18 | 15.2 | 122 | 1.2 | 98 | 62 | 64 |
| C | 2 | 0.200 | 216 | 174 | 1.57 | 2.85 | 0.30 | 16.4 | 79 | 1.9 | 98 | 62 | 66 |
| D | 2 | 0.280 | 216 | 141 | 1.30 | 2.98 | 0.19 | 21.1 | 87 | 2.4 | 96 | 67 | 69 |
| E | 2 | 0.351 | 216 | 109 | 1.25 | 2.77 | 0.20 | 25.5 | 82 | 2.0 | 94 | 66 | 67 |
| F | 5 | 0.251 | 54 | 145 | 0.89 | 2.10 | 0.18 | 14.4 | 128 | 3.0 | 96 | 60 | 60 |
| G | 5 | 0.261 | 54 | 193 | 1.27 | 2.95 | 0.19 | 15.3 | 180 | 5.8 | 98 | 60 | 59 |
| H | 5 | 0.352 | 108 | 145 | 0.90 | 2.14 | 0.18 | 14.7 | 92 | 3.1 | 98 | 61 | 63 |
| I | 5 | 0.350 | 108 | 194 | 1.26 | 2.96 | 0.18 | 15.3 | 121 | 5.9 | 97 | 66 | 65 |
| J | 5 | 0.476 | 216 | 194 | 1.24 | 2.92 | 0.18 | 15.0 | 84 | 5.7 | 100 | 69 | 70 |
| K | 10 | 0.503 | 54 | 146 | 1.36 | 2.25 | 0.36 | 15.5 | 128 | 5.3 | 96 | 55 | 54 |
| L | 10 | 0.503 | 54 | 174 | 1.65 | 2.71 | 0.37 | 15.6 | 156 | 7.6 | 98 | 54 | 56 |
| M | 10 | 0.503 | 54 | 188 | 1.81 | 2.97 | 0.37 | 15.8 | 168 | 9.1 | 98 | 55 | 58 |

while the “$f$” subscript indicates the final value achieved after charging. The “mb” and “bb” subscripts represent values belonging to the main and backing banks, respectively. Unless otherwise noted, subscripts “1” and “2” indicate association with the respective phase. In Table 2.1, columns $f_p$ through $V_{bb,0}$ are the primary design variables that were changed during the experiment, while columns $V_{mb,0}$ and onward are either measured or calculated values.

Variable $\hat{E}_{rec}$ is the inductive, or energy, recapture ratio and represents the fraction of the initial stored energy that is recovered onto the main bank ($C_{mb}$). It is given by

$$\hat{E}_{rec} = \frac{E_{mb,0}}{E_{mb,f}} = 1 - \hat{E}_{rch} \, , \tag{2.6}$$

where $E_{mb,0}$ and $E_{mb,f}$ are the initial and final energy stored in $C_{mb}$ and $\hat{E}_{rch} = E_{rch}/E_{mb,f}$ is the recharging ratio. $E_{rch}$ is the energy recharged by the PPU during a single charging cycle. The output power of the PPU is therefore $P_{out} = f_p E_{rch}$. The higher the recapture ratio, the larger the energy recovered by the main bank after a discharge. For a fixed output power, a larger $\hat{E}_{rec}$ allows for higher pulse rates to be achieved.

The voltage gain across the PPU is simply the ratio of the final output voltage to the initial input voltage, i.e.,

$$\hat{V}_{gain} = V_{mb,f}/V_{bb,0}\,. \tag{2.7}$$

Variables $\eta_1$ and $\eta_2$ are the effective efficiencies of phases 1 and 2, respectively, which we define as

$$\eta_1 = \frac{E_{L_b}}{E_{in,1}} \tag{2.8a}$$

$$\eta_2 = \frac{E_{rch}}{E_{L_b} + E_{in,2}}\,. \tag{2.8b}$$

Energies $E_{in,1}$ and $E_{in,2}$ are the energy transferred into the circuit from the backing bank during phases 1 and 2, respectively. $E_{L_b}$ is the peak energy stored in the boost inductors and is expressed as

$$E_{L_b} = N_b\left(\frac{1}{2}L_b I^2_{L_{b,peak}}\right)\,, \tag{2.9}$$

where $I_{L_{b,peak}}$ is the peak inductor current, which is achieved as the circuit transitions from phase 1 to phase 2. For the present prototype, the number of boost cells is $N_b = 2$. The denominator in Equation (2.8b) reflects that the energy for recharging the main bank comes from a combination of the energy stored in the boost inductors as well as a typically small amount of additional energy supplied by the backing bank during phase 2.

It should be noted that, as defined, the total efficiency, $\eta$, is not simply a product of $\eta_1$ and $\eta_2$ but is instead given by

$$\eta = \frac{E_{rch}}{E_{in,1} + E_{in,2}} = \frac{1 + E_{in,2}/E_{L_b}}{1 + E_{in,2}/E_{in,1}}\,\eta_1\eta_2\,. \tag{2.10}$$

In the limit $E_{L_b} \gg E_{in,2}$, however, equation (2.10) reduces to $\eta \approx \eta_1\eta_2$.

For the cases in Table 2.1, all of the energy used in the charging process can be assumed to come from $C_{bb}$, and we can calculate $\eta$ experimentally using the ratio of the change in main and backing bank energies

$$\eta = \frac{E_{rch}}{E_{in}} = \frac{C_{mb}}{C_{bb}} \frac{\left(V_{mb,f}^2 - V_{mb,0}^2\right)}{\left(V_{bb,0}^2 - V_{bb,f}^2\right)} \,. \tag{2.11}$$

With $C_{bb}$ and $C_{mb}$ known, $\eta$ can be conveniently determined from only measurements of the initial and final bank voltages.

The data in Table 2.1 show that the prototype PPU successfully demonstrated high pulse rate operation within the targeted 1 kW to 10 kW power range and with high voltage gain. Pulse rates from 1 kHz to 10 kHz were demonstrated while achieving the voltage gains required for stepping up spacecraft bus-level voltages to a level useful for IPPT operation. The minimum output voltage achieved was 2.10 kV in Case F while the maximum was 2.98 kV in Case D. The minimum voltage gain measured was 14.4 (Case F) while the highest was 25.5 (Case E). Although the output power generally increased with pulse rate, exceptions to this trend occurred due to variations in $\hat{V}_{gain}$ and $\hat{E}_{rec}$ between cases.

Figure 2.5 compares waveforms for $I_{L_b}$ and $V_{mb}$ generated by the SPICE model to the measured values as well as those predicted by the theoretical model comprised of equations (2.1) and (2.3) and the simplified linear model given by equations (2.2) and (2.4). Note that because resistive effects are absent from the linear model due to the stated assumptions, it is equivalent to the ideal case where all losses are negligible.

Figure 2.5a and 2.5b reveal excellent agreement between the SPICE model and the experimental waveforms for both $I_{L_b}$ and $V_{mb}$. Of particular note is the accuracy with which the exponential switch resistance model of equation (2.5) appears to be able to replicate the transient switching behavior of the IGBT. The SPICE model and experimental $I_{L_b}$ waveforms deviate only slightly during the transition between phase 1 and 2, with the SPICE model underpredicting $I_{L_b}$ by a few Amperes or less in most cases. The dashed vertical line in Figure 2.5c marks $t - \tau_{on} + \tau_{adj} = 0$ in equation (2.5), which we take as the start of switch turn-off in the SPICE model. This timing lines up well with the initiation of switch turn-off

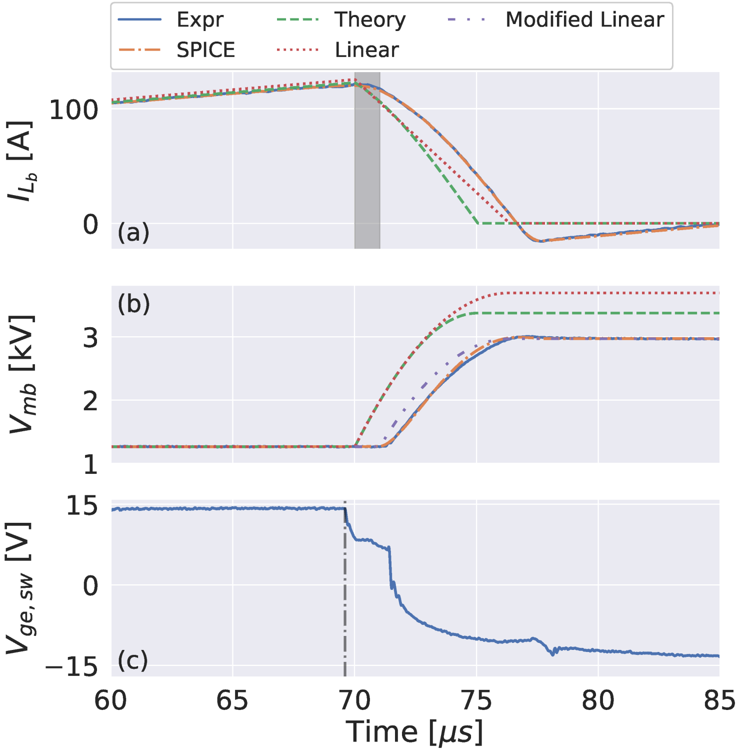

**Figure 2.5:** Comparison of experimentally measured waveforms for (a) $I_{L_b}$ and (b) $V_{mb}$ with those predicted by SPICE, simplified circuit theory, and the linear approximation to the circuit theory. Subplot (c) shows the measured gate voltage of the boost switch IGBTs and compares it to the fitted value of $t_{delay}$ for the SPICE model. The waveforms shown are for the second pulse in Case I.

in the experiment, indicated by the drop in the measured $V_{ge,sw}$.

Figure 2.5a also shows that the SPICE model is able to accurately predict the reverse current that occurs in the transition between phases 2 and 3. This is due to the inclusion and fitting of the stray capacitances in the SPICE model. The peak and shape of this reverse current were found to be impacted by the aggregate of $C_{sw}$, $C_{L_b}$, $C_d$, and $C_{snub}$. Of these, $C_{snub}$ was thought to have the largest contribution based on its measured value of 2.2 nF.

From Figure 2.5a we find that our simplified theory and the resulting linear approximation match the experimental $I_{L_b}$ well during phase 1. The linear model is found to slightly overpredict $I_{L_b}$ due to its inherent assumption of negligible resistance. The assumption in these models of instantaneous switching between phases 1 and 2, however, causes the predicted $I_{L_b}$ to fall and $V_{mb}$ to rise sooner than in the experimental data or SPICE results, as seen in Figures 2.5a and 2.5b, respectively. This assumption also neglects switching losses, which contributes to both theoretical models significantly overpredicting $V_{mb,f}$.

A modification to the theory can be made with the assistance of the SPICE model to add in the effects of turn-off switching losses. Instead of assuming $I_{L_b}$ immediately flows onto $C_{mb}$ in phase 2, we assume that $I_{L_b}$ continues to flow through the switch for a short period. This switching time, given by

$$\tau_{sw} = \frac{1.75}{\alpha_{sw}}\,, \tag{2.12}$$

is represented by the shaded region in Figure 2.5a, with the factor of 1.75 being determined empirically. After $\tau_{sw}$ has elapsed, $I_{L_b}$ is assumed to flow only into $C_{mb}$ as in the original theory. By treating the $I_{L_b}$ that flows during $\tau_{sw}$ as lost energy, we can include the effects of turn-off switching losses in the theoretical model without adjusting the model equations. Figure 2.5b shows that the inclusion of this modification greatly improves the $V_{mb,f}$ predicted by the linear model.

Given the close agreement of the SPICE and experimental waveforms in Figures 2.5a and 2.5b, we generally expect that the SPICE model should provide an accurate estimation of the energy losses in the PPU. The partitioning of energy predicted by the SPICE model is presented in Table 2.2 for the second pulse in cases G, I, and J. These three cases were selected for comparison since the initial and final conditions are similar in each.

In Table 2.2, $E_{R,1}$ and $E_{R,2}$ are the Ohmic losses due to the effective circuit resistance during phase 1 and phase 2, respectively. $E_{sw}$ is the turn-off switching loss and is defined as any losses due to energy dissipation in $R_{sw}$ (equation (2.5)). This differs slightly from the standard definition of switching losses as those occurring between certain percentages of $V_{ge,sw}$ and the collector current [56]. The "miscellaneous" energy losses tabulated under $E_{misc}$ account for losses in the $RCD$ turn-off snubbers and stray capacitance in the circuit.

**Table 2.2:** Partitioning of energies predicted by the SPICE model.

| Case | $E_{R,1}$ | $E_{R,2}$ | $E_{sw}$ | $E_{misc.}$ | $E_{loss}$ | $E_{rch}$ |
|---|---|---|---|---|---|---|
| | [mJ] | | | | | |
| G | 79 | 128 | 529 | 24 | 760 | 1184 |
| I | 49 | 92 | 442 | 26 | 609 | 1185 |
| J | 36 | 84 | 380 | 21 | 521 | 1148 |

The total energy loss for the pulse is given, for convenience, by $E_{loss}$. The total output, i.e., recharging, energy $E_{rch}$ is included so the losses may be put into perspective.

Table 2.2 shows that the SPICE model predicts switching losses are the dominant loss mechanism, accounting for 70% or more of $E_{loss}$ and between 33-45% of $E_{rch}$ for each of the three cases modeled. In contrast, total conduction losses were around 25% of total losses. Ohmic losses are calculated to be higher in phase 2 than phase 1 by roughly a factor of 2. Stray losses were estimated to be only a few percent, possibly as a result of the $C_{bb}$ recharging mechanism described in section 2.4.1, and remained relatively constant across all three cases.

Due to the prominence of the turn-off switching losses, adopting a quasi-resonant topology for the boost cells such that the switches achieve zero-current switching (ZCS) or zero-voltage switching (ZVS) at turn-off, may prove beneficial [57]. The implementation of these types of soft-switching techniques in boost converters and boost converter-based CCPS have been reported in the literature, for example in [58] and [59]. The efficiency of each of the phases as well as the overall efficiency predicted by the modified linear and SPICE models is compared to the experiment values in Table 2.3. Since the linear model neglects resistive losses by assumption, we estimated $E_{R,1}$ for the modified linear model by calculating Ohmic losses using $R_1$ from the full model with $I_{L_b}$ from the linear model. We justify this by noting that the full theoretical and linear models predict very similar $I_{L_b}$ in phase 1, as shown by

**Table 2.3:** Comparison of performance predicted by the modified linear (ML) and SPICE (SP) models to measured values (EX). Efficiencies are reported here in percent.

| Case | $\eta_1$ | | | $\eta_2$ | | | $\eta$ | | |
|---|---|---|---|---|---|---|---|---|---|
| | ML | SP | EX | ML | SP | EX | ML | SP | EX |
| G | 96 | 95 | 98 | 64 | 64 | 60 | 64 | 61 | 59 |
| I | 97 | 96 | 97 | 64 | 69 | 66 | 64 | 66 | 65 |
| J | 98 | 97 | 100 | 65 | 71 | 69 | 65 | 69 | 70 |

**Table 2.4:** Parameters used to generate the SPICE model predicted values in Tables 2.2 and 2.3.

| Case | $R_{C_{bb}}$ | $R_{C_{mb}}$ | $R_{b,1}$ | $R_{b,2}$ | $C_{L_b}$ | $C_{sw,b}$ | $C_d$ | $C_{snub}$ | $C_{sw,d}$ | $\alpha_{sw}$ | $\tau_{adj.}$ |
|---|---|---|---|---|---|---|---|---|---|---|---|
| | [mΩ] | | | | [nF] | | | | | [1/µs] | [µs] |
| G | 5 | 5 | 61 | 2500 | 0.10 | 0.10 | 1.30 | 2.00 | 6.00 | 2.20 | 0.28 |
| I | 5 | 5 | 61 | 2500 | 0.10 | 0.10 | 1.20 | 2.00 | 6.00 | 1.70 | 0.40 |
| J | 10 | 20 | 61 | 3250 | 0.10 | 0.10 | 1.20 | 1.80 | 6.00 | 1.30 | 1.10 |

Figure 2.5a.

Good agreement is observed in the case of $\eta_1$, where both models calculate high efficiencies comparable to the experimental value. In phase 2, the modification of the linear model using $\tau_{sw}$ from the SPICE model allows prediction of $\eta_2$ to within ±5%. The SPICE model is found to remain in good agreement with experiment for $\eta_2$, lending credence to the time varying switch resistance model. Both models and experiment agree that $\eta_2$ is noticeably lower than $\eta_1$, due to the impact of switching and higher conduction losses in phase 2. The modified linear model was found to predict the total efficiency to within ±5% while the SPICE model produced values within ±2%. Both models showed a tendency to underpredict efficiency for the lowest inductance case (Case G) and overpredict for the highest inductance case (Case J).

The parameters used in the SPICE model for generating the data in Table 2.2 are given in Table 2.4. Resistances $R_{C_{bb}}$ and $R_{C_{mb}}$ are the effective series resistances for the backing and main capacitor banks, respectively, while $R_{b,1}$ and $R_{b,2}$ are the effective resistances of each of the boost cells during phase 1 and phase 2, respectively. To find the values of $R_1$ and $R_2$ as defined in section 2.2.3, we use $R_1 = R_{C_{bb}} + R_{b,1}/N_b$ and $R_2 = R_{C_{mb}} + R_{b,2}/N_b$. We immediately notice that $R_{b,2}$ is over an order of magnitude higher than $R_{b,1}$, which explains the larger phase 2 Ohmic losses in Table 2.2. Comparing the effective frequencies of the current waveforms in each of the two phases, we find that the frequency is usually $\lesssim 1\,\mathrm{kHz}$ in phase 1 and then increases to $\gtrsim 10\,\mathrm{kHz}$ in phase 2. As such, it is hypothesized that AC resistivity effects, namely the skin and proximity effects, may be at least partially behind the increase in resistivity.

The higher $R_{C_{bb}}$ and $R_{C_{mb}}$ in case J compared to cases G and I is thought to be the result of higher ESR of the capacitors at low frequencies. The increase in $R_2$ is expected to be partially due to stacking multiple inductors in series to increase $L_b$. The stray capacitances were largely constant across all three cases apart from a few minor adjustments. This agrees with the results in Table 2.2, which showed that the parasitic losses remained similar. Finally, $\alpha_{sw}$ is found to decrease as $L_b$ increases and $I_{L_{b,peak}}$ decreases. $\tau_{adj}$ is observed to follow the opposite trend, indicating later initiation of switch turn-off as $I_{L_b}$ decreases. The datasheet for the FZ200R65KF2 IGBTs indicate that switching turn-off and delay times should scale inversely with collector current at turn-off, which agrees with the observed trends in $\alpha_{sw}$ and $\tau_{adj}$.

### *2.4.3 Performance Scaling*

Scaling of the PPU efficiency in each phase was investigated through the modified linear model. We find it useful to recast equations (2.8a) and (2.8b) in terms of the energy lost in each phase, $E_{loss,1}$ and $E_{loss,2}$, respectively. Note that we have defined these losses such that $E_{loss,1} = E_{in,1} - E_{L_b}$ and $E_{loss,2} = (E_{L_b} + E_{in,2}) - E_{rch}$, consistent with our definitions of $\eta_1$ and $\eta_2$ in section 2.4.2. To find simple equations guiding the scaling of $\eta_1$ and $\eta_2$, we make two additional simplifying assumptions. First, based on data in Table 2.1, we assume that the voltage gain (equation (2.7)) is large and the energy recovery (equation (2.6)) is non-negligible such that $\hat{V}_{gain}\sqrt{\hat{E}_{rec}} \gg 1$. Second, based on Table 2.2 we assume that the conduction losses in phase 2 ($E_{R,2}$) are small relative to the switching losses ($E_{sw}$) so that we may approximate $E_{loss,2} \approx E_{sw}$ and $E_{rch} \approx E_{L_b} - E_{sw}$. Under these assumptions, equations (2.2) and (2.4) were used to derive the following scaling laws:

$$\eta_1 \approx \frac{1}{1 + \frac{2}{3}\hat{V}_{gain}\left(\frac{\tau_{LC}}{\tau_{L/R_1}}\right)} \tag{2.13a}$$

$$\eta_2 \approx \frac{1}{\left(1 + N_b\sqrt{\frac{\hat{E}_{rec}}{1-\hat{E}_{rec}}\frac{\tau_{sw}}{\tau_{LC}}}\right)^2} \,. \tag{2.13b}$$

In addition to the previously defined $\tau_{sw}$, which represents the characteristic switching timescale, two key timescales appear in equations (2.13a) and (2.13b)

$$\tau_{L/R,1} = L_b/R_1 \tag{2.14a}$$

$$\tau_{LC} = \sqrt{(L_b/N_b)\, C_{mb}}\,. \tag{2.14b}$$

Timescale $\tau_{L/R,1}$ is the effective $L/R$ timescale for phase 1 and represents the characteristic timescale for resistive energy decay in phase 1. Timescale $\tau_{LC}$ is the effective $LC$ timescale and is related to the rates at which energy can be stored in and transferred from the boost inductors. It may be shown that the product $\hat{V}_{gain}\tau_{LC}$ is proportional to $\tau_{on}$, which, as shown graphically in Figure 2.3a, is the time it takes for boost inductors to reach their maximum stored energy, i.e., $E_{L_b}$. The $\eta_1$ scaling factor in equation (2.13a) may thus be interpreted as the ratio of the energy storage and energy dissipation timescales in phase 1. This ratio informs us that Ohmic losses can be minimized if energy can be stored in $L_b$ over a time period that is short relative to $\tau_{L/R,1}$, resulting in a high $\eta_1$. While $N_b$ does not show up

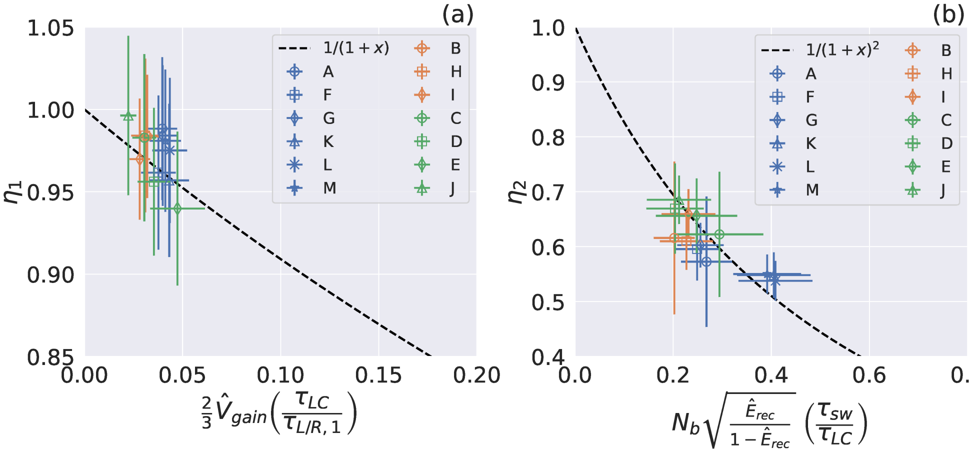

**Figure 2.6:** Scaling of (a) $\eta_1$ and (b) $\eta_2$ with their respective scaling parameters.

explicitly in equation (2.13a), a factor of $1/\sqrt{N_b}$ appears in $\tau_{LC}$, indicating that increasing the number of boost cells will decrease phase 1 Ohmic losses.

The timescale ratio $\tau_{sw}/\tau_{LC}$ in equation (2.13b) represents the impact of turn-off switching losses. A larger ratio indicates that, during phase 2, $I_{L_b}$ is slow to change from flowing through the boost cell switches to flowing onto $C_{mb}$, resulting in larger switching losses. The square root term in equation (2.13b) suggests that the relative importance of switching losses will increase with $\hat{E}_{rec}$. The energy recapture ratio is related to both the current at switch turn-off ($I_{L_b,peak}$) and the voltage across the switch immediately following turn-off ($V_{mb,0}$) and describes the intensity of the switching losses relative to the energy recharged onto the main bank. The increase of the switching losses with $N_b$ is simply a statement that, assuming no change in the other parameters, switching losses will scale linearly with the number of switches being used. The appearance of this $N_b$ dependency is notable, since it may render the strategy of increasing the number of boost cells to decrease the Ohmic losses untenable.

The inverse scaling of $\eta_2$ with $\hat{E}_{rec}$ is somewhat concerning. It has been shown that the discharge circuit of an IPPT should be strongly underdamped to achieve high efficiency [28]. Due to low damping, an efficient IPPT utilizing inductive recapture is likely to have a relatively high energy recapture ratio. This suggests the possibility of a compromise between thruster and PPU efficiency.

The presence of $\tau_{LC}$ in the numerator of equation (2.13a) and denominator of equation (2.13b) suggests that there will be some degree of trade-off between $\eta_1$ and $\eta_2$. While we aim to have the capacitor charging timescale be short relative to the resistive dissipation timescale in phase 1, we also require that this timescale be long relative to $\tau_{sw}$ to minimize switching losses. Within the parameter space of interest, however, it is likely that $\tau_{LC}$ will be closer to $\tau_{sw}$ than to $\tau_{L/R_1}$. Moreover, $\eta_2$ scales as $1/(1+x)^2$ while $\eta_1$ only scales as $1/(1+x)$. This suggests that minimizing the ratio $\tau_{sw}/\tau_{LC}$ should be prioritized to maximize overall efficiency in most cases.

Figure 2.6 shows the scaling of $\eta_1$ and $\eta_2$ with their respective scaling parameters. The points are grouped by nominal boost inductor value, with blue, orange, and green corresponding to $L_b$ of 54 µH, 108 µH, and 216 µH, respectively. The points are observed to generally follow the expected scaling trends, marked by the dashed black lines, in both figures 2.6a and 2.6b. Figure 2.6a shows the data is concentrated at low $x$-values where $\eta_1$ is high. This is due to relatively large $L_b$, low $R_1$, and modest output energies ($E_{rch}$), which resulted in an energy dissipation timescale that was long relative to the energy storage timescale. With $\hat{V}_{gain}$ typically on the order of $\sim 10$, the phase 1 timescale ratio was of order $10^{-3}$.

Figure 2.6b shows $\eta_2$ varies strongly with the scaling parameter, particularly at low $x$-values. With $N_b = 2$, minimizing $\tau_{sw}/\tau_{LC}$ and $\hat{E}_{rec}$ becomes important for achieving high $\eta_2$. Based on the values of $\hat{E}_{rec}$ in Table 2.1, we find the square root term in equation (2.13b) ranges from about 0.45 to 0.75. SPICE model results show $\tau_{sw}/\tau_{LC}$ varies relatively little for the cases in Table 2.1, with all calculated values falling within 0.21 to 0.28. This narrow range is likely due in part to the conjectured scaling of $\tau_{sw}$ with $L_b$ discussed in section 2.4.2, which seems to result in $\tau_{sw}$ trending with $\tau_{LC}$.

The general grouping of points with the same nominal boost inductance seen in Figure 2.6 is thought to be the result of the $1/\sqrt{L_b}$ factor that appears in the scaling parameters for both $\eta_1$ and $\eta_2$. This inverse relationship is due to a larger $L_b$ decreasing the $I_{L_{b,peak}}$ needed to store a certain $E_{L_b}$ and, by extension, output a certain $E_{rch}$. A lower $I_{L_{b,peak}}$ leads to lower Ohmic losses in phase 1, assuming $R_1$ remains unchanged, and lower switching losses in phase 2. This suggests that the efficiency in both phases should tend to increase as $L_b$ grows.

The data in Figures 2.6a and 2.6b generally support this hypothesis, with exceptions being attributed to variations in other parameters in the scaling laws. In Figure 2.6a, relatively large $\hat{V}_{gain}$ result in lower $\eta_1$ for cases D and E, even though $L_b = 216\,\mu\mathrm{H}$, which was the largest tested. In Figure 2.6b, cases K, L, and M have noticeably higher scaling parameter values than cases A, F, and G, despite sharing the same $L_b = 54\,\mathrm{nH}$. This is attributed to the high $\hat{E}_{rec}$ in these cases, which highlights the challenge of achieving low switching losses while keeping the inductive recapture ratio high.

Equations (2.13a) and (2.13b) hint that the design of the PPU and thruster are interconnected. Using the modified linear theory, we show that $\tau_{LC}$ has a lower limit dictated by the minimum allowable PPU efficiency and an upper limit set by the pulse rate of the thruster, $f_p$,

$$\frac{N_b}{\gamma}\sqrt{\frac{\hat{E}_{rec}}{1-\hat{E}_{rec}}}\tau_{sw} \lesssim \tau_{LC} \lesssim \frac{1}{f_p\hat{V}_{gain}\sqrt{1-\hat{E}_{rec}}}\,. \tag{2.15}$$

The lower limit in equation (2.15) was derived from equation (2.13b) by setting a minimum allowable phase 2 efficiency, $\eta_{2,min}$, with $\gamma = \sqrt{1/\eta_{2,min}} - 1$. The upper limit was produced by finding that the on-time scales as

$$\tau_{on} = \frac{D_{on}}{f_p} \sim \hat{V}_{gain}\sqrt{1-\hat{E}_{rec}}\,\tau_{LC}\,, \tag{2.16}$$

where $D_{on} = \tau_{on}/T$ is the on-time, and also the phase 1, duty cycle. Equation (2.16) shows that maximizing $D_{on}$ leads to the highest possible $\tau_{LC}$ for a given $f_p$, $\hat{V}_{gain}$, and $\hat{E}_{rec}$. Accordingly, this suggests that the PPU should seek to operate at the maximum allowable duty cycle to achieve the best efficiency. While for the purposes of equation (2.15) we have assumed the maximum duty cycle to be $D_{on} \approx 1$, in practice $D_{on} < 1$ since finite switching times and the existence of phase 2 require $\tau_{on} < T$.

If $\hat{V}_{gain}$ and $\hat{E}_{rec}$ are fixed by the thruster and satellite bus design and $D_{on}$ is at its maximum, equation (2.16) shows that increasing $f_p$ requires a decrease in $\tau_{LC}$. This indicates that, for a given $\hat{E}_{rec}$ and $\hat{V}_{gain}$, the maximum achievable PPU efficiency will tend to scale inversely with thruster pulse rate. We note that this trend is not observed in Table 2.1 because our choice of operating parameters led to a non-maximized $D_{on}$ in most cases.

The upper and lower limits in equation (2.15) may be combined to produce the constraint

$$f_p \lesssim \frac{\gamma}{N_b \sqrt{\hat{E}_{rec}} \hat{V}_{gain} \tau_{sw}} \, . \tag{2.17}$$

Equation (2.17) effectively states that $f_p$ must be sufficiently slow to allow $\tau_{on}$, and thereby $\tau_{LC}$, to be long enough that high $\eta_2$ can be achieved. We observe that, from a thruster design standpoint, large $\hat{E}_{rec}$ and $\hat{V}_{gain}$ tend to reduce the maximum attainable $f_p$. In terms of PPU design, it is found that $N_b$ and $\tau_{sw}$ can be reduced to achieve higher pulse rates. We also note that a lower $\eta_{2,min}$ can be traded off for higher $f_p$ via an increase in $\gamma$.

Timescale $\tau_{LC}$ is a combination of PPU design parameters $L_b$ and $N_b$, and thruster design parameter $C_{mb}$. In many cases, however, the choice of $C_{mb}$ will be constrained by the thruster design requirements. Decreasing $N_b$ is equivalent to increasing the effective boost inductance, i.e., $L_b/N_b$, with $\tau_{LC}$ being maximized for the minimum $N_b = 1$. The factor of $1/\sqrt{L_b}$ in the scaling parameters for $\eta_1$ and $\eta_2$ suggest that, ignoring mass and volume limitations, $L_b$ should be increased until $\tau_{LC}$ reaches its upper limit to maximize PPU efficiency.

Reducing $\tau_{sw}$ is an obvious target for improving PPU efficiency. Switching times could potentially be improved, for example, by using later generation IGBTs with improved turn-off characteristics or perhaps even series-stacked SiC MOSFET modules. While we have treated $\tau_{sw}$ as an independent variable in equation (2.13b) for simplicity, it often has a complex dependency on several factors, such as the collector current and collector-emitter voltage at turn-off, which may produce dependencies on variables such as $L_b$, $\hat{V}_{gain}$, $\hat{E}_{rec}$, or $N_b$. The apparent inverse scaling of $\tau_{sw}$ with $L_b$ found in Table 2.4, for example, may change how $\eta_2$ scales with $L_b$. Future work may seek to express $\tau_{sw}$ in terms of the PPU and thruster design variables.

### *2.4.4 Quasi-Steady Operation*

Quasi-steady state testing of the PPU prototype was performed by removing the 1 kΩ resistors between the DC supply and $C_{bb}$ and using a 15 kW Lambda ESS DC power supply with variable output up to 200 V and 75 A as the input power source. This supply was intended to mimic the power output of an appropriately sized spacecraft bus and had sufficient power to fully replenish the charge on $C_{bb}$ between pulses. For these tests, the PPU was operated for up to 20 pulses at a time while $V_{bb}$, $V_{mb}$, and $I_{L_b}$ were measured. The resulting waveforms for PPU operation at 2 kHz are shown in Figure 2.7. Unlike in Figure 2.4a, we observe that $V_{mb,0}$ and $V_{mb,f}$ become quite consistent for pulse two and onward. Examining all pulses after the first, we find pulse-to-pulse deviation in $V_{mb,0}$ and $V_{mb,f}$ to be less than 2% of the average value, providing strong evidence of quasi-steady state operation. While $V_{bb}$ fluctuates at first, possibly due to the DC power supply being unable to perfectly regulate its power output over such short timescales, it too appears to level out to the target value of $\approx 120$ V by the end of the pulse train.

While thermal imaging showed no signs of significant component heating in any of the tests performed, attempts to operate beyond about 20 pulses were halted due to concern over growing negative overshoot in $I_{L_b}$ following shut-off of the boost cell switches and an associated negative drift in the quiescent $I_{L_b}$, as seen in Figure 2.7b. The exact cause of this negative drift is unknown at present, but its stronger presence in boost cell one may indicate an imbalance between the cells.

### *2.4.5 Simulated Component Failure*

The robustness of the PPU was investigated by simulating a component failure in one of the boost cells. Rather than simulate the component failure itself, we instead simulated the expected fail-safe response, i.e., the isolation of the cell with the failed component, by opening the corresponding boost cell IGBT. The main and backing bank voltages and boost cell inductor currents over several cycles before and after deactivating one of the boost cell

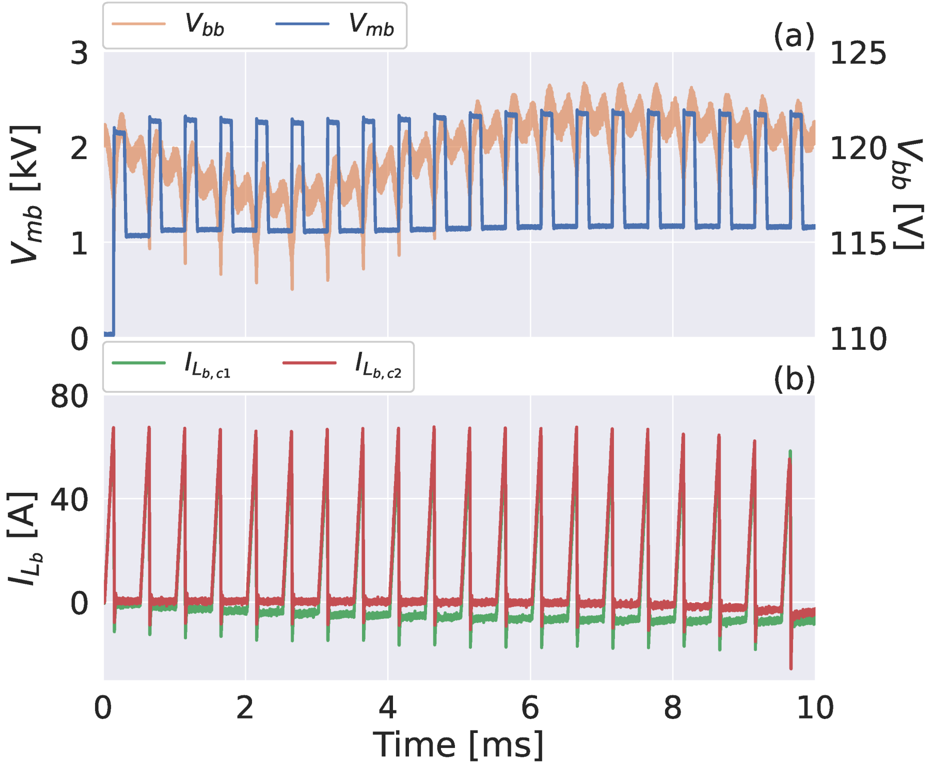

**Figure 2.7:** Demonstration of quasi-steady operation over 20 pulses at a pulse rate of 2 kHz. Shown are (a) Backing and main bank voltages and (b) current through each of the boost cell inductors.

switches are shown in Figure 2.8. The timing of the simulated component failure and switch deactivation is demarcated in Figure 2.8a by the red line just before 2 ms.

Prior to the simulated component failure, the waveforms indicate that the PPU is operating nominally. After the fourth pulse, the simulated component failure occurs and the switch in the first boost cell is disabled, as might occur with a failure detection circuit in place. Figure 2.8b shows $I_{L_{b,c2}}$ to be unaffected by the disabling of the first boost cell, highlighting the ability of each boost cell to operate independently in this PPU topology.

The loss of $I_{L_{b,c1}}$, however, predictably results in a decrease in the output power of the PPU. For Figure 2.8, the loss of cell one lead to a roughly 43% reduction in $P_{out}$. While

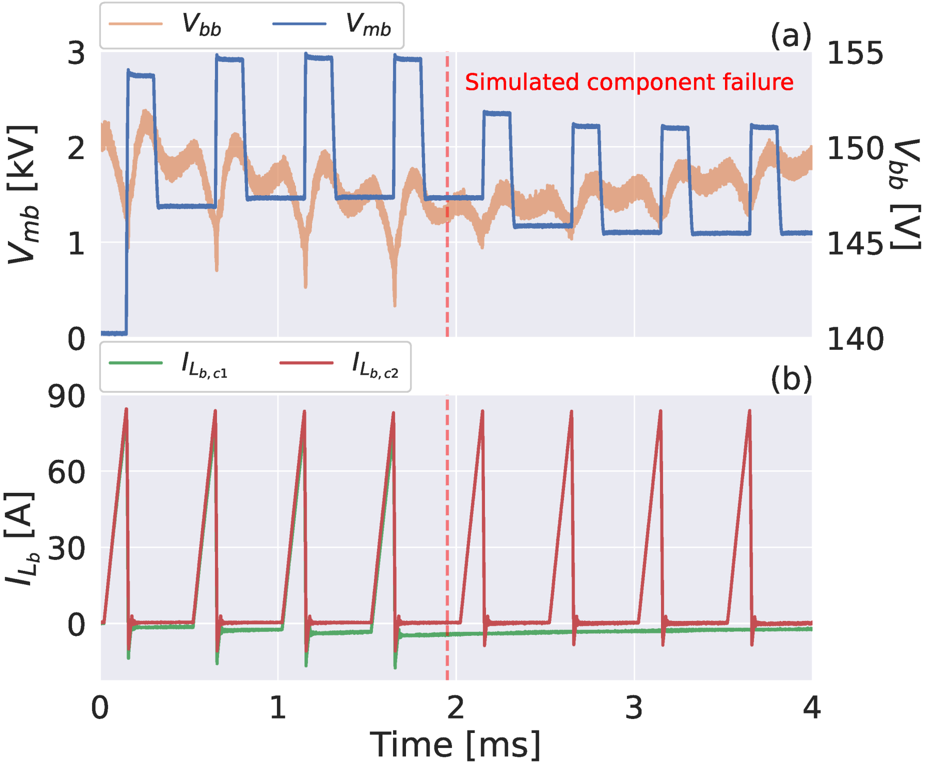

**Figure 2.8:** Demonstration of continued PPU operation after simulated component failure. Shown are (a) Backing and main bank voltages and (b) current through each of the boost cell inductors.

$D_{sw}$ was fixed at 0.25 for the waveforms shown in Figure 2.8, active control of the duty cycle could be used to increase $I_{L_{b,c2}}$ to compensate for the loss of $I_{L_{b,c1}}$. This would come at the cost of increased stresses in the remaining operational cell, however, as well as a lower efficiency due the increase in losses that accompanies an increase in the boost cell current.

## *2.5 Conclusion*

In this paper we have presented a prototype PPU for powering IPPTs operating at high repetition rates. A benchtop PPU was constructed and testing of this prototype at various pulse rates and in quasi-steady operation was presented. The PPU also demonstrated continued operation in the event of a loss of one of the boost cells, evidencing the robust and redundant nature of the proposed topology. Measurements indicated that the PPU was capable of supporting IPPT operation at pulse rates from 1 kHz to 10 kHz and power of 1 kW to 10 kW. Voltage gains between 14.4 and 25.5 were recorded for spacecraft bus level input voltages between 109 V to 194 V, yielding IPPT relevant output voltages between 2 kV and 3 kV. Total electrical efficiency varied from a low of 54% to a high of 70%.

A SPICE model of the PPU circuit topology revealed the efficiency of the second phase of operation, wherein energy is transferred from the boost inductors to the main capacitor bank, limits the overall PPU efficiency. SPICE modeling indicated that low phase 2 efficiency was primarily the result of switching losses in the boost cell IGBTs, which accounted for more than 70% of the total losses in some cases. Higher conduction losses also contributed to the lower efficiency in phase 2, and were hypothesized to be the result of AC resistivity effects.

Simple scaling laws for the phase 1 and phase 2 efficiencies were derived using the modified linear model. The former was found to scale with voltage gain and the ratio of the $LC$ and $L/R$ timescales while the latter scaled with the ratio of the switching and $LC$ timescales and inversely with the inductive recapture ratio. The modified linear theory was also used to show that the maximum thruster pulse rate the PPU can support is constrained by the number of boost cells, inductive recapture ratio, voltage gain, switching timescale, and minimum allowable phase 2 efficiency. Given that the efficiency of the present PPU appears switching loss dominated and that switching losses may become large at high recapture ratios, implementation of soft switching techniques, such as the use of quasi-resonant switch configurations to achieve ZCS or ZVS at turn-off, may be of interest for future prototypes.

# Chapter 3

# CURRENT SHEET EVOLUTION IN A PLANAR IPPT

In this chapter we investigate the formation of the current sheet in planar IPPTs. The formation of this current sheet is essential to the operation of a planar IPPT and, as such, understanding its formation is paramount to their development. We present a compact planar IPPT prototype intended to be used as a testbed for the development of high pulse rate IPPTs. By using several diagnostics to collect measurements of this device while operating in a single-shot mode in a constant pressure gas backfill, we are able to gain new insight into the evolution of the current sheet over time.[2]

## *3.1 Introduction*

Inductive pulsed plasma thrusters (IPPTs) are a type of electric propulsion (EP) device that produces thrust by inductively accelerating a plasma generated from a gaseous propellant [3, 8]. In an IPPT, a discharge circuit produces a time-varying current, which in turn gives rise to time-varying electric and magnetic fields. When a sufficiently conductive plasma is present close to the drive coil, image currents will form to oppose the change in magnetic flux through the plasma. The interaction between the drive coil and induced plasma currents then accelerates the plasma, producing thrust.

IPPTs are unique compared to other EP concepts in that both plasma generation and acceleration are accomplished inductively. This has the advantage of eliminating electrodes in contact with the plasma, which avoids lifetime limitations associated with electrode erosion and allows for a wider range of propellants to be used [8]. This property makes

---

[2] This chapter contains results from Curtis L Promislow and Justin M Little. Current sheet evolution in a planar inductive pulsed plasma thruster. Journal of Physics D: Applied Physics, 57(20):205205, 2024.[60]

IPPTs of interest for missions involving in-situ resource utilization[5], multi-mode propulsion concepts[61, 4], and atmosphere-breathing EP[6, 7].

The inductive nature of IPPTs means that the discharge circuit in these devices is complete and current can flow even in the absence of a plasma. This necessitates the rapid breakdown of the gaseous propellant into a highly conductive plasma which is impermeable to the magnetic field produced by the thruster; otherwise, energy is lost to resistance in the thruster circuitry without producing meaningful thrust. Due to the skin effect, this highly conductive plasma is expected to contain a thin region, known as the "current sheet"[11], where most of the current is concentrated. Similar structures are also observed and investigated in other types of plasma accelerators, namely pulsed plasma thrusters[62] and theta-pinch devices[63].

A lumped-element circuit model has been extensively used to model the coupling between the IPPT discharge circuit and the translating current sheet [64, 3]. A circuit diagram of the equivalent lumped-element circuit used in the model is shown in Figure 3.1. First developed by Daily and Lovberg [27, 15], the model couples the discharge circuit to a plasma circuit via a transformer model. The mutual inductance, $M$, which describes the inductive coupling between the discharge circuit and current sheet is usually found via an empirical equation that casts it as a function of the distance of the sheet from the drive coil [18, 46]. The bulk effective plasma resistance, $R_p$, is typically calculated from the plasma resistivity, which is often obtained from estimates of the relevant collision frequencies[64].

Dailey and Lovberg found the circuit model predicted IPPT performance in good agreement with thrust stand measurements [15]. Dailey and Lovberg also used the model to predict relatively constant thrust efficiency over the range of design parameters where the electrical and acceleration timescales were similar [21]. Polzin non-dimensionalized the circuit model and discovered several key scaling parameters, namely the inductance and critical resistance ratios and the dynamic impedance [16]. Polzin found that thrust efficiency was maximized at values of dynamic impedance where the electrical and acceleration timescales were matched. He also observed that efficiency increased as the inductance ratio decreased

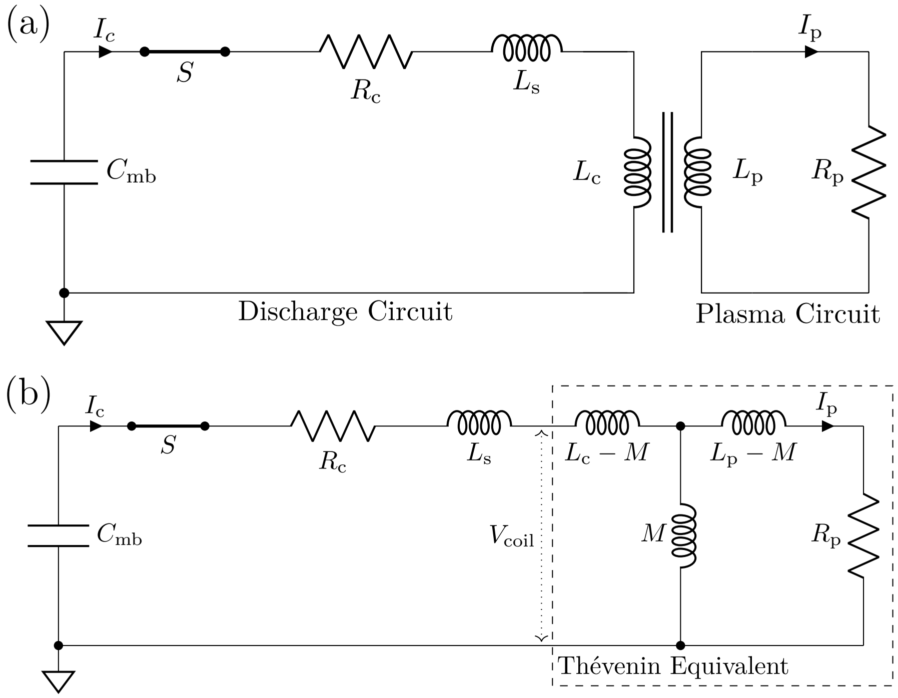

**Figure 3.1:** Lumped element circuit diagram of the IPPT discharge circuit transformer coupled to the plasma. The coupling can be modeled as a (a) transformer or its (b) Thévenin-equivalent circuit.

and that both efficiency and exhaust velocity increased as the critical resistance ratios decreased.

A recent 1D model by Little et. al. [31] used the circuit model in conjunction with a non-equilibrium plasma model to investigate current sheet formation. Their results indicated that current sheet formation was a balance between Ohmic heating of the electron population and cooling of said population through collisional interactions with the neutral particles. Little et. al. also proposed a dimensionless “formation parameter” for describing current sheet formation and discovered a critical value of this parameter above which a current sheet would form[31].

Knowledge of $M$, or equivalently the coupling coefficient, $k$, provides a measure of how well the discharge circuit is coupled to the translating current sheet and is closely related to the properties and motion of the sheet. Meanwhile, $R_p$ allows for calculation of the plasma heating, which has been identified as critical to current sheet formation[31]. Together, $M$ and $R_p$ provide powerful insight into the evolution of the current sheet.

We present here methods for calculating $M$ and the effective skin depth resistance within the current sheet, $R_{sd}$, (a more relevant analogue to $R_p$) as functions of time from experimental measurements. We then apply the presented methods to data obtained from a compact, low per-pulse discharge energy IPPT operating in static background fill conditions. Details of the thruster and diagnostics used to collect the measurements are supplied in section 3.2. The methods used to parse the data are detailed in section 3.3. General application of the methods is covered in section 3.4. Finally, the methods are applied to understand the evolution of the current sheet in section 3.5 and the effects of the initial neutral gas density and pre-ionization (PI) on the evolution in section 3.6.

## 3.2 Experimental Setup and Data Collection

### 3.2.1 Experiment Setup and Operation

Data was collected from a research prototype IPPT, shown in Figure 3.3(a). The prototype IPPT had an inner and outer drive coil radius of $r_a = 1.9\,\text{cm}$ and $r_b = 7.2\,\text{cm}$, respectively. The drive coil itself was formed from eight 1.5 turn Archimedes spiral inductors connected in parallel and wound in a two-layer fashion to reduce stray inductance[3]. We measured this arrangement to have an inductance of 375 nH at 300 kHz using an $LCR$ meter. The stray inductance and decoupling distance of the drive coil were found to be 40 nH and 3.13 cm, respectively, by using the “dummy” load method described in the literature [46, 64].

The vacuum chamber was a glass tube (25.4 cm inner diameter, 60.96 cm long) with L-gaskets at both ends to form a vacuum seal between the chamber body and two endplates.

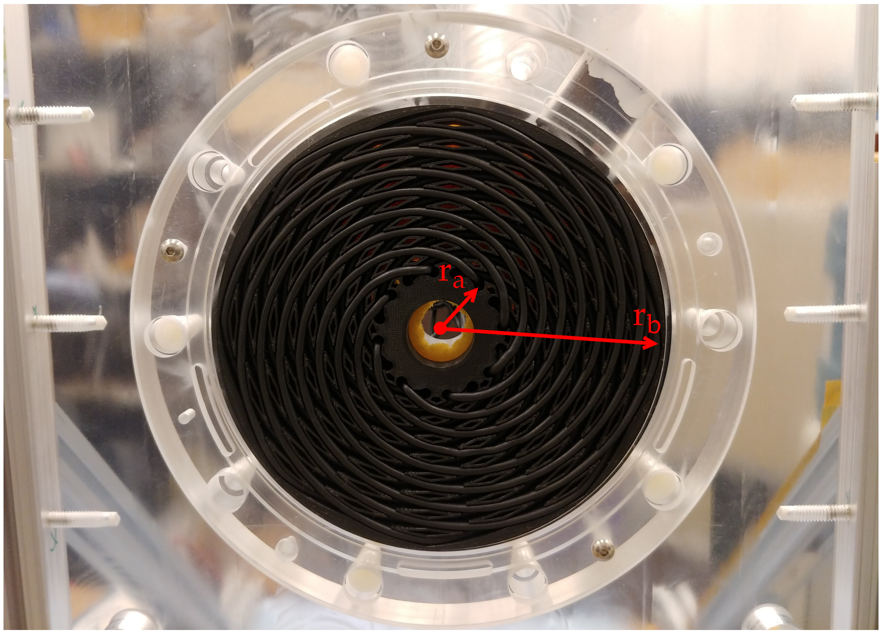

**Figure 3.2:** Image showing the multi-layer inductive drive coil of the prototype IPPT. Note that the metal bolts shown in this image were replaced with plastic ones prior to testing of the device.

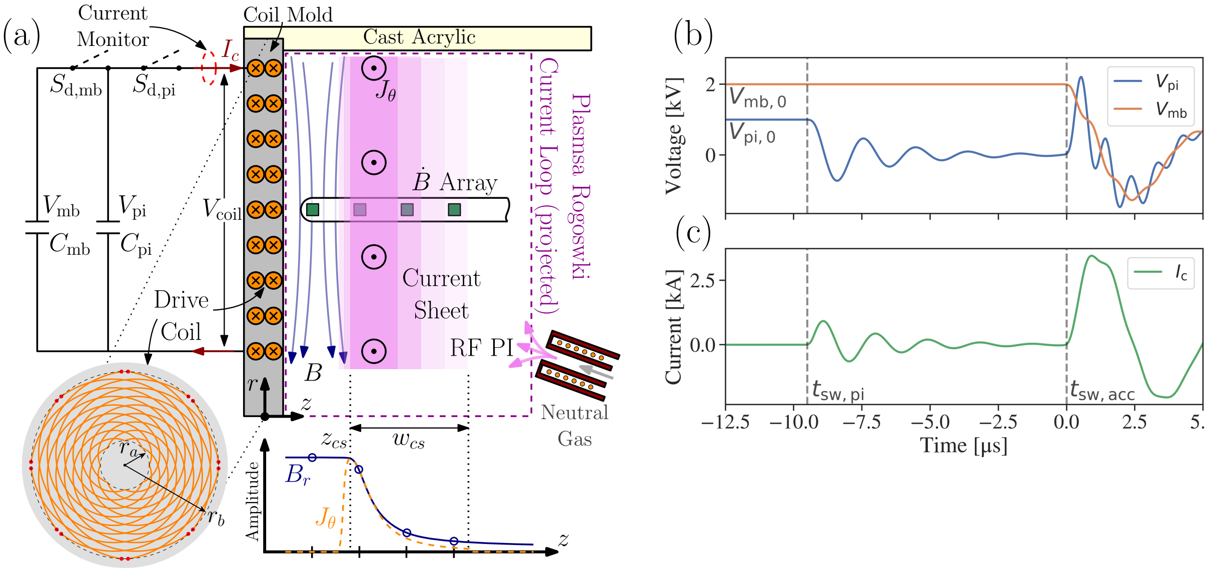

**Figure 3.3:** Diagram of compact, low discharge energy IPPT used for data collection from (a) side and front-on views and idealized (b) capacitor voltages and (c) discharge circuit current when a plasma is present in front of the drive coil.

The IPPT drive coil was mounted to a 30.48 cm × 30.48 cm × 2.54 cm cast acrylic endplate. The opposite endplate was stainless steel and contained electrical feedthroughs for the in-chamber diagnostics. An ISO 100 flange in this endplate led to the pumping system. The pumping system consisted of an Edwards 510 L/s turbomolecular pump backed by a 12 L/s rotary vane roughing pump and produced chamber base pressures as low as $1 \times 10^{-5}$ Torr ($1.33 \times 10^{-3}$ Pa). During experiments, pressure in the chamber was measured with a capacitive manometer (MKS 626D). This gauge provided a direct, gas composition independent reading of the total chamber pressure in the $1 \times 10^{-4}$ Torr to 0.1 Torr (0.013 Pa to 13.3 Pa) range with an accuracy of ±0.5 % of the reading. For the results presented here, gas was delivered through the RF PI, with the flow of gas controlled via a needle valve.

The discharge circuit of the IPPT consisted of two capacitor banks, two switches, and the drive coil, as shown in Figure 3.3(a). A "main" capacitor bank, $C_{mb}$, stores the energy

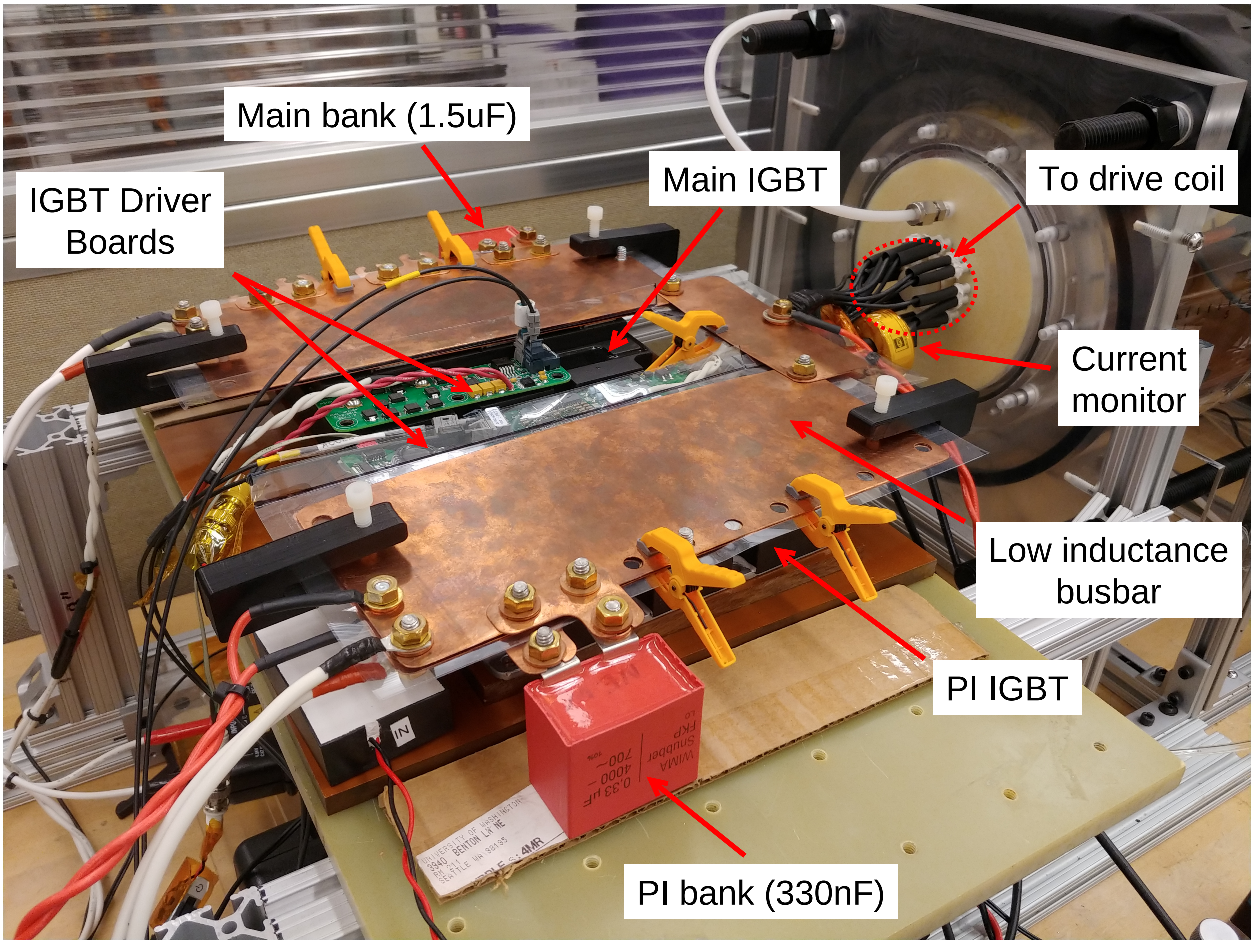

**Figure 3.4:** Image of the IPPT discharge circuit, with second stage PI and main capacitor banks shown.

for driving the time varying current that, ideally, forms and accelerates the current sheet. $C_{mb}$ was connected to the drive coil by an insulated gate bipolar transistor (IGBT) switch $S_{mb}$ (ABB 5SNA0750G650300). A second, smaller capacitance bank, $C_{pi}$, was discharged via IGBT switch $S_{pi}$ (ABB 5SNA1200E330100) and was part of the PI system. In this paper, $C_{mb} = 1.5\,\mu\text{F}$ and $C_{pi} = 330\,\text{nF}$. Nominal charging voltages for the capacitor banks were no more than $2\,\text{kV}$, giving a maximum total per-pulse discharge energy of $< 4\,\text{J}$.

At these low per-pulse discharge energies, the electric field induced by the current rise rate in our IPPT was found to be insufficient to break down the neutral gas unassisted. As such, a two-stage PI system was used to initiate gas breakdown and supply an initial plasma for the main discharge to couple energy into. The first stage was an RF PI, which consists of a 1.27 cm diameter solenoidal coil driven by a 13.56 MHz RF generator at 100 W. Gas injected through this coil was broken down by the high frequency fields and flowed into the chamber as a weakly ionized plasma. In the second stage, $C_{pi}$ was discharged through the drive coil, ionizing more of the neutral gas and distributing it more evenly over the coil face than using the RF PI alone. We note that PI can be accomplished through less complex means, such as Paschen breakdown between electrodes[17], and that the use of a PI system is unnecessary in IPPTs where the induced electric field is sufficiently large[23].

Typical operation of the IPPT discharge circuit is shown in Figure 3.3(b,c). Prior to operation, the static fill pressure in the chamber, $p_0$, is set and allowed to reach a steady value. Fill pressures were selected such that the thruster discharge energy was typically larger or comparable to the total energy required to ionize all propellant within the decoupling distance of the drive coil. Next, $C_{mb}$ and $C_{pi}$ are charged to their target voltages, $V_{mb,0}$ and $V_{pi,0}$, respectively. Once charged, the RF PI is turned on, initiating breakdown of the neutral gas. At time $t_{sw,pi}$, switch $S_{pi}$ is activated, marking the start of the second-stage PI. The RF PI is also deactivated at this time. After five cycles of the second-stage PI discharge, typically $\sim 10\,\mu\text{s}$, switch $S_{mb}$ is closed, connecting $C_{mb}$ to the drive coil and initiating the main discharge. We take the time of $S_{mb}$ closing ($t_{sw,acc}$ in Figure 3.3(c)) as $t = 0$ for plotting purposes.

### *3.2.2 Diagnostics*

Figure 3.3(a) depicts the current sheet formed by operation of the IPPT in an idealized case. Here, current flowing through the drive coil, $I_c$, generates a plasma and induces an azimuthal current density, $J_\theta$, to form a current sheet. The location of the leading edge of the current sheet relative to the coil mid-plane is given by $z_{cs}$, and the width by $w_{cs}$. Integration of $J_\theta$ over the current sheet volume yields the total plasma current, $I_p$. The total magnetic field,

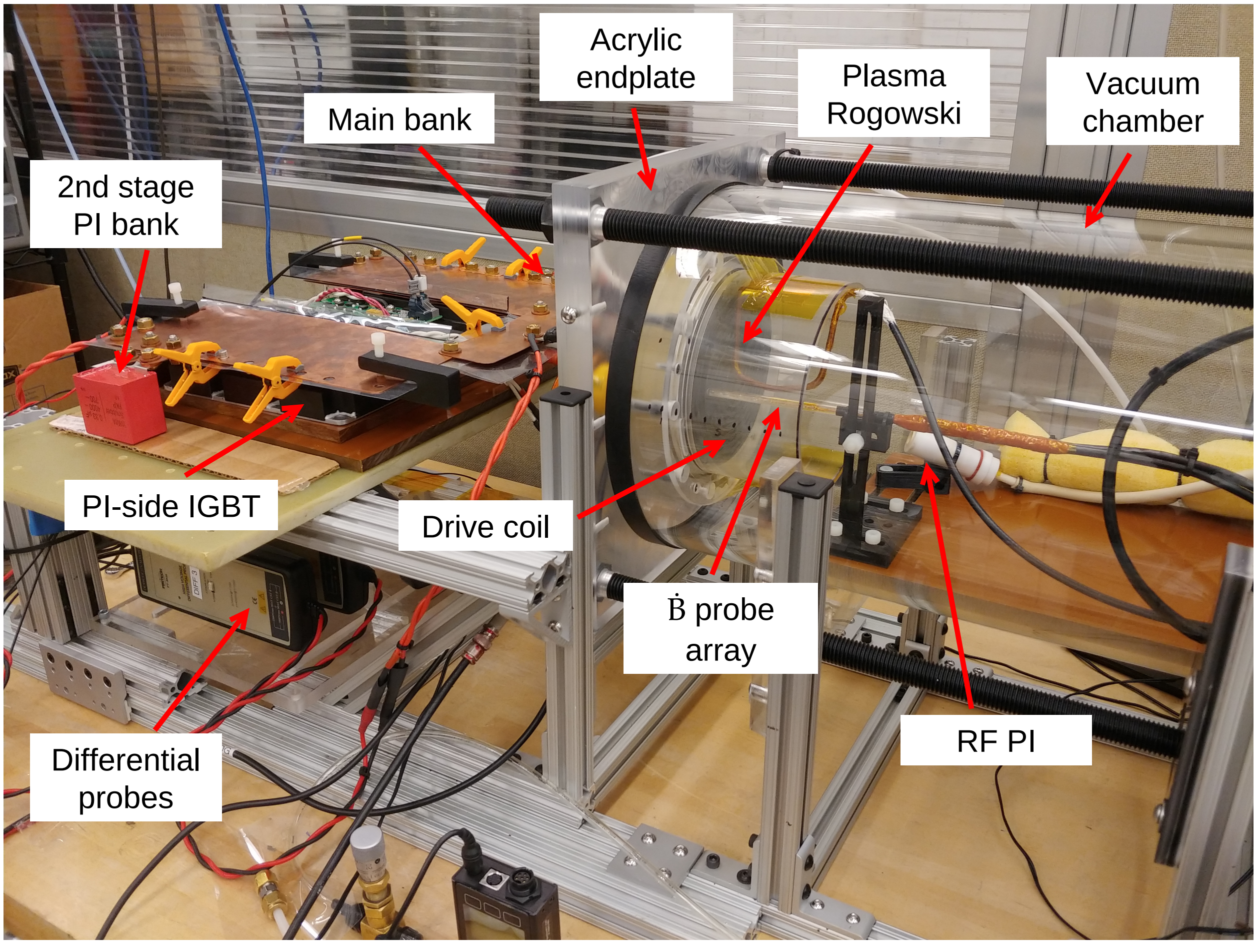

**Figure 3.5:** Image of experimental setup showing discharge circuit, drive coil, vacuum chamber, and several diagnostics.

$B$, is a superposition of the fields produced by the currents flowing in the drive coil and plasma. Idealized axial distributions of $J_\theta$ and the radial component of the total magnetic field, $B_r$, are depicted in Figure 3.3(a).

A suite of diagnostics was used to collect data from the prototype IPPT setup. These diagnostics fell into three main categories of measurements: current, voltage, and magnetic field. More information regarding the construction and calibration of several of these diagnostics may be found in Marsh[65].

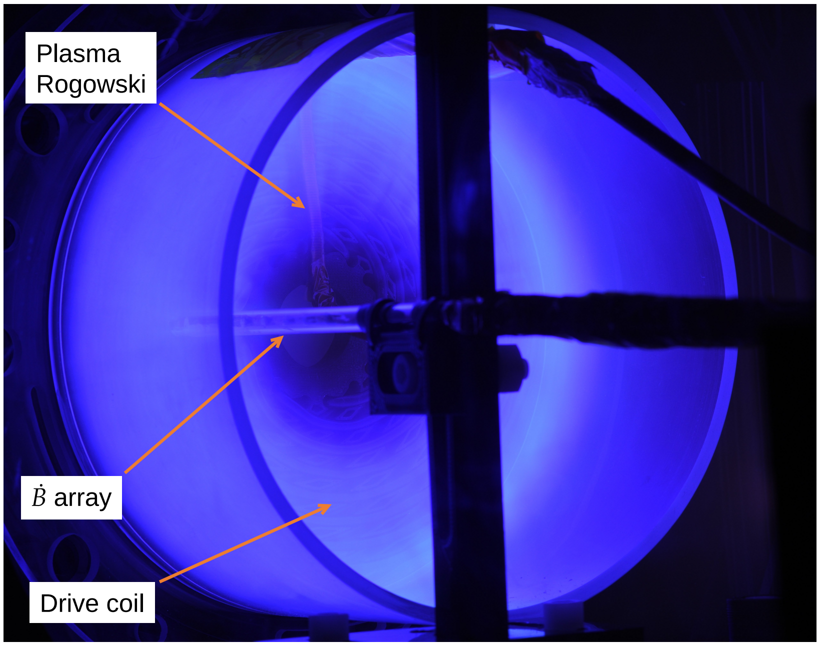

**Figure 3.6:** Long exposure ($\sim 100\,\mathrm{ms}$) DSLR image showing the $\dot{B}$ probe array and plasma Rogowski during a nominal discharge event. Fill gas is argon in this image.

*Current Measurements*

The discharge circuit current, $I_c$, was measured by a current transformer (Ion Physics CM-10-M) with 0.1 V/A sensitivity and 12 ns rise time. $I_c$ was measured at the location where the drive coil connected to the rest of the discharge circuit (see Figure 3.3(a)).

Key to our analysis is the total plasma current, $I_p$. Dailey and Lovberg reported using a Rogowski coil in the plasma region for mapping the axial variation of the azimuthal current density[11]. Following this approach, we used a rectangular (plasma) Rogowski coil whose current sensing loop encompassed the entirety of the region in which plasma was observed to measure $I_p$. This loop, depicted by the dashed region in Figure 3.3(a), extended axially from the coil face to 7 cm downstream (over twice the drive coil decoupling distance) and radially from 1.5 cm to 7.5 cm. This allowed the Rogowski to enclose the entire $J_\theta$ distribution and thus measure $I_p$.

A small $L/R$ time allowed the Rogowski to have a fast temporal response, with an estimated rise time of $\approx 30\,\text{ns}$. Comparison of discharge circuit current and voltage measurements taken with and without the plasma Rogowski installed suggested that the presence of this diagnostic did not significantly perturb the plasma. High speed imagery also provided qualitative evidence for this conclusion. Integration of the Rogowski coil output was accomplished numerically. A cubic spline was fit to the integrated data to correct for drift introduced by numerical integration of digitization noise in the signal introduced by the oscilloscope.

### *Voltage Measurements*

Differential probes with a 100 MHz bandwidth (Pintek PT-8020) were used to measure the voltage across the main capacitor bank ($V_{mb}$), 2nd-stage PI capacitor bank ($V_{pi}$) and drive coil, ($V_{\text{coil}}$). The high common mode rejection ratio (CMRR) of these probes resulted in excellent high frequency noise immunity. Any remaining high frequency noise was filtered using a forward-backward digital lowpass filter with cascaded second-order sections. The measurement of $V_{\text{coil}}$ was taken at the same location as $I_c$, i.e., where the drive coil connected to the rest of the discharge circuit.

### *Magnetic Field Measurements*

A linear $\dot{B}$ probe array consisting of four 5.6 µH chip inductors spaced $\Delta z = 1\,\text{cm}$ apart was used to measure the rate of change of the radial component of the total magnetic field, $B_r$, at the mean radius of the drive coil. When terminated at the nominal $100\,\Omega$ differential impedance, this gave an $L/R$ rise time of 56 ns. The location of this array is shown in Figure 3.3(a), with the locations of the probes relative to the depicted axial $B_r$ distribution indicated, and Figure 3.6. The first probe was located 0.5 cm from the drive coil face and 0.81 cm from the coil mid-plane. To calibrate output of the probes, a sensitivity curve was found for the range 100 kHz to 500 kHz by using a pulsed Helmholtz coil in accordance with the procedure given by Polzin et al. [66]. Integration of the $\dot{B}_r$ signals to obtain $B_r$

was achieved numerically using the same procedure for integrating data from the plasma Rogowski coil. Similar to the plasma Rogowski coil, the presence of the $\dot{B}$ probe array was not observed to significantly perturb the operation of the thruster.

## 3.3 Analysis Methods

We now present methods for determining the evolution of the inductive coupling and characteristic plasma resistance from measurements taken by the diagnostics discussed in section 3.2.2. Once determined, we seek to use this information to produce time-histories of the heating in and acceleration of the current sheet. We note that the methods presented here are general and are not limited in scope to the compact IPPT detailed in section 3.2.1.

### 3.3.1 Inductive Coupling

Applying Kirchoff's circuit laws to the two current loops in Figure 3.1(b), the voltage across the drive coil may be expressed as

$$V_{\text{coil}} = L_c \frac{dI_c}{dt} - \frac{d}{dt}\left(M I_p\right) \,, \tag{3.1}$$

where, to reiterate, $I_c$ and $I_p$ are the currents in the discharge and plasma circuits, $M$ is the mutual inductance, and $L_c$ is the drive coil inductance. Rearranging and integrating with the initial condition that the current sheet does not yet exist at starting time $t_0$, we find

$$M = \frac{1}{I_p}\left[L_c\left(I_c - I_{c,0}\right) - \int_{t_0}^{t} V_{\text{coil}}\, d\tau\right] \,, \tag{3.2}$$

where $I_{c,0}$ is the discharge circuit current at $t = t_0$ and $\tau$ is a dummy time variable for integration. In this paper, we take $t_0 = t_{sw,pi}$. Equation (3.2) shows that $M$ may be directly calculated if $L_c$ is known and $V_{coil}$, $I_c$, and $I_p$ are measured. Crucially, at this point we have made no additional assumptions beyond those inherent to the lumped-element circuit model.

It is often more convenient to examine the coupling coefficient, $k$, rather than $M$ directly, where

$$k = \frac{M}{\sqrt{L_c L_p}} \,. \tag{3.3}$$

Here, following Dailey and Lovberg [18], we approximate the shape of the current sheet as a flat annulus and estimate its inductance according to

$$L_p = \mu_0 \frac{r_a + r_b}{2} \left[ \ln \left( \frac{r_b + r_a}{r_b - r_a} \right) + 0.9 \right] , \tag{3.4}$$

where $r_a$ and $r_b$ are the inner and outer radii of the annulus, respectively, and $\mu_0$ is the permeability of free space. We assume here that $r_b$ and $r_a$ are constant and, moreover, the same as those of the drive coil. This latter assumption is equivalent to stating that the current sheet forms over the entire surface of the drive coil. Due to our assumptions, equation (3.4) yields a constant value for $L_p$, and $k$ as calculated by equation (3.3) becomes a normalization of $M$. If $L_p$ differs significantly from the value given by equation (3.4), the result given by equation (3.3) will diverge from the true value of $k$.

### *3.3.2 Plasma Resistance*

The lumped-element circuit model discussed in section 3.1 treats the plasma as a single resistor with resistance $R_p$. This bulk plasma resistance is closely related to the resistive, i.e., Ohmic, heating of the plasma, which Little et al. have shown is central to formation of the current sheet[31]. For conductors carrying time-varying currents, Ohmic heating primarily occurs within the skin depth[67]. As such, we believe that the resistance of the plasma inside the skin depth, $R_{sd}$, provides more insight into the evolution of the current sheet than the bulk plasma resistance described by $R_p$.

We evaluate the azimuthal component of Ampere's law at the mean radius of the drive coil, where we argue that the magnetic field is sufficiently radial to approximate $\partial B_z/\partial r \approx 0$. This leads to a relation between the total radial magnetic field, $B_r$, and the azimuthal current density, $J_\theta$,

$$\frac{dB_r}{dz} = \mu_0 J_\theta \, . \tag{3.5}$$

To connect our measurements of $B_r$ to $R_{sd}$, we assume that $J_\theta$ inside the current sheet may be expressed as

$$J_\theta(z) = \begin{cases} 0, & z < z_{cs} \\ J_0 \exp\left(-\dfrac{z - z_{cs}}{\delta_{fd}}\right), & z \geq z_{cs}\ , \end{cases} \tag{3.6}$$

where $J_0$ is the surface current density and $z$ and $z_{cs}$ are the axial distance of the measurement location and current sheet leading edge from the mid-plane of the drive coil, respectively.

We note that $J_0$ is not a constant but rather a function of time which captures the time dependency of the current distribution. The decay rate of $J_\theta$ in equation (3.6) is dictated by the flux penetration depth, $\delta_{fd}$, which is the transient analogue to the harmonic skin depth for a steady-state driving waveform, $\delta_{sd}$[67]. We note that since equation (3.6) considers only the axial variation of $J_\theta$, it implicitly assumes that the current sheet is radially uniform. This assumption is supported by data reported by Dailey and Lovberg[11], which showed that the axial distribution of the electric field was fairly uniform across in the radius of the coil face.

The form of $J_\theta$ proposed in equation (3.6) is motivated by a combination of theory and experiment. Theoretically, it is an approximation of the current density profile produced in a conductive half-space (or thick slab) when subjected to a transient sinusoidal magnetic field. While the driving field is increasing in magnitude, the current density profile produced due to diffusion of the field into the conductor is approximately exponential[67]. Experimentally, measurements reported by Dailey for a planar IPPT appear to show that $J_\theta$ within the primary current sheet possessed an approximately exponential profile until around the quarter cycle of $I_c$[10].

Inside the current sheet, the skin effect results in $J_\theta$ becoming phase shifted relative to the surface value, $J_0$. In turn, this causes the maximum $J_\theta$ to migrate into the sheet during the first half-cycle of $I_c$[67]. To the exponential model in equation (3.6), this phase shift is indistinguishable from bulk downstream motion of the sheet itself. As such, our assumed $J_\theta$ is only applicable before downstream diffusion becomes significant. Based on theoretical solutions to the transient diffusion equation[67] and experimental measurements of $J_\theta$ in IPPTs[10], we believe equation (3.6), and all subsequent equations which rely upon it, apply until approximately the maximum in the driving magnetic field or, equivalently, the maximum in $I_c$.

Substituting equation (3.6) into equation (3.5) and integrating produces an expression for the axial profile of $B_r$. Due to superposition, $B_r$ can be expressed as the combination of fields due to the drive coil and plasma current $B_r = B_{r_c} + B_{r_p}$, where $B_{r_c}$ and $B_{r_p}$ are the components due to the drive coil and plasma currents, respectively. By subtracting $B_{r_c}$ we can account for the spatial decay of the coil field with space and find an expression for the field due to plasma currents only

$$B_{r_p} = \mu_0 J_0 \delta_{fd} \left[ 1 - \exp\left( -\frac{z - z_{cs}}{\delta_{fd}} \right) \right] + B_{r,0} - B_{r_c}. \tag{3.7}$$

Here, $B_{r,0}$ is the value of the total radial magnetic field at the upstream surface of the current sheet.

In equation (3.7) $B_{r_c}$ is not a constant but rather itself a function of $z$. To extract this component from the measured total $B_r$, we performed a calibration to determine the response of the $\dot{B}_r$ probe array to the field produced by the drive coil alone. This resulted in a calibration curve that related $I_c$ and $B_{r_c}$ which, for cases where plasma was present, allowed $B_{r_c}$ to be determined from the measured $I_c$.

By measuring $B_r$ at various $z$ locations and then subtracting the corresponding $B_{r_c}$, a measured profile for $B_{r_p}$ can be generated to which equation (3.7) can be fit. The fit parameters are $\delta_{fd}$, $J_0$, and $z_{cs}$. $B_{r,0}$ was taken to be the maximum $B_r$ measured by the array. We note that this assumes that at least one probe is always upstream of $z_{cs}$.

Once $\delta_{fd}$ has been found from the fit, it may be used to find $\delta_{sd}$. While the magnitude of the driving field is rising, it can be shown[67]

$$\delta_{sd} \approx \frac{4}{3} \delta_{fd}\,. \tag{3.8}$$

With $\delta_{sd}$ known, we determine the bulk resistivity in the current sheet from

$$\rho_{sd} = \frac{1}{2} \mu_0 \omega_{I_p} \delta_{sd}^2\,, \tag{3.9}$$

where $\omega_{I_p}$ is the angular frequency of the bulk plasma current. Since we are interested in the variation of $\rho_{sd}$ on timescales faster than the waveform half-period, we use the instantaneous frequency of $I_p$ via the Hilbert transform method [68]. This gives $\omega_{I_p}$ at each time step that $\delta_{sd}$ is calculated.

Using equation (3.9), we express the effective skin depth resistance within the current sheet as

$$R_{sd} = \frac{\pi}{2}\left(\frac{r_b + r_a}{r_b - r_a}\right)\mu_0 \omega_{I_p} \delta_{sd}\,. \tag{3.10}$$

So long as any plasma outside of the skin layer acts as a parallel resistance, $R_{sd} > R_p$. We also note that, while we have followed Polzin et al.[29] and Little et al.[31] in treating the current sheet as a homogeneous plasma annulus whose radial dimensions are assumed to match those of the drive coil, Sharma et al. reported the appearance of prominent spokes during the sheet formation process[69]. Such structures may result in azimuthal variation in the plasma resistivity and necessitate considering a distributed or at least series resistance during the time over which these spokes are present.

### *Current Sheet Width*

The current density profile in equation (3.6) can also be used to estimate the width of the current sheet, $w_{cs}$. If we assume that the bulk of the plasma current is carried within the sheet, we may approximate

$$I_p \approx \int_{r_a}^{r_b} \int_{z_{cs}}^{z_{cs}+w_{cs}} J_0 \exp\left(-\frac{z - z_{cs}}{\delta_{fd}}\right) drdz\,. \tag{3.11}$$

Performing this integral and rearranging the resulting terms, we find the current sheet width is given by

$$w_{cs} \approx -\delta_{fd} \log\left[1 - \frac{I_p}{(r_b - r_a)\, J_0 \delta_{fd}}\right]\,. \tag{3.12}$$

When the current sheet is much wider than the skin depth, we find

$$J_{\theta,0} \approx \frac{I_p}{(r_b - r_a)\,\delta_{fd}} \sim \frac{I_p}{\delta_{fd}}\,. \tag{3.13}$$

The surface current density is thus expected to scale with the ratio of $I_p$ and $\delta_{sd}$ when $w_{cs} \gg \delta_{fd}$. We reiterate that, since equation (3.12) relies upon equation (3.6), it is limited in validity to before the maximum in $I_c$.

### *3.3.3 Power Analysis*

As previously discussed, inductive coupling and the plasma resistance are closely related to the motion of and energy deposition in the current sheet. Energy input into the sheet is primarily accomplished through Ohmic heating of the electron population. In keeping with our use of $R_{sd}$ instead of $R_p$, instead of the total Ohmic heating of the plasma we examine heating within the skin depth,

$$P_{oh_{sd}} \approx I_{sd}^2 R_{sd}\,, \tag{3.14}$$

where $I_{sd}$ is the total current within the skin depth ($\delta_{sd}$) and $R_{sd}$ is calculated from equation (3.10). When $w_{cs} \gg \delta_{sd}$, it may be found from integration of equation (3.6) that $I_{sd} \approx 0.75\, I_p$, i.e., that nearly two thirds of the total plasma current is carried within the skin layer. The localized skin depth heating given by equation (3.14) is thought to be more relevant to current sheet formation than the total plasma Ohmic heating obtained by using the bulk plasma resistance, $R_p$.

The power associated with electromagnetic acceleration of a rigid conductor can be expressed as

$$P_{em} = -I_c I_p \frac{dM}{dt}\,. \tag{3.15}$$

We note that the sign convention in this equation has been taken such that positive $I_c$ and $I_p$ are flowing in opposing directions. Positive accelerating power is thus produced when $dM/dt$ is negative, which corresponds to sheet translation in the downstream direction.

In the case of a current sheet, changes in the shape of the sheet, e.g. due to ionization, will also cause changes in $M$. To isolate changes in $M$ resulting from bulk motion of the sheet, we use the chain rule to convert $dM/dt$ to the product of $dM/dz_{cs}$ and $dz_{cs}/dt$. To evaluate $dM/dz_{cs}$, we use the empirical equation[46]

$$k = k_0 \exp\left(-\frac{z_{cs}}{z_{dc}}\right) , \tag{3.16}$$

where $z_{cs}$ is the axial distance of the upstream edge of the current sheet from the coil mid-plane and $z_{dc}$ is the decoupling distance of the coil. $k_0$ is a constant parameter, typically determined by fitting data obtained by using a conductive "dummy load" as a stand-in for the plasma[46]. Using equations (3.3) and (3.16), we find

$$P_{em} = \frac{I_c I_p M}{z_{dc}} \frac{dz_{cs}}{dt} . \tag{3.17}$$

Similarly, the total instantaneous electromagnetic force on the current sheet can be approximated as

$$F_{em} = \frac{I_c I_p M}{z_{dc}} . \tag{3.18}$$

Notably, calculation of $F_{em}$ does not require knowledge of $z_{cs}$. We note that $F_{em}$ is equivalent to integrating the Lorentz force density over the volume of the current sheet at any given time. $F_{em}$ is only equal to the instantaneous thrust produced by the IPPT when the current sheet may be treated as a solid body. The time-averaged electromagnetic force on the sheet may be found by integrating equation (3.18) with respect to time and multiplying by the pulse rate of the thruster.

## *3.4 Results and Analysis*

### *3.4.1 Circuit Measurements*

The mutual inductance as a function of time was found from equation (3.2) by using experimentally measured waveforms for $I_c$, $I_p$, and $V_{\text{coil}}$. Figure 3.7 shows a typical set of measured waveforms for a vacuum (no plasma) and a representative plasma case when using argon as the fill gas. We note that the data in Figure 3.7 is for a single discharge event and that the error bands represent the uncertainty associated with the estimated measurement error associated with the relevant diagnostic. The uncertainty due to variance between discharges was

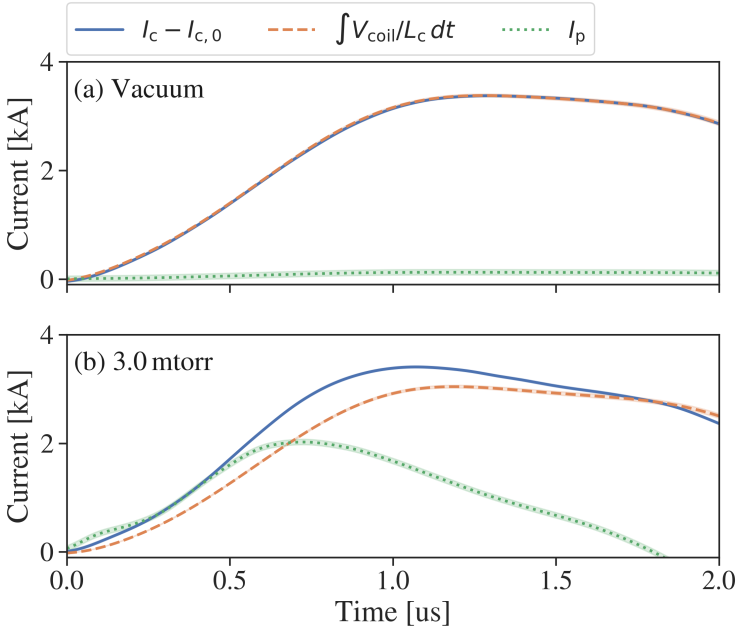

**Figure 3.7:** Comparison of experimentally measured waveforms of $I_c$, $I_p$, and integrated $V_{\text{coil}}$ used to calculate the mutual inductance between a (a) vacuum and (b) a representative plasma case. For the plasma case, $p_0 = 3\,\text{mTorr}$ (0.4 Pa), $V_{pi,0} = 1\,\text{kV}$, $V_{mb,0} = 2\,\text{kV}$, and the fill gas was argon.

found to be no more than a couple percent, and could be accounted for by the measurement uncertainty. Similar excellent repeatability has been observed in other pulsed EP devices, namely pulsed plasma thrusters[70].

In the absence of a coupled plasma load, the circuit should behave like a transformer with an open secondary. In this case, $I_c - I_{c,0}$ and $\int V_{\text{coil}}/L_c\,dt$ should be equal, as seen in Figure 3.7(a). Figure 3.7(b) shows that all three terms, i.e., $I_p$, $I_c - I_{c,0}$, and $\int V_{\text{coil}}/L_c\,dt$ are affected by the presence of plasma. While both $I_p$ and the difference between $I_c - I_{c,0}$ and $\int V_{\text{coil}}/L_c\,dt$ appear to grow, the effect on the coupling will depend on their ratio. To avoid a singularity, equation (3.2) necessitates that the bracketed term goes to zero at the same time as $I_p$. Graphically, this means that the curves of $I_c - I_{c,0}$ and $\int V_{\text{coil}}\,dt/L_c$ should intersect at zero-crossings of $I_p$. Figure 3.7(b) shows this occurs to within the measurement uncertainty.

### *3.4.2 $B_r(z)$ Curve Fits*

Figure 3.8 shows the total $B_r$ waveforms measured by each of the four probes in the array. From this total $B_r$, the components due to the coil and plasma currents were extracted using the calibration curve method described in section 3.3.2. The waveforms of these components are also shown in Figure 3.8. Similar to the circuit data, the magnetic field probe data was found to be highly repeatable, with variance between repeated measurements found to be largely attributable to the measurement uncertainty of the diagnostic.

The magnitude of the total field relative to the coil component can be used to estimate the position of the current sheet. When the sheet is downstream of a probe, its magnetic field will be in the same direction as that produced by the coil and the total field will be larger than the coil component alone. This effect is more pronounced the closer the probe is to the leading edge of the current sheet. As the sheet passes over the probe, the fields produced by plasma upstream and downstream of the probes will be in opposing directions. This can equivalently be thought of as a screening effect, wherein the upstream plasma blocks some of the field produced by the drive coil from reaching the probes. Due to this behavior, $B_r$ will become less than $B_{r_c}$.

At some point within the sheet, the $B_{r_p}$ produced by the upstream and downstream plasma will be equal and cancel. This point corresponds to $B_{r_p} = 0$ or, equivalently, a crossing of the $B_r$ and $B_{r_c}$ curves, which is demarcated in Figure 3.8 by the cross symbols. Since we are only interested in crossings due to translation of the sheet, we track only the last of these crossings for each probe (ignoring crossings that are due to $I_p = 0$). When data from a probe, e.g. probe one in Figure 3.8, does not display crossings, this suggests that the sheet forms downstream of this probe.

By taking the value of $B_{r_p}$ at a given time for each of the four probes in the array, a curve for the axial variation of $B_{r_p}$ can be obtained, to which equation (3.7) can be fit. Figure 3.9

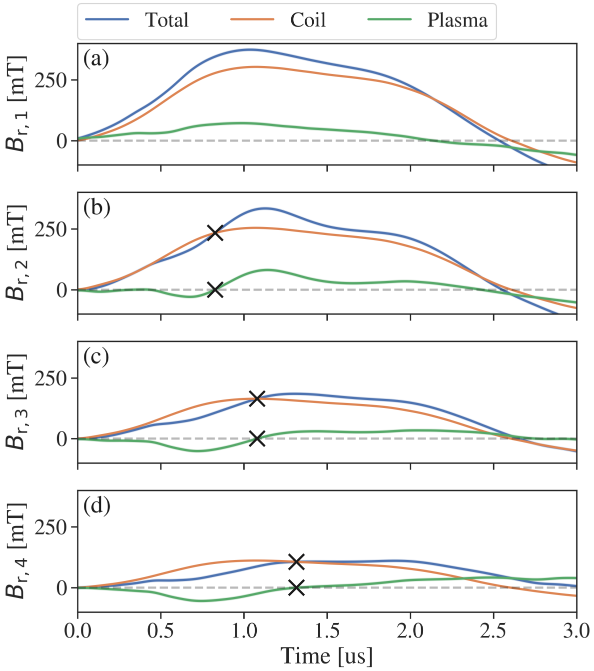

**Figure 3.8:** Measured $B_r$ from linear $\dot{B}$ probe array for nominal operating conditions and $p_0 = 3\,\mathrm{mTorr}$ (0.4 Pa, argon). Probes were stationed at axial distances of (a) 0.5 cm, (b) 1.5 cm, (c) 2.5 cm, and (d) 3.5 cm from the coil face.

shows $B_{r_p}$ as a function of the axial coordinate, $z$, for nine time slices. We observe that the data follows an exponential decay, lending confidence to our use of equation (3.7). The dashed black line is the curve obtained by performing a nonlinear weighted least-squares fit of equation (3.7) to the data; good agreement between the fitted curve and the data was generally achieved.

The current sheet location, $z_{cs}$, calculated from the fit is marked in Figure 3.9 by the vertical blue dashed line. We note that reliable fits are not achieved until $t > 0.16\,\mu\mathrm{s}$. This is because the curve fitting procedure requires the number of points inside the plasma to be greater than or equal to the number of fit parameters, i.e., three. At small time, the $B_{r_p}$ measured by the downstream probes are still indistinguishable from zero and thus cannot be meaningfully included in the fit.

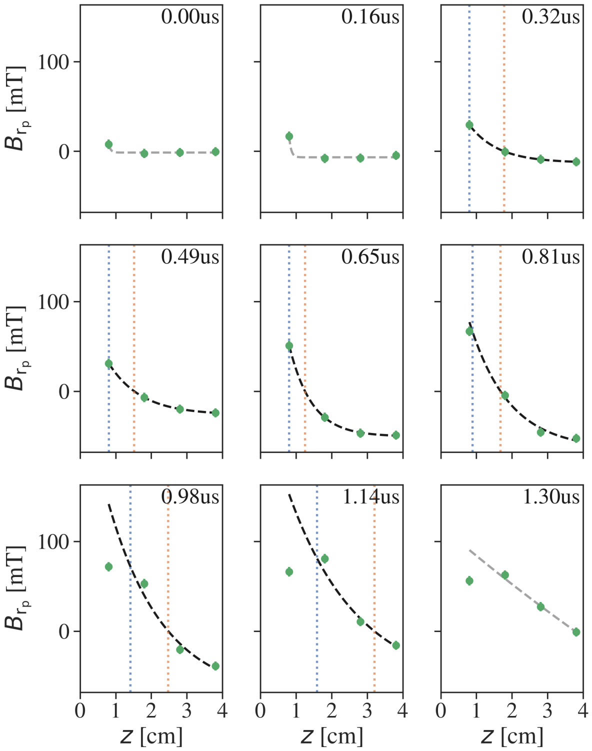

**Figure 3.9:** Fits produced by weighted non-linear least squares curve fitting of $B_{r_p}$ data measured by a linear $\dot{B}_r$ probe array for $p_0 = 3\,\text{mTorr}$ (0.4 Pa, argon).

In addition to the location of the current sheet leading edge, the location of the point inside the sheet where $B_{r_p} = 0$ can also be tracked. In this case, the fit procedure is carried out in the same manner but with $B_{r,0} - B_{r_c} = 0$. The location of this so called "null point", $z_{\text{null}}$, is shown in Figure 3.9 by the orange dotted lines. The distance between the leading edge and null point locations can be used as an indication of the width of the sheet. We note that only changes in $z_{cs}$ are unambiguously associated with bulk motion of the sheet. This is because $z_{null}$ is influenced by not only the location of the sheet, but also its width and the internal distribution of current.

Examining Figure 3.9, we find that plasma appears to form between probes one and two sometime before the 0.32 µs mark. As time progresses, we see evidence of a plasma region that is broadening while remaining mostly stationary. The field measured by probe one increases while the field measured by probes three and four becomes more negative, suggesting a growth in the plasma current. At 0.65 µs, we see the $B_{r_p}(z)$ profile has steepened significantly between probes one and two. This points towards the broader plasma region narrowing into what may be a magnetically impermeable current sheet.

At 0.98 µs, we see the first indication of significant sheet motion, with $z_{cs}$ moving downstream of probe 1. By 1.14 µs, the $B_{r_p}$ measured at probe two increases above that measured at probe one, indicating the greater proximity of $z_{cs}$ to this probe. The sheet is also observed to broaden as it translates, with the difference between $z_{cs}$ and $z_{\text{null}}$ increasing between 0.65 µs and 1.3 µs. Beyond 1.3 µs, evidence suggests $z_{cs}$ has moved beyond probe two and insufficient downstream probe data exists to continue the fitting procedure.

The effects of the fit weighting become apparent at 0.98 µs. We observe that the probe one measurement is weighted less as the current sheet moves away, effectively ensuring that only points in or downstream of the current sheet are being included in the fit. The weighting is empirical and determined based on the position of the null point relative to the probe location. Specifically, the weighting is accomplished by assigning standard deviations of errors in the data according to

$$\sigma_{B_{fit}} = \left( \frac{z_{null}}{z_{probe}} \right)^2 , \tag{3.19}$$

where $\sigma_{B_{fit}}$ is the standard deviation of errors assigned to the $B_{r_p}$ data used in the fit, $z_{\text{null}}$ is the position of the null point relative to the coil mid-plane, and $z_{\text{probe}}$ is the probe location. We note that the values calculated from equation (3.19) are strictly assigned for the purposes of curve fitting and do not represent the actual measurement uncertainty.

## *3.5 Current Sheet Evolution*

The time evolution of key current sheet parameters and derived quantities are presented in Figure 3.10 for a representative plasma case. From Figure 3.10 we observe what appears to be three distinct phases: ionization, formation, and acceleration. The boundaries between these phases are roughly demarcated by the vertical dashed lines.

Data for the parameters obtained from the $B_{r_p}$ fits was generally not available immediately at $t = 0$. This is because, as discussed in section 3.4.2, the curve fitting procedure required at least three probes to be inside the plasma. With the present axial probe spacing, it was uncertain whether this criteria was met until after some finite time. This lack of suitable fit points at early time is shown in Figure 3.9, which shows that only the first probe measured fields appreciably different from zero until somewhere between $0.16\,\mu\text{s}$ and $0.32\,\mu\text{s}$. We have thus chosen to omit data before $t \approx 0.2\,\mu\text{s}$, which we have identified as a conservative estimate of when sufficient data exists to perform the curve fitting procedure.

While $k$ may be calculated at any time $t \geq 0$, the uncertainty in this parameter tends to be large at early times due to the relatively small values of $I_c$, $I_p$, and the integral of $V_{\text{coil}}$, which make the uncertainty in these values proportionally large. For our discussion we have thus chosen to limit the plotted values of $k$ to the same time region as the parameters obtained from the $B_{r_p}$ fits so that we may always have data from an independent diagnostic with which to corroborate.

Despite the lack of data in the first $\approx 0.2\,\mu\text{s}$, we may infer some information regarding the nature of the plasma in the early time by examining the initial values of the variables as they first appear in Figure 3.10. At $t = 0.2\,\mu\text{s}$, $I_p$ is small but clearly present. Inductive coupling is moderately high ($k \approx 0.7$), which indicates the presence of plasma relatively close to the coil face. This plasma is the result of the initial coupling between the drive coil and any plasma generated by the second-stage PI system. $R_{sd}$ and $\delta_{sd}$ are fairly low, which would suggest that the initial plasma is relatively high temperature. Due to the small initial $\delta_{sd}$, the initial $J_0$ is significant despite the rather small $I_p$.

Figures 3.10(f,g) show $z_{cs}$ at or upstream of probe one ($\leq 0.712\,\text{cm}$) and $z_{\text{null}}$ slightly downstream between probes one and two ($1.45\,\text{cm}$). Consistent with the initial position data, $w_{cs}$ is observed to be narrow at $t = 0.2\,\mu\text{s}$. Ohmic heating is initially small, as a result of the small $I_p$ and $R_{sd}$. Similarly, $F_{em}$ and $P_{em}$ are also close to zero, indicating little acceleration of the plasma occurs before $t = 0.2\,\mu\text{s}$. The small $w_{cs}$ and negligible $P_{oh_{sd}}$, $F_{em}$,

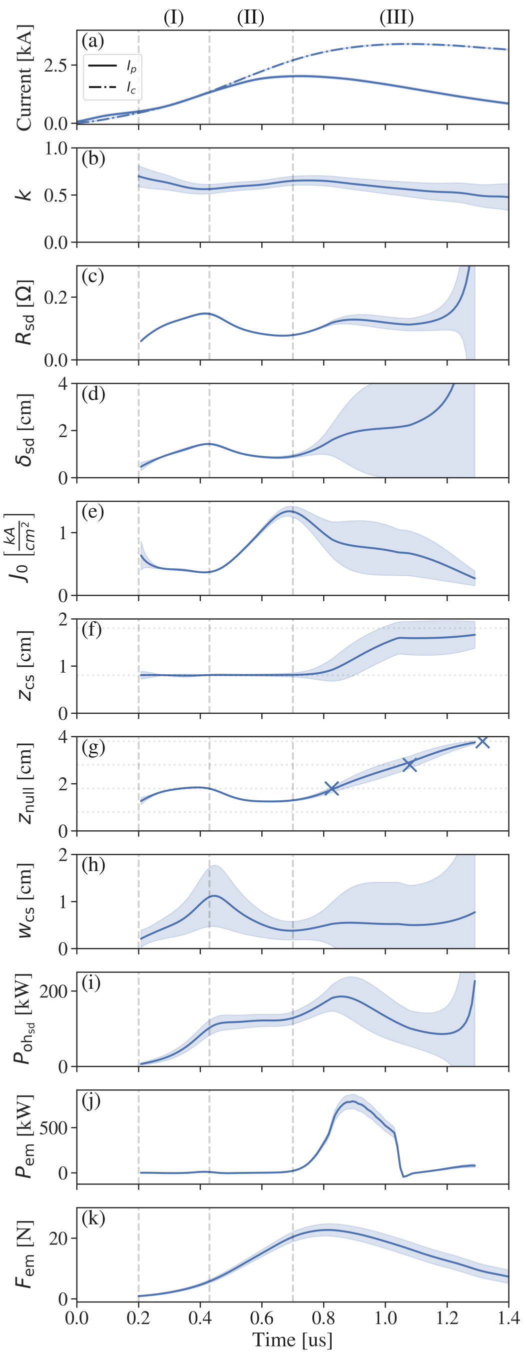

**Figure 3.10:** Temporal evolution of (a) $I_c$ and $I_p$, (b) $k$, (c) $R_{sd}$, (d) $\delta_{sd}$, (e) $J_0$, (f) $z_{cs}$, (g) $z_{null}$, (h) $w_{cs}$, (i) $P_{oh_{sd}}$, (j) $P_{em}$, and (k) $F_{em}$ for $V_{mb,0} = 2\,\mathrm{kV}$, $V_{pi,0} = 1\,\mathrm{kV}$, and $p_0 = 3\,\mathrm{mTorr}$ (0.4 Pa, argon). Phases are labeled (I) ionization, (II) formation, and (III) acceleration.

and $P_{em}$, however, suggest that the initial plasma formed from a relatively small region that was heated locally, and that the bulk of the fill gas remains largely un-ionized.

The ionization phase covers $0.2\,\mu\text{s} \lesssim t \lesssim 0.45\,\mu\text{s}$ in Figure 3.10. During this phase, $I_p$ continues to rise. $k$ is found to decrease, while $R_{sd}$ and $\delta_{sd}$ rise. $J_0$ remains relatively flat or even slightly decays during this phase due to the rise in $\delta_{sd}$. While the upstream edge shows little movement, $z_{\text{null}}$ is found to move downstream. Correspondingly, we see $w_{cs}$ broaden. $P_{oh_{sd}}$ rises substantially while $F_{em}$ increases modestly. $P_{em}$ remains vanishingly small as a result of negligible movement in $z_{cs}$.

The decline in $k$ combined with downstream movement in $z_{\text{null}}$, a static $z_{cs}$, and increasing $w_{cs}$ points towards a broadening region of ionization. The rise in $R_{sd}$ and $\delta_{sd}$ indicate a cooling plasma, which is consistent with the quenching of the early-time electron population due to inelastic collisions with surrounding neutrals found by Little et al.[31] The growth in $P_{oh_{sd}}$ while $F_{em}$ remains small and $P_{em}$ is close to zero suggests that the gas is being ionized without significant acceleration. The decline in $k$ is thus thought to be due to a broadening current distribution rather than bulk downstream motion of the plasma. This aligns with the observation that $J_0$ remains flat despite $I_p$ increasing, which is also predicted by the scaling of equation (3.13).

The formation phase covers $0.45\,\mu\text{s} \lesssim t \lesssim 0.7\,\mu\text{s}$ in Figure 3.10. In this phase, $k$ begins to increase again while $R_{sd}$ and $\delta_{sd}$ decrease. A marked rise in $J_0$ also occurs during this phase, which is attributed to the continued increase in $I_p$ and narrowing of $\delta_{sd}$. Although $z_{cs}$ remains largely stationary, $z_{\text{null}}$ is now found to move upstream, which results in a narrowing $w_{cs}$. $P_{oh}$ remains high, but the rate of increase is found to plateau. $F_{em}$ continues to grow, although significant $P_{em}$ is again not observed due to the stationary $z_{cs}$.

The combination of an increase in coupling, rise in $J_0$, and upstream motion of $z_{\text{null}}$ while $z_{cs}$ remains stationary points towards current becoming increasingly concentrated towards the coil-facing (upstream) edge of the sheet. This agrees with the decrease in $\delta_{sd}$, which indicates that current and heating are being localized in an increasingly thin layer. The decrease in $R_{sd}$ while $P_{oh_{sd}}$ remains high suggests that heating power is being preferentially deposited in this narrowing region. We posit that the strong heating of a narrowing region of plasma accompanied with the rapid rise in current density and decrease in skin depth that occurs during this phase is evidence of the formation of a well-defined current sheet that is at least partially magnetically impermeable.

While the initial energy deposited in the plasma is used to overcome quenching due to cold neutrals, as the plasma region broadens and ionization continues, the neutral population near the upstream edge should reduce. We hypothesize that this allows more of the deposited energy to go into heating the electrons and raising the plasma temperature. This increase in temperature decreases the resistivity and, accordingly, the skin depth. The continuation of this feedback cycle causes heating to become increasingly localized near the upstream edge, resulting in the concentration of current in this area. This effect is likely enhanced due to $k$ being higher closer to the coil face, and thus the upstream edge of the sheet.

Dailey and Lovberg showed that the strength of the axial electric field, $E_z$, at any point within the current sheet was determined by a combination of the local $J_\theta B_r$ Lorentz force and axial electron pressure gradient[11]. Confinement of $I_p$ to a narrower region should increase the local $J_\theta B_r$, while concentration of Ohmic heating is anticipated to steepen the electron pressure gradient due to locally increasing the electron density and temperature. As such, we postulate that the upstream localization of the plasma current and Ohmic heating is closely related to both the appearance and the spatial distribution of the strong $E_z$ responsible for accelerating the ions in the sheet.

The acceleration phase extends from $t \gtrsim 0.7\,\mu\text{s}$, which corresponds approximately with the maximum in $I_p$, until the end of the data collection window shown in Figure 3.10. During this phase, $k$ undergoes a consistent, substantial decline. $R_{sd}$ and $\delta_{sd}$ increase, moderately at first, then somewhat more gradually, and finally sharply as the plasma current decays towards zero. $J_0$ falls during this period and does so at a rate that is initially faster than the decline in $I_p$.

Significant downstream motion of $z_{cs}$ is observed for the first time during this phase. $z_{\text{null}}$ also moves downstream at a similar rate, which is in agreement with the only modest increase in $w_{cs}$ during this phase. Ohmic heating in the skin layer reaches a maximum near the start of the acceleration phase but then quickly decreases. $F_{em}$ peaks at the start of this phase as well which, along with the motion of $z_{cs}$, results in significant power going into acceleration of the sheet. Both $F_{em}$ and $P_{em}$ peak between the maxima in $I_c$ and $I_p$, which appears reasonable based on the linear dependencies found in equations (3.17) and (3.18).

The decrease in $k$ while both $z_{cs}$ and $z_{\text{null}}$ move downstream suggests that the current sheet experiences cohesive translation during the acceleration phase. The slight delay in the motion of $z_{cs}$ relative to $z_{\text{null}}$ may be related to the structure $E_z$, which has been reported to be weaker near the upstream edge of the sheet due to the electron pressure gradient in this region[11]. While some of the decrease in $k$ may be the result of a broadening of the current distribution, the limited increase in $w_{cs}$ during this phase indicates that a substantial part of the decrease in coupling is due to bulk current sheet motion. Figure 3.10(f) indicates that peak sheet velocities of roughly 30 km/s to 40 km/s were obtained, which is in line with simulated values reported for comparable IPPTs[31, 71].

Simulated and experimental results reported in the literature, e.g., [31, 16], show that the current sheet interacts with ambient background neutrals it encounters as it translates. The two primary mechanisms of interaction are thought to be inelastic, i.e., ionization and excitation, collisions and charge exchange reactions. Ionization or excitation of ingested neutrals will cool the sheet, which is consistent with the increases in $\delta_{sd}$ and $R_{sd}$ during the acceleration phase observed in Figures 3.10(c,d). Figure 3.10(i) shows that $P_{oh_{sd}}$ initially increases despite $I_p$ beginning to decline, suggesting that energy is being expended to heat the newly encountered downstream gas.

Later in the acceleration phase, the reduction in coupling, alongside the natural circuit oscillation, leads to an eventual decline in $I_p$ and, accordingly, $P_{oh_{sd}}$. The increase in $R_{sd}$ and $\delta_{sd}$ at this later time is consistent with a current sheet that is receiving less energy from the drive coil due to the reduction in the inductive coupling that occurs as it moves downstream. Once losses in the sheet become greater than the energy deposited via Ohmic heating, the current sheet is expected to become less well-defined and more permeable to the accelerating magnetic fields. This increased permeability, in turn, reduces the electromagnetic accelerating power to and force on the sheet, which we see in Figures 3.10(j,k).

An abrupt knee in $z_{cs}$ is observed later in the acceleration phase at around the peak in $I_c$. Similar flattening of the sheet position was also seen around this time in experimental data reported by Polzin[16] and in simulations performed by McCulloh et al. [71]. We posit that this phenomenon is due to the entrainment of ambient gas by the sheet as it translates.

Figure 3.10 shows that knee in $z_{cs}$ occurs at a time when $\delta_{sd}$ and $R_{sd}$ are relatively flat. As such, it seems unlikely that it is the result of a sudden increase in ionization or excitation reactions. Instead, we hypothesize that a significant rise in charge exchange reactions occurs around this time. This conjecture is drawn from simulation results reported by McCulloh et al., which show that the "transparency" of the sheet to charge exchange reactions decreases dramatically until around the time that $I_c$ approaches its maximum. Since the ions formed in the sheet by charge exchange reactions are initially mostly stationary relative to the sheet, their acceleration to the sheet speed will sap momentum from the sheet and reduce its velocity.

The downstream motion of the sheet also leads to a marked increase in the uncertainties for parameters which come from the $\dot{B}_{r_p}$ fits. This is due to the weighting procedure described in section 3.4.2, which performs a weighted fit by assigning larger uncertainties to measurements taken by $\dot{B}$ probes which are upstream of $z_{\text{null}}$. We observe from Figures 3.9 that the growth in the uncertainties in the fit parameters in Figure 3.10 corresponds approximately with the time at which $z_{\text{null}}$ crosses the second probe location. As $z_{\text{null}}$ moves further downstream, the uncertainty in the $B_{r_p}$ from probe two becomes larger, and the fit is effectively being performed using only the measurements from probes three and four. This consequently leads to a significant increase in the fit parameter uncertainty.

Figure 3.10(a) shows that the peak in $I_c$ occurs in the later portion of the acceleration phase ($\approx 1\,\mu\text{s}$). Since $I_c$ is responsible for the driving magnetic field, $B_r$ will be rising until this time. This suggests that our assumed current density profile (equation (3.6)) is valid until well into the acceleration phase. Since the uncertainty in the fit parameters is already significant in this region due to the reduction in downstream points available for fitting, we believe any additional error introduced by our assumed $J_\theta$ is minimal.

Comparing the width shown in Figure 3.10(h) to the $B_{r_p}(z)$ profiles shown in Figure 3.9, we observe that the $w_{cs}$ predicted by equation (3.12) tends to be smaller than the current sheet width inferred from the spatial decay of $B_{r_p}$. This is most apparent in the acceleration phase, where Figure 3.9 suggests the sheet gets significantly wider while Figure 3.10(h) predicts $w_{cs}$ remains relatively small, albeit with large uncertainty. We believe this is due to the sensitivity of equation (3.12) to the radii terms inside the natural logarithm. While we have assumed that the radial extent of the plasma remains constant, it is possible that it may vary. A smaller $r_b - r_a$ than assumed would result in an underestimate of $w_{cs}$.

The phases observed in Figure 3.10 suggests a general sequence of events for the evolution of the current sheet in a planar IPPT. First, a plasma is produced sufficiently close to the coil face, either by PI or the initial portion of the main discharge, that strong inductive coupling can be achieved. Next, the coupling between the drive coil and initial plasma results in the generation of significant bulk plasma current. Ohmic heating rises as surrounding neutrals attempt to quench the initial plasma, which increases the resistivity and results in ionization of a broader region of gas. If power deposition by Ohmic heating is sufficient to overcome energy losses due to quenching, both plasma current and heating become increasingly localized towards the upstream edge of the plasma.

If the current density and conductivity of this region become sufficiently high, it becomes magnetically impermeable and a well-defined current sheet is formed. Once this occurs, the electromagnetic force is able to produce bulk motion of the sheet and acceleration of the sheet to high velocity occurs. The lifetime and trajectory of the sheet are influenced by both the interaction of the sheet with ambient gas it encounters and the rate at which energy deposition into the sheet diminishes due to the reduction in coupling as it translates. Once losses in the sheet exceed energy input by the drive coil, the sheet begins to decay and lose its magnetic impermeability.

## *3.6 Effects of Varying Pressure and PI*

We now use the methods of section 3.3 to investigate the effects of varying fill pressure ($p_0$) and initial PI capacitor bank voltage ($V_{pi,0}$). The fill pressure is related to the neutral density, $n_0$, in front of the drive coil. $p_0$ may thus be considered a proxy for the mass bit or, in cases when gas is injected in steady-state, the mass flow rate. Meanwhile, the degree of PI is related to the design of the IPPT discharge circuit and, more specifically, the required current rise rate. This can have an impact on the mass of the IPPT, since larger current rise rates are associated with increased electrical component mass. For cases where $p_0$ was varied, $V_{mb,0} = 2\,\mathrm{kV}$ and $V_{pi,0} = 1\,\mathrm{kV}$. For cases where $V_{pi,0}$ was varied, $V_{mb,0} = 1.5\,\mathrm{kV}$ and $p_0 = 3\,\mathrm{mTorr}$ ($0.4\,\mathrm{Pa}$). The fill gas was argon for all cases presented in this section.

### *3.6.1 Effects of Varying Pressure*

Figure 3.11 shows the effects of varying $p_0$, or equivalently $n_0$, on the evolution of the current sheet properties and derived quantities. Increasing $p_0$ is found to substantially increase the bulk current driven in the plasma. $I_c$ is increased slightly as well and is found to have a slightly faster rise time, both of which indicate a drop in the effective inductance seen by the discharge circuit and improved inductive coupling between the drive coil and plasma.

The increase in initial $k$ suggests that the PI plasma forms closer to the coil face at higher $p_0$. This is supported by the position data in Figures 3.11(f,g), which show that, while $z_{cs}$ remains similar between cases, the initial $z_{\mathrm{null}}$ moves upstream as pressure is increased. Similar shifts in the initial position of the current sheet were also reported by Polzin[16], who found that lower pressures resulted in the sheet forming further downstream in a planar IPPT, and Hallock et al.[72], who reported sheets formed further upstream as pressure was increased in a conical theta pinch IPPT.

Coupling remains higher throughout the ionization and formation phases at higher $p_0$, indicating that plasma remains closer to the coil face as the sheet forms. This again agrees with the position data during these phases, which show a static $z_{cs}$ but more pronounced

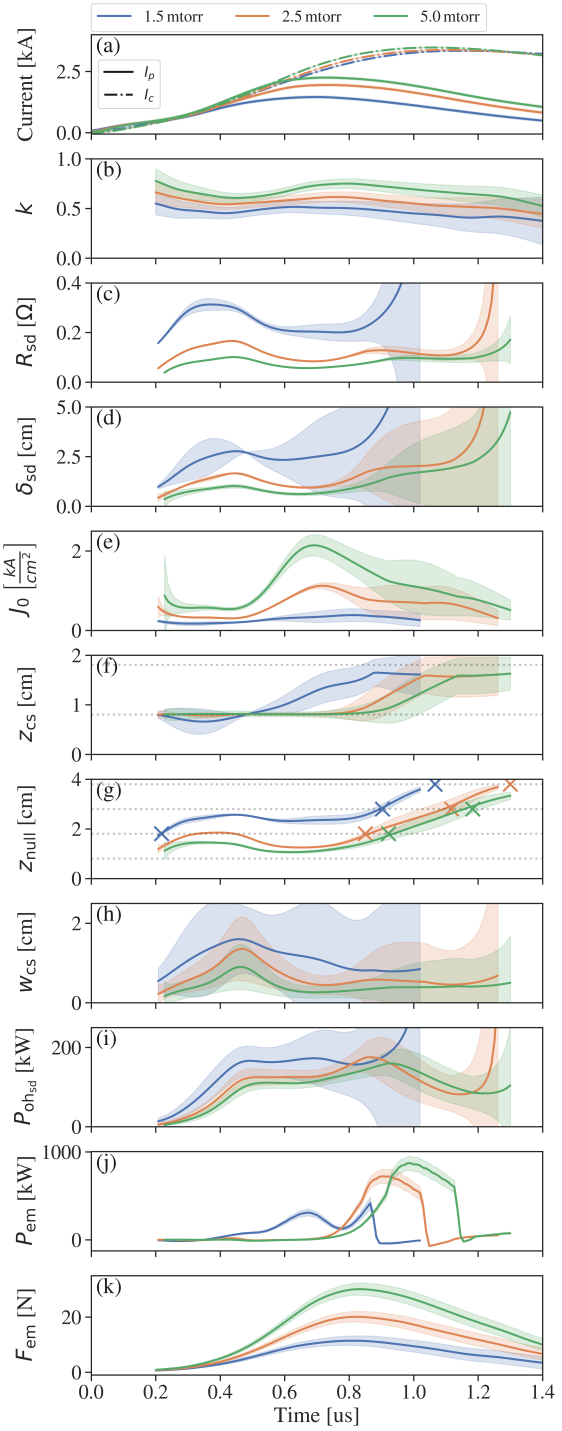

**Figure 3.11:** Effects of varying $p_0$ on the temporal evolution of (a) $I_c$ and $I_p$, (b) $k$, (c) $R_{sd}$, (d) $\delta_{sd}$, (e) $J_0$, (f) $z_{cs}$, (g) $z_{null}$, (h) $w_{cs}$, (i) $P_{oh_{sd}}$, (j) $P_{em}$, and (k) $F_{em}$. Here, $V_{mb,0} = 2\,\text{kV}$, $V_{pi,0} = 1\,\text{kV}$, and the fill gas was argon.

upstream motion in $z_{\text{null}}$ at higher $p_0$. Skin depth and current sheet width are found to decrease across all phases as fill pressure is increased. The rise in $J_0$ during the formation phase is also observed to increase markedly with pressure, with the rate of increase being notably faster than that of $I_p$. Combined, these trends point towards the upstream localization effect becoming stronger at higher $p_0$.

More pronounced upstream localization may explain the somewhat counterintuitive decrease in $R_{sd}$ observed with increasing fill pressure. Higher $p_0$ correspond to a larger neutral population and, typically, greater collisionality, which might be expected to lead to stronger plasma quenching and thus a higher plasma resistivity. If the region being heated is smaller, however, it is possible for Ohmic heating to keep the region highly ionized despite the increased interaction with neutrals. In addition, while $n_0$ is higher, the total number of neutrals in the region being heated will depend on the product of $n_0$ and the volume of this region. Moreover, Figure 3.11(h) shows that $w_{cs}$ is largest at the end of the ionization phase and then decreases during the formation phase. This suggests that the skin layer may, as it shifts upstream during the formation phase, become somewhat insulated from the downstream neutral background by the larger region of plasma formed during the ionization phase.

Figure 3.11(i) shows that Ohmic heating in much of the first three phases has a weak inverse relation with pressure. This is consistent with our interpretation of higher pressures resulting in a smaller region of plasma being heated to higher temperatures. The associated reduction in $R_{sd}$ causes $P_{oh_{sd}}$ to be smaller despite the increase in $I_p$ with $p_0$.

Increasing $p_0$ does not appear to significantly alter the timing of the ionization and formation phases. The ionization phase is observed to be slightly extended and the formation phase slightly shortened, but these shifts are modest. The timing of the acceleration phase, however, is affected, with higher pressure delaying the onset of downstream motion of $z_{cs}$. We propose that this is because the stronger upstream localization effect leads to a larger electron pressure gradient which, in turn, creates a greater reduction in $E_z$ near the upstream edge. Downstream motion of $z_{cs}$ is then delayed until the gradient is relaxed and $E_z$ rises.

This delay also causes a rightward shift in the curves of $P_{em}$, as seen in Figure 3.11(j).

The surface current density and skin depth are directly related to the plasma magnetic field via equation (3.7). A stronger $B_{r_p}$ is equivalent to an increase in the decay of $B_r$ as it propagates through the sheet. As such, a higher $J_0$ and lower $\delta_{sd}$ indicate a sheet that is less transparent to the driving field produced by the drive coil. This is in agreement with Figures 3.11(j,k), which show that $P_{em}$ and $F_{em}$ increase with pressure, and suggests that the sheet becomes less permeable to the accelerating magnetic field as pressure is increased.

Based on the data in Figure 3.11, we conclude that the effects of higher $p_0$ (or equivalently $n_0$) on current sheet formation in our IPPT are as follows:

1. Formation of the initial PI plasma closer to the coil face.
2. Greater inductive coupling across all phases.
3. Enhanced localization of plasma current and Ohmic heating into a narrower region of plasma near the upstream edge of the current sheet.
4. Improved current sheet impermeability to the accelerating electromagnetic fields.

Given the importance of PI to point (1) which, in turn, affects all subsequent items, it is clear that PI can play a significant role in the evolution of the current sheet. We explore these effects in the following section.

### *3.6.2 Effects of Varying PI*

Figure 3.12 presents the effects of varying $V_{pi,0}$ on the evolution of the current sheet properties and derived quantities. From Figure 3.12(a), higher $V_{pi,0}$ is found to affect both the magnitude and timing of $I_c$ and $I_p$. Both $I_c$ and $I_p$ increase with $V_{pi,0}$. The increase is more pronounced for $I_p$, with the peak $I_p$ for $V_{pi,0} = 1.5\,\text{kV}$ being roughly double that of $V_{pi,0} = 0.5\,\text{kV}$. A clear increase in the rise rates of $I_c$ and $I_p$ is also observed, with the resulting leftward shift in the waveforms again being more apparent for $I_p$. Peak $I_p$ is found to occur approximately 200 ns earlier for $V_{pi,0} = 1.5\,\mathrm{kV}$ compared to $V_{pi,0} = 0.5\,\mathrm{kV}$. This shift suggests that the timing of the current sheet formation may be influenced by $V_{pi,0}$.

Figures 3.12(b-h) show that the effect of $V_{pi,0}$ on the initial values of the plotted variables is fairly modest. This seems somewhat counterintuitive, since we would expect varying $V_{pi,0}$ to strongly affect the parameter values at early times. While it is possible that the effects of this change occur mostly at $t \lesssim 200\,\mathrm{ns}$, where we do not have reliable data for most quantities, we would anticipate these effects would still propagate to later time, which we do not see strong evidence of.

Instead, we hypothesize that the relatively weak correlation between $V_{pi,0}$ and the initial values is related to the manner in which the second-stage PI was operated. When the PI capacitor bank was discharged, it was allowed to ring through five full cycles before the main discharge was initiated. The number of cycles was chosen to both ensure spatial uniformity of the PI plasma and allow for a PI plasma to be reliably generated at all conditions tested. By the later cycles, however, the PI capacitor bank was mostly drained and, accordingly, very little energy was being deposited into the PI plasma. We postulate that this allowed for significant quenching and diffusion of the PI plasma in the later cycles, which resulted in PI plasmas which were both relatively low ionization fraction and more similar than the differences in $V_{pi,0}$ would indicate.

Figures 3.12(c, d) show that $\delta_{sd}$ and $R_{sd}$ rise faster during the ionization phase as $V_{pi,0}$ is increased. The faster rise in $R_{sd}$ appears to be driven by a similar rise in $\delta_{sd}$, which we postulate is caused by a broader region of gas being ionized and quenched. This hypothesis is supported by the more rapid decline in $k$, further downstream migration of $z_{\mathrm{null}}$, and more substantial broadening of $w_{cs}$ during the ionization phase at higher $V_{pi,0}$. We note that Little et al.[31] and McCulloh et al.[71] reported a similar increase in early-time quenching as the initial gas ionization fraction was increased in their simulations.

The combination of higher $I_p$ and faster rise in $R_{sd}$ leads to one of the most important impacts of increased PI. Figure 3.12(i) shows a dramatic increase in the Ohmic heating during the ionization phase. Peak $P_{oh_{sd}}$ during this phase roughly doubles between the lowest and

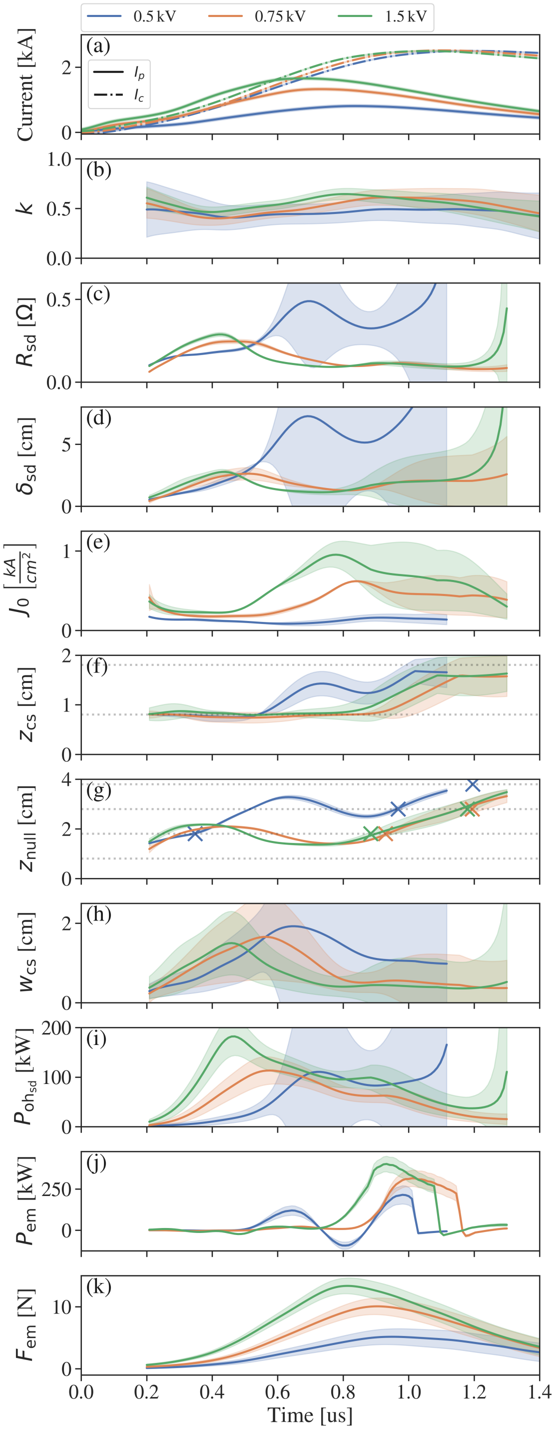

**Figure 3.12:** Effects of varying $V_{pi,0}$ on the temporal evolution of (a) $I_c$ and $I_p$, (b) $k$, (c) $R_{sd}$, (d) $\delta_{sd}$, (e) $J_0$, (f) $z_{cs}$, (g) $z_{null}$, (h) $w_{cs}$, (i) $P_{oh_{sd}}$, (j) $P_{em}$, and (k) $F_{em}$. Here, $V_{mb,0} = 1.5\,\text{kV}$ and $p_0 = 2.5\,\text{mTorr}$ (0.33 Pa, argon).

highest $V_{pi,0}$ cases and, moreover, occurs $\approx 300\,\mathrm{ns}$ earlier in time. The greatly increased Ohmic heating during the ionization phase leads to an earlier and more distinctive transition to the formation phase. Figure 3.12(b) shows that the characteristic change in the slope of $k$ between the two phases is found to be sharper and occur earlier in time. Similarly, from Figures 3.12(c-e) we find the local maxima in $\delta_{sd}$ and $R_{sd}$, and the transition of $J_0$ from relatively flat to rising, also occur earlier and are more pronounced.

During the formation phase, $k$ is found to rise at a greater rate with increasing $V_{pi,0}$, particularly when comparing the two higher cases to the lowest. Both the magnitude and rate of decrease in $\delta_{sd}$ and $R_{sd}$ are seen to increase with $V_{pi,0}$. Similarly, the rate of increase in $J_0$ is increased and a higher maximum $J_0$ is achieved. Together, these trends suggest that higher $V_{pi,0}$ lead to more rapid localization of plasma current and heating near the upstream edge of the sheet. This conjecture is supported by the quicker upstream motion in $z_{\mathrm{null}}$ and sharper initial narrowing in $w_{cs}$.

Like the ionization phase, the duration of the formation phase is also shortened at higher $V_{pi,0}$. We attribute this reduction to the increased Ohmic heating observed at the beginning of this phase. The higher heating causes the faster reduction in $\delta_{sd}$ and $R_{sd}$, which, in turn, drives the more rapid localization of the heating. This forms a feedback loop in which the already elevated heating is concentrated in a shrinking region of plasma. This effect results in a sharper decline in $P_{oh_{sd}}$ at the start of the formation phase, since the resistance drops quickly in the skin layer where heating is being concentrated.

The hastening of the upstream localization process leads to the sheet becoming impermeable to the accelerating magnetic fields earlier and, accordingly, a faster and more defined transition to the acceleration phase. The earlier onset of the acceleration phase at higher $V_{pi,0}$ is seen from Figures 3.12(f,g), where $z_{cs}$ and $z_{\mathrm{null}}$ are found to begin cohesive downstream motion earlier in time while $w_{cs}$ remains relatively constant. This is consistent with Figure 3.12(k) which shows $F_{em}$ rises faster and achieves a greater maximum at larger $V_{pi,0}$. A similar trend is also observed for $P_{em}$ (Figure 3.12(j)) for the 0.75 kV and 1.5 kV cases.

Downstream motion of $z_{cs}$ is observed to occur earliest in the $V_{pi,0} = 0.5\,\mathrm{kV}$ case, in apparent contrast with the trends at higher $V_{pi,0}$. We find from Figure 3.12(g), however, that this motion is not in concert with that of $z_{\text{null}}$. This is also supported by Figure 3.12(h), which indicates that $w_{cs}$ is still changing during the initial downstream motion in $z_{cs}$. This implies that, while the plasma undergoes some form of downstream motion, it is not of the cohesive type that appears to correspond with the acceleration of a current sheet. For the 0.5 kV case, this cohesive motion in both $z_{cs}$ and $z_{\text{null}}$, and the associated flattening of $w_{cs}$, does not occur until $\gtrsim 0.9\,\mu\text{s}$. This is, within uncertainty, no earlier than in the 0.75 kV case.

Unlike the previous two phases, the duration of the acceleration phase is found to grow with $V_{pi,0}$. This may be seen from Figures 3.12(b-e), which show an extended period of decline in $k$, low $\delta_{sd}$ and $R_{sd}$, and relatively high $J_0$. This is also supported by Figures 3.12(j,k), which show the region of significant $P_{em}$ and $F_{em}$ broadens as $V_{pi,0}$ increases. We interpret the longer acceleration phase as indicative of a more well-defined current sheet that demonstrates longer-lived magnetic impermeability. This impermeability is related to the value of $k$ at a given current sheet location, which will affect the $F_{em}$ produced as shown by equation (3.18). In general, the longer the sheet remains magnetically impermeable, the greater the time integrated $F_{em}$ and the larger the thrust produced by the IPPT. A more detailed discussion of the effects of the magnetic permeability on the motion of the current sheet may be found in Little et al.[31].

Little et al. found that increasing the initial gas ionization fraction ($\chi_0$) led to much stronger quenching of the sheet as it translated due to increased interaction with background neutrals [31]. Figures 3.12(c,d), however, indicate that higher $V_{pi,0}$ do not cause a concomitant increase in the cooling of the sheet during the acceleration phase. We note that, while $V_{pi,0}$ is expected to impact $\chi_0$, the two are not equivalent and may not scale proportionally. We showed previously that increasing $V_{pi,0}$ appears to result in a wider initial plasma region. This suggests that increasing $V_{pi,0}$ may have ionized a broader region of gas to similar $\chi_0$ rather than increasing $\chi_0$ within a fixed region as was simulated by Little et al. In addition, we previously hypothesized that $\chi_0$ was both similar and relatively small in all $V_{pi,0}$ cases due to the method of operation of the second-stage PI discussed earlier in this section.

The lack of quenching during the acceleration phase suggests that the electrons in the sheet do not experience significant inelastic collisions with background neutrals as the sheet translates. To estimate the interaction between sheet electrons and background neutrals as the sheet translates, we examine the ionization transparency proposed by Little et al.[31]

$$\theta_{m,ion} = \exp\left(-n_{cs} w_{cs} K_{ion}/v_{cs}\right) \ , \tag{3.20}$$

where $n_{cs}$ is the plasma density in the current sheet, $v_{cs}$ is the current sheet velocity, and $K_{ion}$ is the ionization reaction rate. From Figure 3.12 we find $w_{cs} \approx 0.5\,\mathrm{cm}$ and $v_{cs} \approx 30\,\mathrm{km/s}$ during the acceleration phase. We assume based on the simulated results of McCulloh et al.[71] that the density of the sheet is at least on the order of the ambient gas, i.e., $n_{cs} \gtrsim 1 \times 10^{20}\,\mathrm{m}^{-3}$.

Evaluation of $K_{ion}$ requires an estimate of the electron temperature in the sheet, $T_e$. Using the plasma resistivity and electron-ion and electron-neutral collision frequency equations from Little et al., when $n_{cs} \gtrsim n_0$ it may be approximated

$$T_e \approx \left(\frac{1.45 \times 10^{-3}}{\rho_{sd}}\right)^{2/3} \ , \tag{3.21}$$

where we use the resistivity in the skin depth layer instead of the global plasma resistivity, and the resulting $T_e$ is in units of eV. Equation (3.21) suggests that $T_e \approx 2.5\,\mathrm{eV}$ during the acceleration phase, which appears reasonable based on reported simulated and experimental results[16, 71, 29]. With this $T_e$, and using an empirical expression for $K_{ion}$[73], we find $\theta_{ion} \approx 1$. For comparison, estimations of $T_e$ at $5\,\mathrm{eV}$ and $10\,\mathrm{eV}$ produce $\theta_{ion}$ of 0.97 and 0.77, respectively. These high $\theta_{ion}$ are consistent with our observation of only modest quenching during the acceleration phase and support our claim that the electrons in our current sheets are not significantly ionizing the background neutrals as the sheet translates.

While the evolution of the variables in Figure 3.12 appear similar for $V_{pi,0}$ of 0.75 kV and 1.5 kV, they are notably different for the 0.5 kV case. In this lowest $V_{pi,0}$ case, transitions between the ionization, formation, and acceleration phases are either not observed or poorly defined. In addition, upstream localization of heating and current appears to occur only slightly. Together, these observations suggest that the current sheet formed in this case is very weak. When $V_{pi,0}$ was lowered much below 0.5 kV, no significant $I_p$ was observed to form during the first half-cycle of $I_c$. This suggests a threshold value of $V_{pi,0}$ needed to form a current sheet in our IPPT.

Some evidence of asymptotic behavior with increasing $V_{pi,0}$ is observed from Figure 3.12. While significant changes in the evolution of the variables occur between all three cases shown, they are, as a proportion of the change in $V_{pi,0}$, less substantial between the 0.75 kV and 1.5 kV cases than between the two lowest $V_{pi,0}$ cases. An increase in $V_{pi,0}$ by 50% is found to roughly double the maximum $I_p$ and $F_{em}$ and shift the peak in $P_{oh_{sd}}$ leftward by approximately 200 ns. In comparison, a doubling of $V_{pi,0}$ in the two higher cases produces only about a 1.3 increase in both maximum $I_p$ and $F_{em}$ while the peak in Ohmic heating occurs some $\approx$ 100 ns earlier. While additional data and further investigation are needed, this suggests that there may be a point of diminishing returns when increasing $V_{pi,0}$ or potentially the degree of PI in general.

Based on the data in Figure 3.12, we conclude the effects of higher $V_{pi,0}$ on current sheet formation in our IPPT are as follows:

1. Ionization of a broader region of gas.
2. Ohmic heating in the ionization and formation phases is markedly increased, which also shortens the duration of these phases.
3. Enhanced and more rapid upstream localization.
4. Current sheet impermeability is improved and sheet acceleration appears longer lasting.

## 3.7 Conclusions

We have presented methods for examining the evolution of the current sheet produced by a planar IPPT. Applying the presented methods to experimental data obtained from a compact, low discharge energy IPPT, we were able to report, for the first time in the literature, time-dependent measurements of the inductive coupling and plasma resistance in the skin depth. These two quantities were then used to determine time-histories of the power going into Ohmic heating in and electromagnetic acceleration of the current sheet, providing powerful insight into its evolution.

We found that current sheet evolution in our IPPT could be described by three phases: ionization, formation, and acceleration. Our results indicated that Ohmic heating was essential in overcoming neutral quenching during the formation of the current sheet, which agreed with simulation results reported by Little et al.[31]. In addition, evidence of localization of the plasma current and Ohmic heating towards the upstream edge of the current sheet was found, suggesting the importance of the interplay between Ohmic heating and the skin depth of the plasma to the formation of the current sheet.

We used the presented methods along with experimental measurements to examine the influence of varying neutral fill density (or equivalently backfill pressure) and initial PI bank voltage on the evolution of the sheet. Higher fill pressures were found cause the current sheet to form closer to the coil face. While fill pressure has been previously shown to effect the formation location of the sheet, we have additionally shown that it results in higher coupling during all phases and, moreover, that this elevated coupling resulted in stronger upstream localization of the current and Ohmic heating. This, in turn, led to more well-defined current sheets that were less permeable to the driving magnetic fields.

While PI has long been known to impact current sheet formation in IPPTs, the exact mechanisms by which this was accomplished have been less studied. We found that larger PI bank voltages ionized a broader region of gas while the second-stage PI was active, which led to higher skin depths and skin depth resistances in the ionization phase. This higher resistance, combined with an increase in the plasma current, drove substantially higher Ohmic heating of the plasma during the ionization and formation phases. The duration of these phases was shortened as a result and the transition between them sharpened due to stronger and more rapid upstream localization of the plasma current and Ohmic heating.

The impact of varying the PI bank voltage appeared greatest at lower values, with diminishing returns observed as $V_{pi,0}$ continued to increase. Significant plasma current was not observed during the first half-cycle of $I_c$ when $V_{pi,0}$ was much below $0.5\,\mathrm{kV}$, providing evidence of a threshold $V_{pi,0}$ below which a current sheet could not be formed. This may suggest that below this threshold value the rate of collisional ionization of the gas is too slow for strong inductive coupling and significant plasma heating to occur during the first half-cycle. This adds to previous experimental evidence reported by Polzin[16] that suggests sufficient PI is essential to the formation of a current sheet in planar IPPTs with low per-pulse discharge energies.

# Chapter 4

# CURRENT SHEET SCALING IN A PLANAR IPPT

Having gained significant insight into how the current sheet in a planar IPPT evolves over time, we now attempt to determine the fundamental physical processes governing current sheet formation and how they relate to key thruster operational and design parameters. We make use of the evolution data from the previous chapter and analyze it in new ways to arrive at quantitative metrics for the strength of the current sheet. By observing how these metrics change with our control parameters, we are able to develop a dimensionless parameter that describes how the strength of the current sheet scales as a result of the fundamental driving physics. By correlating this scaling parameter with our control parameters, we are able to propose a link between the thruster operating and design parameters and the strength of the current sheet formed by the device.[3]

## *4.1 Motivation and Background*

Inductive pulsed plasma thrusters (IPPTs) are a type of electric propulsion (EP) device that accelerates a plasma via inductive means to produce thrust[3, 8]. This is typically accomplished by driving large ($\gtrsim$ kA), short-duration ($\lesssim 10\,\mathrm{us}$) pulses of current through an inductive coil, which, in turn, induce opposing currents in nearby plasma[64]. A number of parameters related to the operational scaling of IPPTs have been reported in the literature. Lovberg et al.[74] showed that the ratio of the circuit stray inductance to the acceleration coil inductance must be much less than one for efficient inductive acceleration. Polzin[16] considered a dynamic impedance parameter based on that used in analysis of pulsed plasma

---

[3] This chapter contains results from Curtis L Promislow and Justin M Little. Current sheet evolution in a planar inductive pulsed plasma thruster. Journal of Physics D: Applied Physics, 57(20):205205, 2024.[60]

thrusters (PPTs) and reported modeling work that demonstrated that there existed an optimum range for this parameter for maximum thruster efficiency. Polzin and Choueiri [28] and Martin and Eskridge[46] examined the damping ratios of the $RLC$ circuits formed by the drive and plasma circuits. Their modeling results found that the average of these two ratios should be much less than one for efficient IPPT operation, i.e., both $RLC$ circuits should be underdamped.

These parameters share a commonality in that they are all based on the dimensionless parameters that appear when considering the transient acceleration of a plasma in a generic parallel plate accelerator[1]. The systems of equations which give rise to these parameters are based on simplified 1D models which typically treat the plasma (or current sheet) as a slug or snowplow and largely overlook its formation. Much of the existing literature has also focused on the scaling of thruster performance, with relatively little attention paid to the scaling of the fundamental thruster physics. Polzin[23] provided an argument based on first-principles that suggested a minimum current rise rate was needed to form a current sheet. He further posited that the required value of the current rise rate would decrease in cases where pre-ionization (PI) of the neutral propellant was employed. The derivation of this criteria was largely phenomenological, however, and the ranges given were relatively large.

Little et al.[31] investigated current sheet formation in IPPTs through a 1D model that considered the effects of ionization and the electron energy balance under non-equilibrium conditions, neutral gas entrainment, and non-ideal electromagnetic coupling. In this work, Little et al. derived a dimensionless scaling parameter that represented the ratio of Ohmic heating of the electrons to inelastic ionization losses. This “formation parameter” was used to determine the conditions under which a magnetically impermeable current sheet would form, from which the importance of Ohmic heating early in the formation process was discovered. While this parameter was found to accurately describe the scaling of the mass utilization efficiency of the model results, its derivation relied on a number of simplifying assumptions and it has not yet been verified against experimental data.

Recent work by Promislow and Little[60] has demonstrated the ability to measure the time-varying mutual inductance and plasma resistance associated with the current sheet, providing substantial insight into its evolution. Using the methods in that work to analyze data obtained from a compact planar IPPT, we examine the scaling of the strength of the current sheets formed by this device under a range of operational conditions. The IPPT and diagnostics used to collect the data are described in section 4.2, as are the methods of data analysis. General application of the methods is explored in sections III4.3.1 and III4.3.2, and the scaling law obtained from their application is presented in section III4.3.3.

## *4.2 Approach*

The experimental setup and methods used to perform the measurements in this work are largely identical to those described in our earlier work, i.e., Ref. [60]. We provide a short summary here but direct the reader to the cited work for a more detailed description.

### *4.2.1 Experimental Setup*

Data on current sheet formation were taken using a compact, low discharge energy research prototype IPPT. Figure 4.1(a) depicts the current sheet formed by operation of the IPPT in an idealized case. Current flowing through the drive coil, $I_c$, generates a plasma and induces an azimuthal current density, $J_\theta$, in the plasma. Integration of $J_\theta$ over the current sheet volume yields the total plasma current, $I_p$. When $I_p$ accumulates in a narrow layer of plasma with width $w_{cs}$, a current sheet is formed. The location of the leading edge of the current sheet relative to the coil mid-plane is labeled $z_{cs}$. The total magnetic field, $B$, is a superposition of the fields produced by the currents flowing in the drive coil and plasma. In the region of the plasma, $B \approx B_r$, i.e., the magnetic field is assumed to be primarily radial. Idealized axial distributions of $J_\theta$ and the radial component of the total magnetic field, $B_r$, are depicted in Figure 4.1(a).

The prototype IPPT had an inner and outer drive coil radius of $r_a = 1.9\,\text{cm}$ and $r_b = 7.2\,\text{cm}$, respectively. The drive coil itself was formed from eight 1.5 turn Archimedes

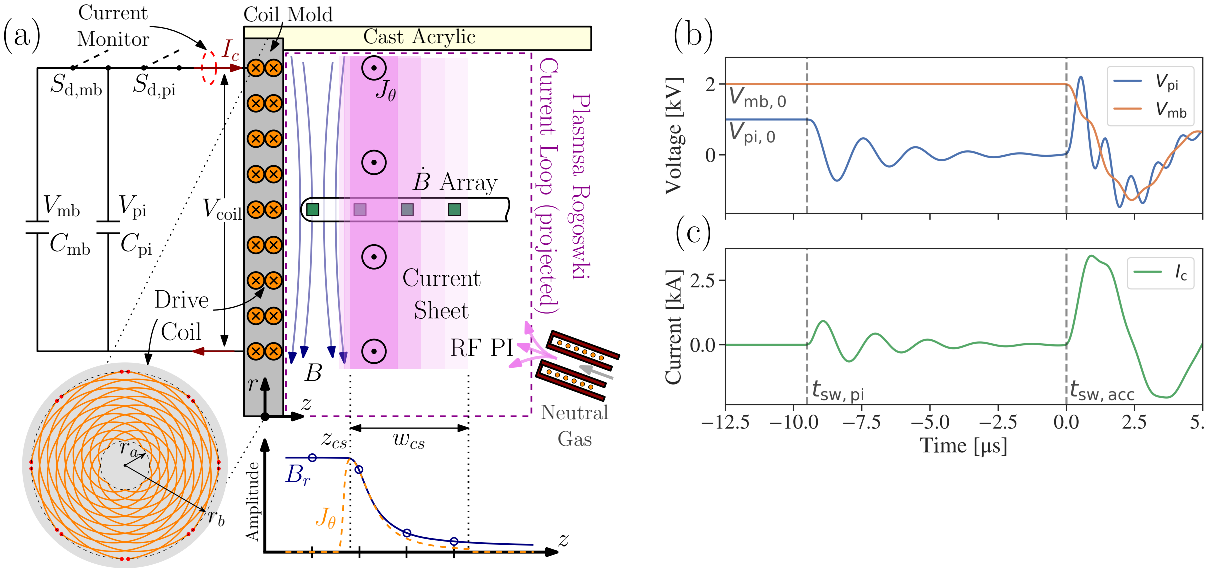

**Figure 4.1:** Diagram of compact, low discharge energy IPPT used for data collection from (a) side and front-on views and idealized (b) capacitor voltages and (c) discharge circuit current when a plasma is present in front of the drive coil. Reproduced from Promislow and Little[60].

spiral inductors connected in parallel and wound in a two-layer fashion to reduce stray inductance[3]. The drive coil was measured to have an inductance of 375 nH at 300 kHz using an $LCR$ meter. The stray inductance and decoupling distance of the drive coil were found to be 40 nH and 3.13 cm, respectively, by using the “dummy” load method[46, 64].

The IPPT was installed on a small cylindrical vacuum system (25.4 cm inner diameter, 60.96 cm long). A turbomolecular pump backed by a rotary vane roughing pump produced chamber base pressures as low as $5 \times 10^{-6}$ Torr ($6.7 \times 10^{-4}$ Pa). During experiments, gas was delivered through the RF PI, with the flow of gas controlled via either a needle valve or an Alicat mass flow controller (model MC-10SLPM-D/5M). Pressure in the chamber was measured with a $1 \times 10^{-4}$ Torr to 0.1 Torr (0.013 Pa to 13.3 Pa) range capacitance manometer (MKS 626D).

Figure 4.1(a) shows the discharge circuit of the IPPT, which consisted of two capacitor banks, two switches, and the drive coil. A “main” capacitor bank, $C_{mb}$, stores the energy for forming and accelerates the current sheet. $C_{mb}$ (1.5 µF) was connected to the drive coil by an insulated gate bipolar transistor (IGBT) switch $S_{mb}$ (ABB 5SNA0750G650300). A second, smaller capacitance bank, $C_{pi}$ (330 nF), was discharged via IGBT switch $S_{pi}$ (ABB 5SNA1200E330100) and was part of the PI system. Nominal charging voltages for the capacitor banks were no more than 2 kV, giving a maximum total per-pulse discharge energy of 4 J.

The current rise rate in our IPPT was found to be insufficient to break down the neutral gas unassisted. Instead, a two-stage PI system was used to initiate gas breakdown and supply an initial plasma for the main discharge to couple energy into. The first stage was an RF PI, which consists of a 1.27 cm diameter solenoidal coil driven by a 13.56 MHz RF generator at 100 W. In the second stage, $C_{pi}$ was discharged through the drive coil. This was intended to ionize more of the neutral gas and distribute it more evenly over the coil face than using the RF PI alone.

Typical operation of the IPPT discharge circuit is shown in Figure 4.1(b,c). Prior to operation, the static fill pressure in the chamber, $p_0$, is set and allowed to reach a steady value. Next, $C_{mb}$ and $C_{pi}$ are charged to their target voltages, $V_{mb,0}$ and $V_{pi,0}$, respectively. Once charged, the RF PI is turned on, initiating breakdown of the neutral gas. At time $t_{sw,pi}$, switch $S_{pi}$ is activated, marking the start of the second-stage PI. The RF PI is also deactivated at this time. After five cycles of the second-stage PI discharge, typically $\sim 10\,\mu s$, switch $S_{mb}$ is closed, connecting $C_{mb}$ to the drive coil and initiating the main discharge. We take the time of $S_{mb}$ closing ($t_{sw,acc}$ in Figure 4.1(c)) as $t = 0$ for plotting purposes.

A suite of diagnostics was used to collect data from the prototype IPPT setup. The discharge circuit current, $I_c$, was measured by a current transformer (Ion Physics CM-10-M) with 0.1 V/A sensitivity and 12 ns rise time. $I_c$ was measured at the location where the drive coil connected to the rest of the discharge circuit (see Figure 4.1(a)). We used a rectangular (plasma) Rogowski coil to measure $I_p$. This loop, depicted by the dashed region in Figure 4.1(a), extended axially from the coil face to 7 cm downstream (over twice the drive coil decoupling distance) and radially from 1.5 cm to 7.5 cm. This current sensing loop was sufficient to encompass the entirety of the region in which plasma is observed. The voltages across the main capacitor bank ($V_{mb}$), 2nd-stage PI capacitor bank ($V_{pi}$) and drive coil, ($V_{\text{coil}}$), were measured using differential probes with a 100 MHz bandwidth (Pintek PT-8020). The high common mode rejection ratio (CMRR) of these probes in combination with digital filters resulted in excellent high frequency noise immunity.

Figure 4.1(a) depicts the calibrated linear $\dot{B}$ probe array used to measure the rate of change of the radial component of the total magnetic field, $B_r$, at the mean radius of the drive coil. This array consisted of four 5.6 µH chip inductors spaced $\Delta z = 1$ cm apart. The first probe is located 0.5 cm from the drive coil face and 0.81 cm from the coil mid-plane. Integration of the $\dot{B}_r$ signals to obtain $B_r$ was achieved numerically, with a detrending algorithm being used to reduce error associated with drift in the integration.

### *4.2.2 Methods*

We now summarize the methods for determining the evolution of the inductive coupling between the drive coil and current sheet and the characteristic plasma resistance inside the skin depth from measurements taken by the diagnostics described in section II4.2.1. The former is obtained from the circuit measurements while the latter is determined from analysis of data from the linear $\dot{B}$ probe array. A full discussion of these methods can be found in Ref. [60].

#### *Inductive Coupling*

We model the electrical interaction between the IPPT discharge circuit and the translating current sheet using a well known lumped-element circuit model, shown in Figure 4.2, that couples the discharge circuit to a plasma circuit via a transformer model[27, 15]. Defining $V_{coil}$ as the voltage across the drive coil (see Figure 4.1(a)), we may express the inductive coupling coefficient between the drive coil and current sheet as

$$k = \frac{1}{I_p\sqrt{L_c L_p}}\left[L_c\left(I_c - I_{c,0}\right) - \int_{t_0}^{t} V_{\text{coil}}\,d\tau\right]\,, \tag{4.1}$$

where $I_c$ and $I_p$ are the currents in the discharge and plasma circuits, $k$ is the inductive coupling coefficient, and $L_c$ and $L_p$ are the self-inductances of the the drive coil and plasma, respectively. $I_{c,0}$ is the discharge circuit current at $t = t_0$ and $\tau$ is a dummy time variable for integration. In this work, we take $t_0 = t_{sw,pi}$ (see Figure 4.1(b,c)). Equation (4.1) shows that $k$ may be directly calculated if $L_c$ and $L_p$ are known and $V_{coil}$, $I_c$, and $I_p$ are measured.

To obtain the plasma inductance, we follow Dailey and Lovberg [18] and approximate the shape of the current sheet as a flat annulus. This allows us to estimate its inductance according to

$$L_p = \mu_0\frac{r_a + r_b}{2}\left[\ln\left(\frac{r_b + r_a}{r_b - r_a}\right) + 0.9\right]\,, \tag{4.2}$$

where $r_a$ and $r_b$ are the inner and outer radii of the annulus, respectively, and $\mu_0$ is the permeability of free space. We assume here that $r_b$ and $r_a$ are constant and, moreover, the same as those of the drive coil. This latter assumption asserts that the current sheet forms over the entire surface of the drive coil. We note that, due to our assumptions, equation (4.2) yields a constant value for $L_p$.

*Plasma Resistivity*

The lumped-element circuit model shown in Figure 4.2 treats the plasma as a single resistor with resistance $R_p$. This bulk plasma resistance is closely related to the resistive, i.e., Ohmic, heating of the plasma, which Little et al. have shown is central to formation of the current sheet[31]. For conductors carrying time-varying currents, Ohmic heating primarily occurs within the skin depth[67]. As such, we believe that the resistance of the plasma inside the skin depth, $R_{sd}$, provides more insight into the evolution of the current sheet than the bulk plasma resistance described by $R_p$.

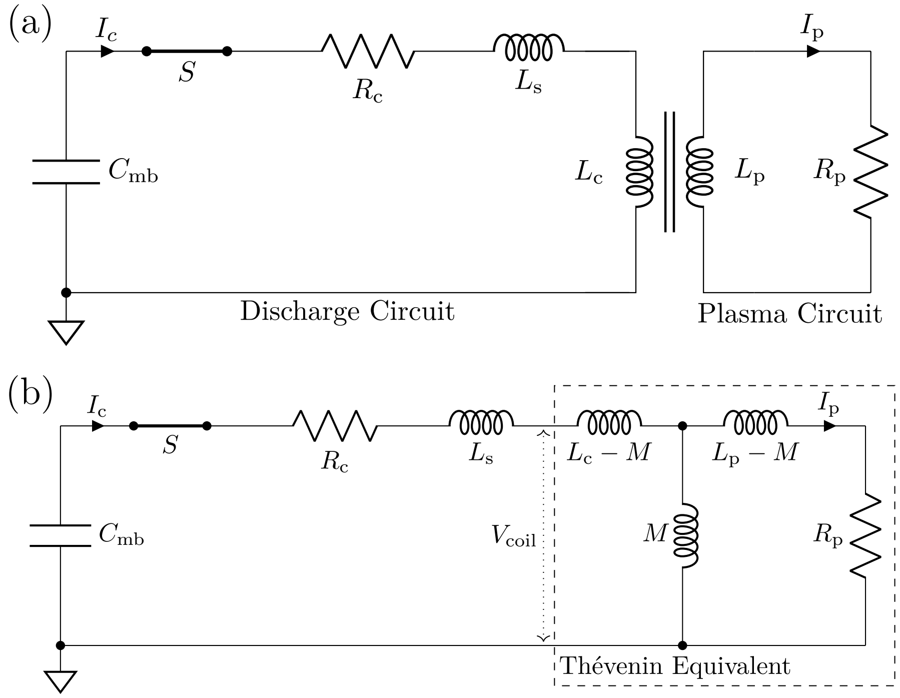

**Figure 4.2:** Lumped element circuit diagram of the IPPT discharge circuit transformer coupled to the plasma. The coupling can be modeled as a (a) transformer or its (b) Thévenin-equivalent circuit. Reproduced from Promislow and Little[60].

Information regarding the skin depth resistance can be obtained from data from our linear $\dot{B}$ probe array which describes how $B_r$ decays with axial distance. We first link $B_r$ to the current density in the sheet by evaluating the azimuthal component of Ampere's law at the mean radius of the drive coil, where we approximate $\partial B_z/\partial r \approx 0$ to find

$$\frac{dB_r}{dz} = \mu_0 J_\theta \, . \tag{4.3}$$

We now assume an exponential form for the azimuthal current density $J_\theta$ inside the current sheet

$$J_\theta(z) = \begin{cases} 0, & z < z_{cs} \\ J_0 \exp\left(-\dfrac{z - z_{cs}}{\delta_{fd}}\right), & z \geq z_{cs}\,, \end{cases} \tag{4.4}$$

where $J_0$ is the surface current density and $z$ and $z_{cs}$ are the axial distance of the measurement location and current sheet leading edge from the mid-plane of the drive coil, respectively. We note that since equation (4.4) considers only the axial variation of $J_\theta$, it implicitly assumes that the current sheet is radially uniform. This assumption is supported by data reported by Dailey and Lovberg[11], which showed that the axial distribution of the electric field was fairly uniform across in the radius of the coil face.

The leading $J_0$ in equation (4.4) is not a constant but rather $J_0(t)$ and is intended to capture the time dependency of the current distribution. The decay rate from this value is dictated by the flux penetration depth, $\delta_{fd}$, which is the transient analogue to the harmonic skin depth for a steady-state driving waveform, $\delta_{sd}$. While the magnitude of the driving field is rising, it can be shown[67]

$$\delta_{sd} \approx \frac{4}{3}\delta_{fd}\,. \tag{4.5}$$

The form of $J_\theta$ proposed in equation (4.4) is motivated by a combination of theory and experiment[67, 10]. An important limitation, however, is that it is unable to distinguish phase shifts in $J_\theta$ that occur as it propagates into the plasma from bulk downstream motion. As such, our assumed $J_\theta$ is only applicable before the phase shift in the current density becomes significant. Based on a combination of theory and experiment[67, 10], equation (4.4), and all subsequent equations which rely upon it, only apply until approximately the maximum in the driving magnetic field or, equivalently, the maximum in $I_c$.

Substituting equation (4.4) into equation (4.3) and integrating yields an axial profile of $B_r$. Due to superposition, we can subtract the component of the total $B_r$ due to the coil current, $B_{r_c}$, and find an expression for the field due to plasma currents only

$$B_{r_p} = \mu_0 J_0 \delta_{fd}\left[1 - \exp\left(-\frac{z - z_{cs}}{\delta_{fd}}\right)\right] + B_{r,0} - B_{r_c}. \tag{4.6}$$

Here, $B_{r,0}$ is the value of the total radial magnetic field at the upstream surface of the current sheet. In equation (4.6) $B_{r_c}$ is not a constant but rather itself a function of $z$. To extract this component from the measured total $B_r$, we produced a calibration curve that related $I_c$ and $B_{r_c}$ which, for cases where plasma was present, allowed $B_{r_c}$ to be determined from the measured $I_c$. By measuring $B_r$ at various $z$ locations and then subtracting the corresponding $B_{r_c}$, a measured profile for $B_{r_p}$ was generated to which equation (4.6) was fit. The fit parameters are $\delta_{fd}$, $J_0$, and $z_{cs}$. $B_{r,0}$ was taken to be the maximum $B_r$ measured by the array. After finding $\delta_{fd}$, and therefore $\delta_{sd}$, from the fit, we can determine the bulk resistivity in the current sheet using

$$\eta_{sd} = \frac{1}{2}\mu_0 \omega_{I_p} \delta_{sd}^2 \,, \tag{4.7}$$

where $\omega_{I_p}$ is the angular frequency of the bulk plasma current. This value was calculated at each time step via the Hilbert transform method [68].

## 4.3 Results and Analysis

We have performed extensive measurements of our IPPT when it is discharged into a static gas backfill as part of an effort to better understand the formation and evolution of the current sheet in IPPTs. In combination with new methods for data analysis, these measurements have allowed us to calculate the time-dependent inductive coupling coefficient and characteristic plasma resistance within the current sheet.

### 4.3.1 Circuit Measurements

The mutual inductance as a function of time was found from equation (4.1) by using experimentally measured waveforms for $I_c$, $I_p$, and $V_{\text{coil}}$. Figure 4.3 shows a typical set of measured waveforms for a vacuum (no plasma) and a representative plasma case. We note that the error bands in Figure 4.3 represent the uncertainty associated with both the estimated measurement error associated with the relevant diagnostic and the uncertainty due to variance between discharges.

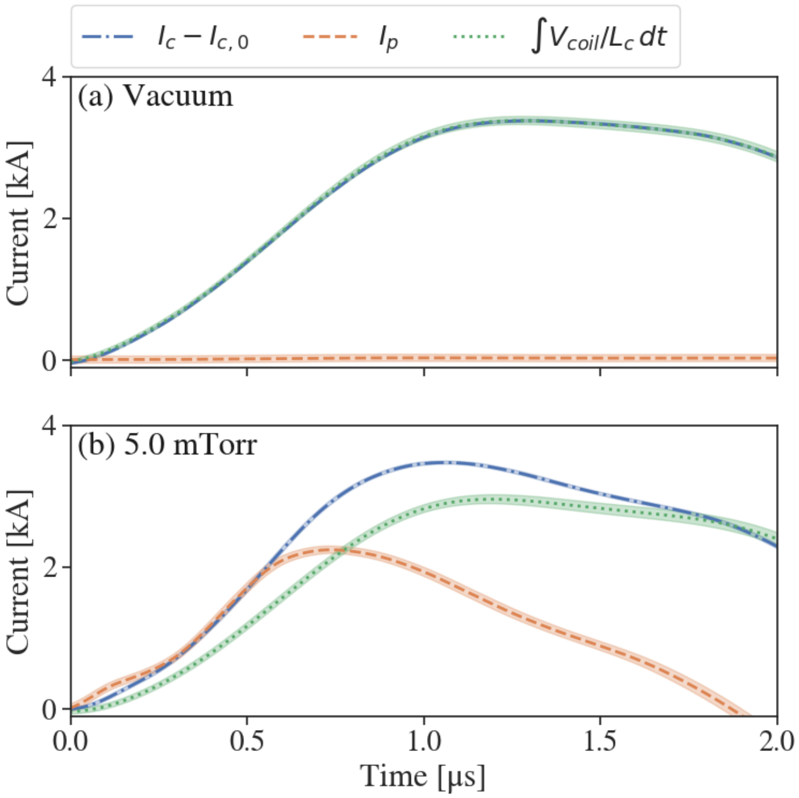

**Figure 4.3:** Comparison of experimentally measured waveforms of $I_c$, $I_p$, and integrated $V_{\mathrm{coil}}$ used to calculate the mutual inductance between a (a) vacuum and (b) a representative plasma case. For the plasma case, $p_0 = 5\,\mathrm{mTorr}$ (0.67 Pa, argon), $V_{pi,0} = 1\,\mathrm{kV}$, and $V_{mb,0} = 2\,\mathrm{kV}$.

In the absence of a coupled plasma load, the circuit should behave like a transformer with an open secondary. In this case, $I_c - I_{c,0}$ and $\int V_{\mathrm{coil}}/L_c\, dt$ should be equal, as seen in Figure 4.3(a). Figure 4.3(b) shows that all three terms, i.e., $I_p$, $I_c - I_{c,0}$, and $\int V_{\mathrm{coil}}/L_c\, dt$ are affected by the presence of plasma. While both $I_p$ and the difference between $I_c - I_{c,0}$ and $\int V_{\mathrm{coil}}/L_c\, dt$ appear to grow, the effect on the coupling will depend on their ratio. To avoid a singularity, equation (4.1) necessitates that the bracketed term goes to zero at the same time as $I_p$. Graphically, this means that the curves of $I_c - I_{c,0}$ and $\int V_{\mathrm{coil}}\, dt/L_c$ should intersect at zero-crossings of $I_p$. Figure 4.3(b) shows this occurs to within the measurement uncertainty.

### *4.3.2 $B_r(z)$ Curve Fits*

Figure 4.4 shows the total $B_r$ waveforms measured by each of the four probes in the array. From this total $B_r$, the components due to the coil and plasma currents were extracted using the calibration curve method described in section 4.2.2. The waveforms of these components are also shown in Figure 4.4.

The magnitude of the total field relative to the coil component can be used to estimate the position of the current sheet. When the sheet is downstream of a probe, its magnetic field will be in the same direction as that produced by the coil and the total field will be larger than the coil component alone. This effect is more pronounced the closer the probe is to the leading edge of the current sheet. As the sheet passes over the probe, the fields produced by plasma upstream and downstream of the probes will be in opposing directions. This can equivalently be thought of as a screening effect, wherein the upstream plasma blocks some of the field produced by the drive coil from reaching the probes. Due to this behavior, $B_r$ will become less than $B_{r_c}$.

By taking the value of $B_{r_p}$ at a given time for each of the four probes in the array, a curve for the axial variation of $B_{r_p}$ can be obtained, to which equation (4.6) can be fit. Figure 4.5 shows $B_{r_p}$ as a function of the axial coordinate, $z$, for nine time slices. We observe that the data generally follows an exponential decay, lending confidence to our use of equation (4.6). The dashed black line is the curve obtained by performing a nonlinear weighted least-squares fit of equation (4.6) to the data[60]; good agreement between the fitted curve and the data was generally achieved.

Examining Figure 4.5, we find that plasma appears to form between probes one and two sometime before the 0.32 µs mark. As time progresses, the absolute values of the measured fields increase while the slope of the fit increases. This suggests a region of plasma that is both expanding and where the plasma current is growing. At 0.65 µs, we see the $B_{r_p}(z)$ profile

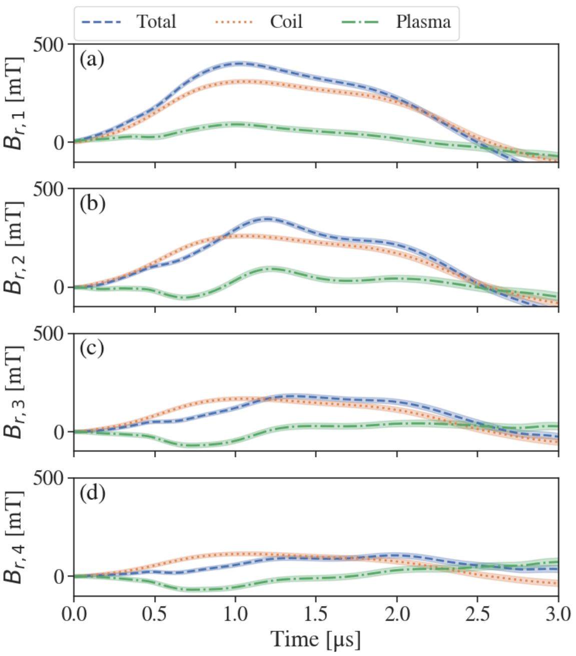

**Figure 4.4:** Measured $B_r$ from linear $\dot{B}$ probe array for nominal operating conditions and $p_0 = 5\,\mathrm{mTorr}$ (0.67 Pa, argon). Probes were stationed at axial distances of (a) 0.5 cm, (b) 1.5 cm, (c) 2.5 cm, and (d) 3.5 cm from the coil face.

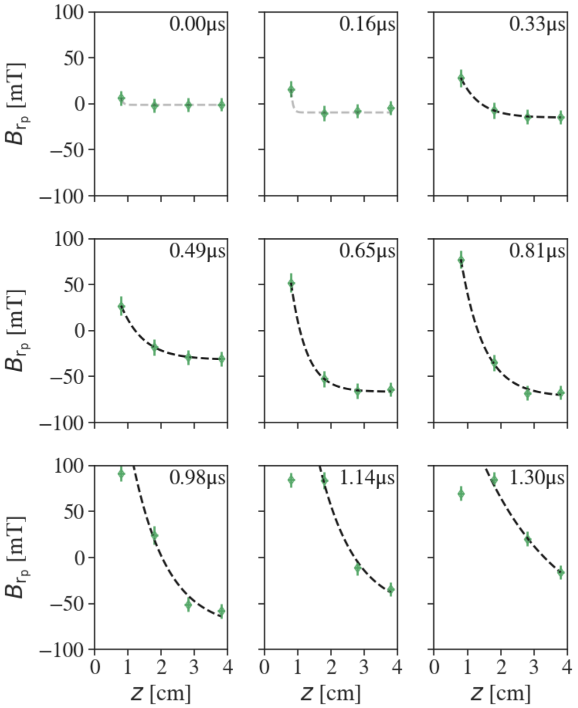

**Figure 4.5:** Fits produced by weighted non-linear least squares curve fitting of $B_{r_p}$ data measured by a linear $\dot{B}_r$ probe array for $p_0 = 5\,\mathrm{mTorr}$ (0.67 Pa, argon).

has steepened significantly between probes one and two. This points towards the broader plasma region narrowing into what may be a magnetically impermeable current sheet. At 0.98 µs, we see the first indication of significant sheet motion, with the fit no longer passing directly through probe one. By 1.14 µs, the $B_{r_p}$ measured at probe two increases above that measured at probe one, indicating the greater proximity of $z_{cs}$ to this probe. The sheet is also observed to broaden as it translates, with the slope of the fit decreasing between 0.65 µs and 1.30 µs.

We note that in a small number of cases, the $B_{r_p}$ axial profile steepens to the degree that it lies exclusively between probes one and two. The fitting procedure is considered unreliable at this point due to it attempting to fit a model with three unknowns to what is effectively two data points. In these cases, $J_0$ is not determined directly from the $B_{r_p}$ fits but rather by polynomial interpolation using the $J_0$ points determined by fits where at least three $B_{r_p}$ points were available. The uncertainty in these points is then the uncertainty in the fit rather than a direct measurement uncertainty.

### *4.3.3 Current Sheet Evolution and Scaling*

Figure 4.6 shows the evolution of several key current sheet parameters for a representative plasma case. For this case, $p_0 = 5\,\mathrm{mTorr}$, $V_{pi,0} = 1\,\mathrm{kV}$, $V_{mb} = 2\,\mathrm{kV}$, and the fill gas was argon. Three distinct phases are generally observed, which we have previously assigned as the ionization, formation, and acceleration phases[60]. The ionization phase corresponds to the ionization of a somewhat broad region of plasma is characterized by a relatively low current density and rising $\delta_{sd}$ and $\eta_{sd}$. $k$ can increase or decrease during this phase, depending on conditions such as $p_0$ and $V_{pi,0}$. During the formation phase, $J_0$ increases rapidly while $\delta_{sd}$, and correspondingly $\eta_{sd}$, decrease. We have interpreted these trends to be indicative of the formation of a magnetically impermeable current sheet, wherein current is being concentrated in a thin layer of plasma. The increase in $k$ during this phase suggests that the current is being localized towards the upstream edge of the sheet. We have previously postulated that the upstream localization of the current drives increasingly localized heating and is ultimately responsible for the formation of the current sheet.

Finally, assuming a magnetically impermeable current sheet was formed, the sheet is pushed downstream from the coil face during the acceleration phase. This is evidenced by the steady decline in $k$ during this phase and is also supported by the magnetic field probe measurements, which showed the leading edge of the current sheet translating downstream only in this phase[60]. The plasma in the sheet cools as it both encounters downstream neutrals and receives less energy from the drive coil, leading to a decrease in $J_0$ and increase

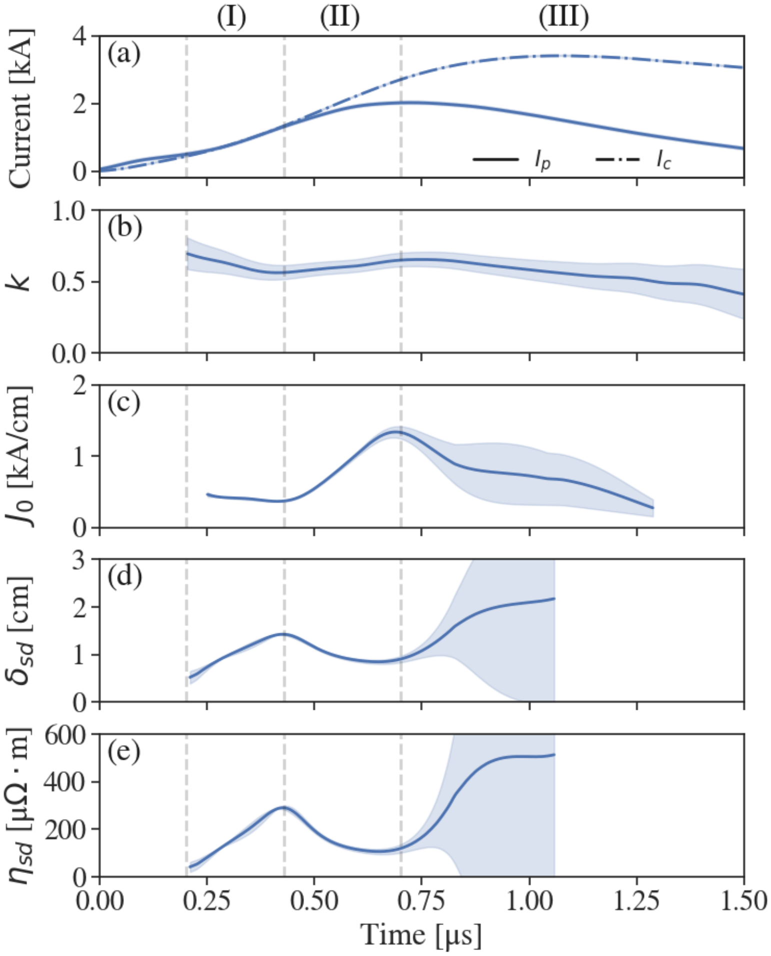

**Figure 4.6:** Time-histories of (a) $I_c$ and $I_p$, (b) $k$, (c) $J_0$, (d) $\delta_{sd}$, and (e) $\eta_{sd}$ from which the scaling parameters are calculated. Dashed vertical lines demarcate the approximate time ranges for the (I) ionization, (II) formation, and (III) acceleration phases.

in $\delta_{sd}$ and $\eta_{sd}$.

We propose two dimensionless parameters for characterizing the strength of the current sheet formed by our IPPT. The first is the maximum $k$ achieved at the end of the formation phase. This parameter serves as a metric for the inductive coupling between the drive coil and current sheet as the latter begins to accelerate downstream. The second is a non-dimensionalized current density, which we define as

$$\hat{J}_0 = \frac{J_{0,max}}{I_{c,max}/z_{dc}} \,. \tag{4.8}$$

Here, $J_{0,max}$ and $I_{c,max}$ are the maximum values of $J_0$ and $I_c$ measured during the first half-cycle of the total plasma current. $\hat{J}_0$ is intended to represent the effectiveness with which a current flowing in the drive circuit is able to produce a localized current in the plasma. Note that we have used $J_0$ instead of $I_p$ in our parameter, since we are more interested in the concentration of the plasma current rather than its total magnitude. In addition to being a metric of the strength of the current sheet, $\hat{J}_0$ is also related to the performance of the thruster, since $J_\theta$ appears in the $J_\theta B_r$ force in the momentum equation[64].

### *Dimensionless Scaling Parameter*

We now seek a dimensionless scaling parameter that encompasses the fundamental physics central to the formation of a current sheet in our device. In the simplest terms, a current sheet is formed when current is able to concentrate in a thin layer of plasma. As such, we propose that the process of current sheet formation can be modeled as a competition between effects that concentrate and those that diffuse current.

Both Lovberg and Dailey[18] and Polzin[29] considered a current sheet that was broadening due to resistive diffusion of the magnetic field. Equation (4.3) shows that the azimuthal current density is directly related to the gradient in the radial magnetic field. As the current sheet forms, the gradient in $B_r$ will be influenced by the properties of the plasma. Transport of a magnetic field into a conductor is governed by the the magnetic diffusion equation which states

$$\frac{\partial \vec{B}}{\partial t} = D_B \nabla^2 \vec{B} + \nabla \times \left( \vec{v} \times \vec{B} \right) \,, \tag{4.9}$$

where

$$D_B = \eta / \mu_0 \tag{4.10}$$

is the magnetic diffusivity and $\eta$ is the resistivity. The relative importance of the diffusive (1st) term compared to the convective (2nd) term is described by the magnetic Reynolds number

$$R_m = \frac{v_{cs} z_{dc}}{D_B}\,, \tag{4.11}$$

where $v_{cs}$ is the velocity of the current sheet and we have selected $z_{dc}$ as the characteristic plasma length scale. Data presented by Promislow and Little[60] indicated that the current sheet was relatively stationary and also fairly resistive during the ionization and formation phases. This suggests that $R_m \lesssim 1$ in our device, at least during formation. This would point towards diffusion being the dominant mechanism, reducing equation (4.9) to

$$\frac{\partial \vec{B}}{\partial t} \approx D_B \nabla^2 \vec{B}\,. \tag{4.12}$$

We note that this is the case of a transient magnetic field diffusing into a stationary conductor.

If we take the curl of equation (4.12) and substitute in equation (4.3), the result is a diffusion equation for the current density in the plasma

$$\frac{\partial \vec{J}}{\partial t} = D_B \nabla^2 \vec{J}. \tag{4.13}$$

Under our stated assumption that $\vec{J} = J_\theta \hat{\theta}$ and that $J_\theta$ is both radially and azimuthally uniform, equation (4.13) reduces to the 1D form

$$\frac{dJ_\theta}{dt} = D_B \frac{\partial^2 J_\theta}{\partial z^2}\,. \tag{4.14}$$

Equation (4.14) shows that the magnetic diffusivity is directly related to the current density rise rate, which has long been seen as a key metric for current sheet formation[23]. Moreover, it suggests that the relevant timescale governing the dissipation of the plasma current is the characteristic timescale for resistive diffusion of the magnetic field.

The magnetic diffusivity also affects the buildup of current density through its relationship with the skin effect. We have previously (see section 3.5) discussed the importance of this effect in driving the upstream localization of the current density that we have postulated is a hallmark of current sheet formation. The skin depth is the characteristic distance from the surface of a conductor over which the current density decays and may be written as

$$\delta_{sd} = \sqrt{\frac{2\eta}{\omega\mu}}\,, \tag{4.15}$$

where $\eta$ is the material resistivity, $\omega$ is the frequency of the current, and $\mu$ is the magnetic permeability of the conductor. Substituting equation (4.10) and assuming $\mu \approx \mu_0$, we find

$$\delta_{sd} = \sqrt{\frac{2D_B}{\omega}}\,. \tag{4.16}$$

Equation (4.16) shows that the magnetic diffusivity is directly related to the skin depth that, according to equation (4.4), controls the depth of the region in which current flows in the plasma. This relationship can be understood as the skin depth being the characteristic length that the magnetic field diffuses into the plasma over one period of oscillation. While we have obtained this result for the harmonic skin depth, $\delta_{sd}$, equation (4.5) shows that a similar result also holds for the case of a non-sinusoidal transient current via the flux penetration depth, $\delta_{fd}$.

As we have seen, magnetic diffusion is expected to be highly influential to both the spatial concentration of current and the rate at which it increases during current sheet formation. It is therefore of interest to estimate the characteristic timescale over which magnetic diffusion into the plasma occurs in our device. To find an expression for this timescale, we consider the characteristic depth to which a time-varying magnetic field penetrates into a planar conductor via diffusion

$$l_c = \sqrt{\frac{\tau_d \eta}{\mu}}\,, \tag{4.17}$$

where $l_c$ is a characteristic length scale for the conductor and $\tau_d$ is the characteristic diffusion time. Note that we have again assumed $\mu \approx \mu_0$, i.e., that the permeability of the conductor is roughly that of free space. By choosing the electromagnetic decoupling distance ($z_{dc}$) as our characteristic length scale, we can rearrange equation (4.17) to arrive at a characteristic timescale for the field to diffuse through the decoupling distance

$$\tau_d = \frac{\mu_0 z_{dc}^2}{\eta_{sd,max}}\,, \tag{4.18}$$

where $\eta_{sd,max}$ is the resistivity calculated from equation (4.7) for the maximum $\delta_{sd}$ measured during the ionization phase.

By inspection, we see that equation (4.18) represents the shortest timescale that the magnetic field could diffuse over the decoupling distance. It is also the characteristic timescale over which magnetic energy is dissipated over this distance. For effective current sheet formation, we require a sheet that is largely impermeable to the driving magnetic field. Accordingly, a large value of $\tau_d$ is desired such that the diffusion of the driving magnetic field is minimized. Equation (4.18) shows that this is accomplished by achieving a low plasma resistivity in the skin depth. This in turn suggests the need for vigorous heating of the plasma early on in the discharge, which is in agreement with the conclusions of Little et al.[31].

The theoretical results of Little et al.[31] suggested that ionization played a significant role in the evolution of the current density during formation of the sheet. While Equation (4.14) describes how an existing current density changes over time, it does not directly account for changes in the current density due to sources or sinks of charged particles. As such, we require a way to include growth in the current density produced by ionization of the background neutrals during the process of current sheet formation. To quantify the influence of ionization in increasing the current density, we estimate the rate of ionization of the neutrals by defining a characteristic ionization reaction rate, $K_{iz}$, as[73]

$$K_{iz} \approx \sigma_0 v_{th,e} \left(1 + \frac{2T_e}{U_{iz}}\right) \exp\left(-\frac{U_{iz}}{T_e}\right) , \tag{4.19}$$

where

$$\sigma_0 = \pi \left(\frac{e}{4\pi\varepsilon_0 U_{iz}}\right)^2 \tag{4.20}$$

is the Thomson cross section expanded near the ionization energy, $U_{iz}$, and $v_{th,e} = \sqrt{8eT_e/\left(\pi m_e\right)}$ is the electron thermal velocity. In the expression for the thermal velocity, $e$ is the elementary charge and $m_e$ is the electron mass. We note that, as defined, $K_{iz}$ has units of $\mathrm{m}^3/\mathrm{s}$.

To calculate our characteristic ionization rate, we require an estimate of the electron temperature, $T_e$. Following Little et al.[31], we can write the plasma resistivity in terms of the relevant collision frequencies as

$$\eta_{sd} = \frac{m_e\left(\nu_{ei} + \nu_{en}\right)}{n_{sd} e^2} , \tag{4.21}$$

where $\nu_{ei}$ and $\nu_{en}$ are the electron-ion and electron-neutral collision rates, respectively, and $n_{sd}$ is the charged particle density in the skin layer. The electron-ion collision frequency can be modeled as

$$\nu_{ei} = \frac{\sqrt{2}Z^2 e^{5/2}}{12\pi^{3/2}\varepsilon_0^2\sqrt{m_e}} \log\left(\Lambda\right) n_{sd} T_e^{-3/2} \tag{4.22}$$

where $\ln\left(\Lambda\right)$ is the Coulomb logarithm, $Z$ is the ionic charge, and $T_e$ is the electron temperature in eV. The electron-neutral collision frequency can be expressed in the form

$$\nu_{en} = n_n \sigma_{en} \sqrt{\frac{8eT_e}{\pi m_e}}\,, \tag{4.23}$$

where $n_n$ is the neutral density and $\sigma_{en}$ is the average electron-neutral momentum transfer cross section for the gas species of interest. If we assume that the plasma density inside the skin layer is larger than the neutral density for much of the formation process, we can approximate $\nu_{ei} \gg \nu_{en}$. With this simplification, equation (4.21) becomes the Spitzer resistivity, which we can use to relate $T_e$ to $\eta_{sd}$ according to

$$T_e = \left(\frac{\sqrt{2em_e}Z^2 \log\Lambda}{12\pi^{3/2}\varepsilon_0^2}\frac{1}{\eta_{sd}}\right)^{2/3} \approx \left(\frac{1.446\times 10^{-3}}{\eta_{sd}}\right)^{2/3}\,. \tag{4.24}$$

Note that for our approximate expression we have used $Z = 1$ and $\log\Lambda = 14$. For our calculation of $\tau_{iz}$, the average $T_e$ over the ionization and formation phases is used. With a method to calculate the characteristic ionization rate in hand, we now seek to estimate how significant ionization will be in increasing the current density in the sheet. To accomplish this, we define a characteristic ionization timescale based on $K_{iz}$,

$$\tau_{iz} = \frac{1}{n_{n,0}K_{iz}}\,, \tag{4.25}$$

where we note that the ideal gas law may be used to express the neutral density ($n_{n,0}$) in terms of the fill pressure, $p_0$, and the temperature of the neutral gas prior to the thruster discharge, $T_n$.

We have so far argued that both ionization and diffusion will contribute to the evolution of the current density in the current sheet. We now propose that it is the combined influence of these two effects on the current density that results in the formation of the sheet. Ionization may be thought of as a source term for current due to the production of charged particles. As these newly formed charged particles are driven by the induced fields, they become part of $J_\theta$ and their evolution becomes dictated by diffusive processes. Should the rate of ionization be high and the current density slow to diffuse, current will tend to accumulate in a thin region, eventually resulting in the formation of a current sheet. If the opposite is true, however, current will dissipate rather than accumulate and a sheet will fail to form.

In cases between the two extremes, i.e., when both the ionization and diffusivity are either high or low, the end result becomes less obvious. A high ionization rate will generate sufficient charged particles for driving current but if the diffusivity is also high then these particles can easily escape the regions where they were produced and are less likely to accumulate. Similarly, if the diffusivity is low but so too is the ionization rate, then the current will tend to concentrate but its growth will be hindered by a lack of charged particles. In such cases, we hypothesize it is the relative strength of the two effects that will determine whether or not a sheet is formed. Using our characteristic timescales for the ionization and diffusion processes, we can express this claim in terms of the following dimensionless inequality

$$\frac{\tau_d}{\tau_{iz}} = \frac{\mu_0 z_{dc}^2 \left(n_{n,0} K_{iz}\right)}{\eta_{sd,max}} \gtrsim \mathcal{T}_{\text{crit}} \, , \tag{4.26}$$

where $\mathcal{T}_{\text{crit}}$ is some critical value above which the combined effects of current concentration and growth are sufficient to produce a well-formed, magnetically impermeable current sheet.

We note that there is also likely to be a certain degree of synergy between the two effects. For example, when the diffusivity is low we would expect $J_\theta$ to tend to be more concentrated than if the diffusivity was high. This greater concentration of $J_\theta$ is expected to, in turn, increase the localized Ohmic heating. Greater heating is then anticipated to raise the electron temperature in this region, resulting in an increase in the ionization rate. This increased ionization rate would proceed to further increase the current density, leading to still greater localized Ohmic heating and so on and so forth. Given this interplay, we expect that the strength of the current sheet will exhibit a relatively strong non-linearity around the critical value.

**Table 4.1:** Experiment parameters for data sets used in scaling analysis.

| Set # | $C_{\mathrm{mb}}$ [µF] | $p_0$ [mTorr] | $V_{\mathrm{pi},0}$ [kV] | $V_{mb,0}$ [kV] | Gas |
|---|---|---|---|---|---|
| 1 | 1.5 | [1.5, 2, 2.5, 3, 5] | 1 | 2 | Ar |
| 2 | 1.5 | 3.07 | [0.5, 0.75, 1, 1.25, 1.5] | 1.5 | Ar |
| 3 | 1.5 | [0.5, 1, 1.5, 2, 2.5, 3, 4, 5, 6, 8] | 1 | 2 | Kr |
| 4 | 1 | [2.03, 3.04] | 1 | 2 | Ar |
| 5 | 1.5 | 3.0 | 0.5 | [1, 2] | Ar |
| 6 | 1.5 | [3.05, 5] | 1 | 1.5 | Ar |
| 7 | 1.5 | [1.03, 3.03, 5.02] | 1 | 1 | Ar |
| 8 | 1.5 | 3.0 | [0.5, 0.75, 1, 1.5] | 1.5 | Kr |
| 9 | 1.5 | [1.6, 2.3, 3.0, 3.8, 4.5, 5.3, 6.1, 6.9, 7.7, 8.7, 9.5, 10.4, 11.3, 12.2] | 1 | 2 | Ar |

To examine how current sheet strength scales with our proposed parameter, we collected data across a range of operational conditions. Among the variables changed were $C_{mb}$, $p_0$, $V_{pi,0}$, and $V_{mb,0}$. In addition, the backfill gas species was also altered, with both argon and krypton gases being investigated. Table 4.1 lists the experimental conditions at which sets of data were taken. Within each set, only one variable was changed while the others remained fixed; this variable is shown as a bracketed list in Table 4.1.

Figure 4.7 shows our two dimensionless metrics for the strength of the current sheet plotted against our proposed scaling parameter, i.e., the ratio of the current diffusion to the ionization timescale, $\tau_d/\tau_{iz}$, for each of the sets in Table 4.1. Figure 4.7(a) shows that $k_{max}$ scales positively with $\tau_d/\tau_{iz}$ over the range investigated. This indicates that increasing $\tau_d/\tau_{iz}$ results in the current distribution within the current sheet being concentrated closer towards the drive coil at the start of the acceleration phase. This is consistent with the "upstream localization" of the current density that we have proposed occurs during the formation of the current sheet in our device[60].

We note, however, that the scaling of $k_{max}$ with $\tau_d/\tau_{iz}$ is logarithmic in nature and thus fairly weak. This suggests that $\tau_d/\tau_{iz}$ does not greatly affect the location of the current distribution at the start of the acceleration phase. One possible explanation for this is to consider $k$ as dependent upon the location of the centroid of the current distribution. If low levels of current are driven in a broad region of plasma during the ionization or early formation phase, a very strong upstream localization effect may be required to significantly move the centroid upstream. Another possibility is that the upstream motion due to localization of the plasma current may be counteracted to an extent by an increase in downstream acceleration during formation. This is to say that, although a strong current sheet may be formed, it is also more strongly repelled by the drive coil during the formation process, leading the location of the centroid of the current distribution to be relatively insensitive to $\tau_d/\tau_{iz}$.

Figure 4.7(b) shows that the dimensionless current density is relatively insensitive to $\tau_d/\tau_{iz} \lesssim 10$ but becomes highly sensitive above this threshold value. This suggests that the diffusive timescale must be long relative to the ionization timescale for significant concentration of current to occur. In other words, when $\tau_d/\tau_{iz} \gg 1$, charged particles formed by ionization of the background neutrals are able to accumulate in the current sheet and participate in further ionization rather than diffusing away. This leads to a rapid rise in the sheet electron density and causes the current density to increase dramatically. We also propose that the rapid rise in the current density has compounding effects in that it increases the rate of ionization as a result of enhanced localized Ohmic heating.

The error bars in Figure 4.7 were determined by propagating measurement uncertainty associated with the diagnostics, estimated repeatability, and, where applicable, the fit procedure described in section 4.3.2. We note, however, that sources of measurement error were not exhaustively considered but rather estimated from, and optimistically assumed to be minimized by, the calibration procedure. This is to say that, effects such as probe misalignment, positioning effects, and other departures from idealized diagnostic operation have not been individually considered. Nonetheless, we posit that the largest source of uncertainty in our data set stems from the fitting procedure used to calculate $J_0$, $\delta_{sd}$, and $z_{null}$. Evidence

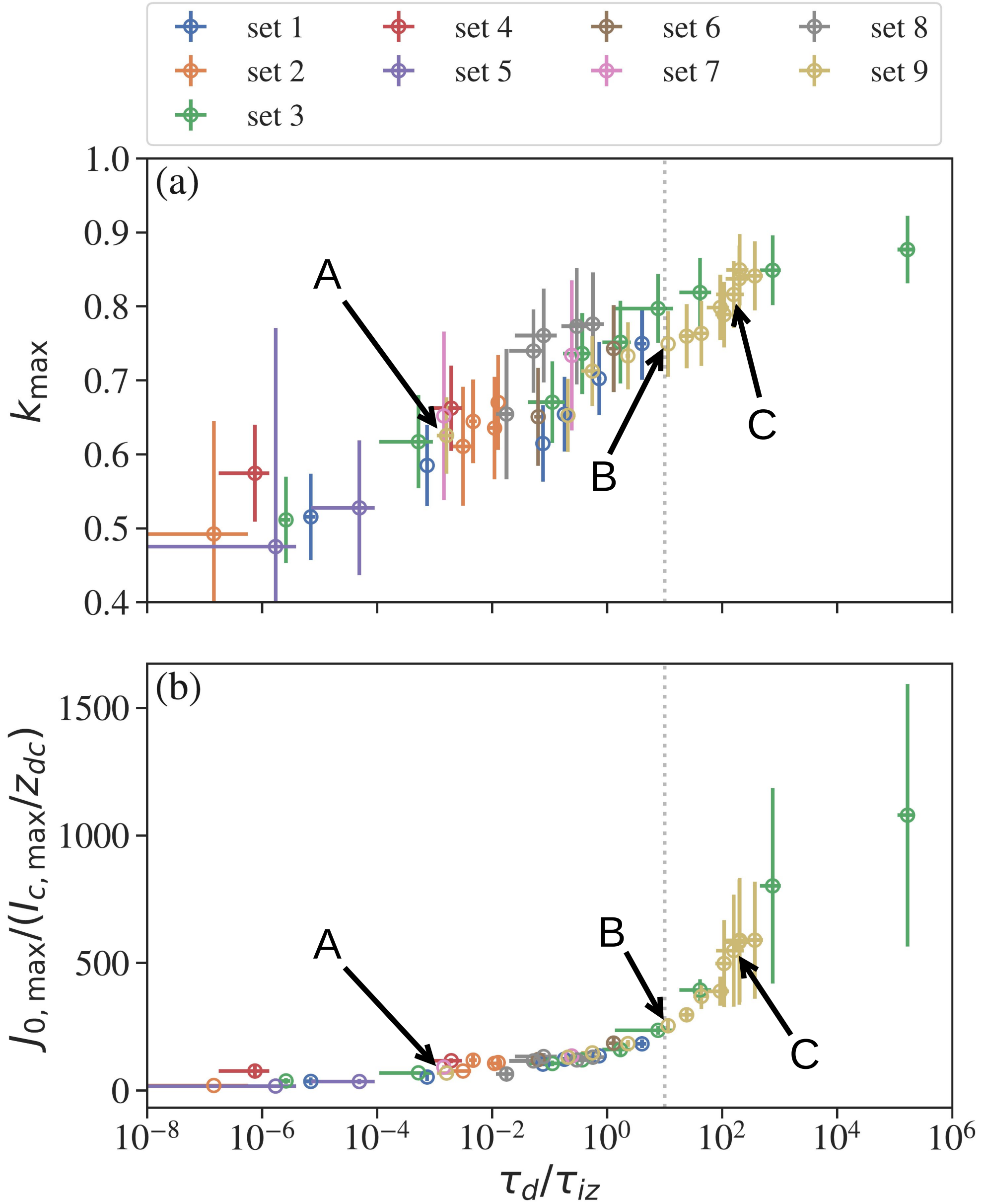

**Figure 4.7:** Scaling of (a) inductive coupling coefficient and (b) dimensionless current density with the ratio of the diffusion to ionization timescales.

of this may be seen in the increase in the size of the y-axis error bars in Figure 4.7(b) at larger $\tau_d/\tau_{iz}$. This rise in uncertainty is attributed to the steepening of the $B_{r_p}$ profile as

$J_0$ increases, which causes the uncertainty associated with the $B_{r_p}$ fitting procedure to grow larger.

Given that both $\tau_d$ and $\tau_{iz}$ contain dependencies on $\eta_{sd}$, it is reasonable to consider whether the total energy from Ohmic heating, $E_h$, found in the numerator of the formation parameter ($\Omega_{form}$) proposed by Little et al.[31] might also be a useful scaling parameter. We can evaluate $E_h$ directly by integrating $I_p$ and $R_{sd}$ over time. We found, however, that neither $k_{max}$ nor $\hat{J}_0$ scaled universally with $E_h$ across all cases. This may be due to localization effects not being well captured by this quantity. In the case where the current and heating become localized in a narrow layer early on, the resistivity in this layer may be fairly small over much of the ionization and formation phases. While $E_h$ would be relatively low in this case, we would expect $\tau_d/\tau_{iz}$ to be fairly high on account of the low resistivity and likely higher temperature. We note that a direct evaluation of $\Omega_{form}$ was not possible from our data due to not having a reliable estimate of the $m_{bit}$ ultimately swept up by the sheet. This precluded the calculation of the denominator of this parameter, i.e., the total ionization energy, $E_{ion}$.

It is of interest now to compare the time evolution of key current sheet parameters for differing values of $\tau_d/\tau_{iz}$. Figure 4.8 shows the evolution of the circuit and plasma currents, inductive coupling, current density, skin depth, and resistivity for three representative cases. The values of $I_{c,max}$, $k_{max}$, and $J_{0,max}$ used to calculate the scaling parameters are marked by the hollow circles in their respective subplots. The three cases selected have $\tau_d/\tau_{iz}$ less than, approximately equal to, and greater than the threshold value of $\tau_d/\tau_{iz} \approx 10$, as seen in Figure 4.7. Comparing the evolution of the selected current sheet parameters between these cases, we find that while the parameters evolve in a similar fashion, $k$ and $J_0$ are generally higher in all phases as $\tau_d/\tau_{iz}$ increases.

The difference in $k$ and particularly $J_0$ between cases is most pronounced at the end of the formation phase. We hypothesize that the cause of this departure is the larger $\eta_{sd}$ observed during the ionization and formation phases for smaller $\tau_d/\tau_{iz}$. To see why this may be the case, we can examine how $\tau_d/\tau_{iz}$ is related to $\eta_{sd}$. From equation (4.18) and (4.25),

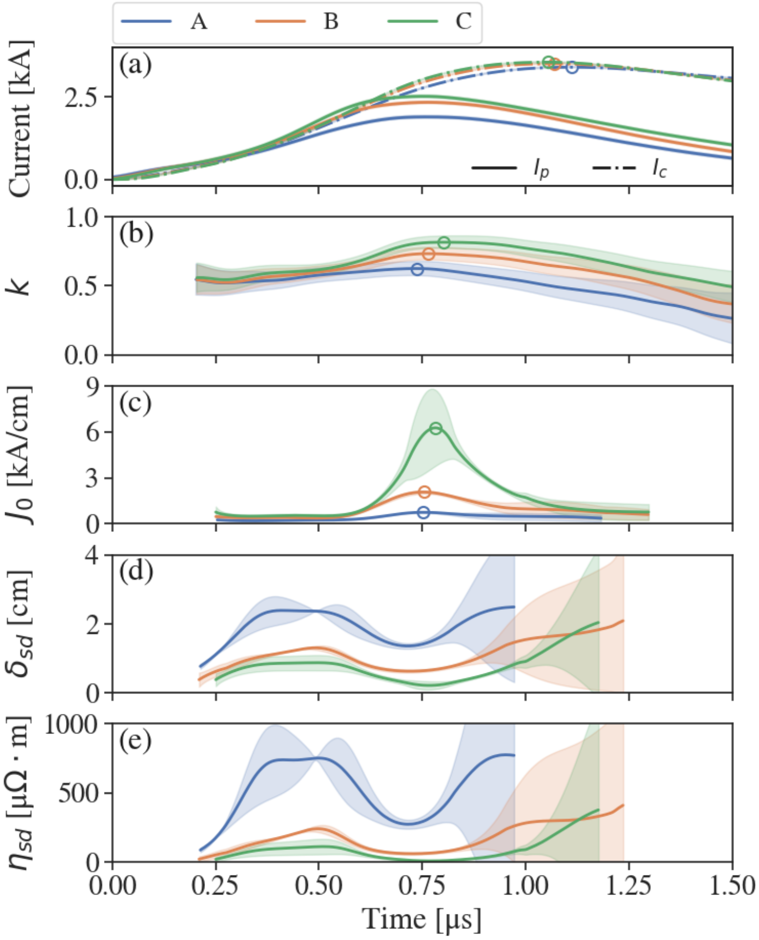

**Figure 4.8:** Time-histories of (a) $I_c$ and $I_p$, (b) $k$, (c) $J_0$, (d) $\delta_{sd}$, and (e) $\eta_{sd}$ for cases with $\tau_d/\tau_{iz}$ below, near, and above 10.

we find, ignoring constants and lower order terms, that

$$\frac{\tau_d}{\tau_{iz}} \sim \frac{1}{\eta_{sd}^2 \exp\left(a\, \eta_{sd}^{2/3}\right)}, \tag{4.27}$$

where $a$ is an arbitrary constant. To the extent that this simplified scaling holds, we would thus expect diffusion to be stronger relative to ionization when $\eta_{sd}$ is large and vice versa. Applying this concept to the evolution of $\eta_{sd}$ shown in Figure 4.8(e), we propose that a larger $\tau_d/\tau_{iz}$ implies that diffusion is generally weaker relative to ionization throughout the ionization and formation phases and not just at the end of the formation phase.

### *Effects of Operational Parameters on Current Sheet Formation*

Having established a scaling law for the strength of the current sheet, we now seek to connect our scaling parameter to the operational parameters of an IPPT, such as the mass bit ($m_{bit}$) and initial charging voltages on the capacitor banks. Figure 4.9(a) shows that increasing $p_0$, which for a static backfill may be considered related to $m_{bit}$, was generally found to increase $\tau_d/\tau_{iz}$. It was previously found that higher $p_0$ appeared to result in Ohmic heating becoming localized in a narrower region of plasma[60]. This was posited to lead to an increase in the local electron temperature in this region and a corresponding decrease in the skin depth and resistivity. As $\eta_{sd}$ decreases, we would expect that $D_\perp$ would also decrease and thus $\tau_d$ will increase. Equation (4.25) shows that $\tau_{iz}$ should be inversely proportional to $p_0$ as a result of higher neutral particle density. If $T_e$ is indeed higher in the localized heating region, $K_{iz}$ will also increase, trending $\tau_{iz}$ smaller.

These results suggest that there is a benefit, at least in regards to the formation of the sheet, to having a sufficiently large $p_0$ or $m_{bit}$. It is expected that there is a limit to the benefits of increasing $m_{bit}$, however, which appears to be confirmed by Figure 4.9(a). At most, $m_{bit}$ can only be increased until the associated total ionization energy equals the initial stored energy, $E_0$. Beyond this, there is not enough stored energy to ionize and heat all the gas; it is this balance that is described by the formation parameter of Little et al.[31] The plasma resistivity will increase in this case, resulting in a decrease in $\tau_d/\tau_{iz}$. It is likely that the limit is lower than this idealized value on account of energy inefficiencies and the fact that not all of the stored energy can be coupled into the plasma at once. For the cases in Table 4.1, $E_0/E_{iz}$ was always greater than four and in many cases was greater than ten. This suggests that we were operating in a regime that was well away from this energy limit and thus did not encounter the hindering effects of excessive $m_{bit}$. This agrees with the roll-off of $\tau_d/\tau_{iz}$ shown at higher $p_0$ for sets 1 and 9 in Figure 4.9(a).

The scaling of $\tau_d/\tau_{iz}$ with $V_{pi,0}$ in our device may provide insight into the role of PI

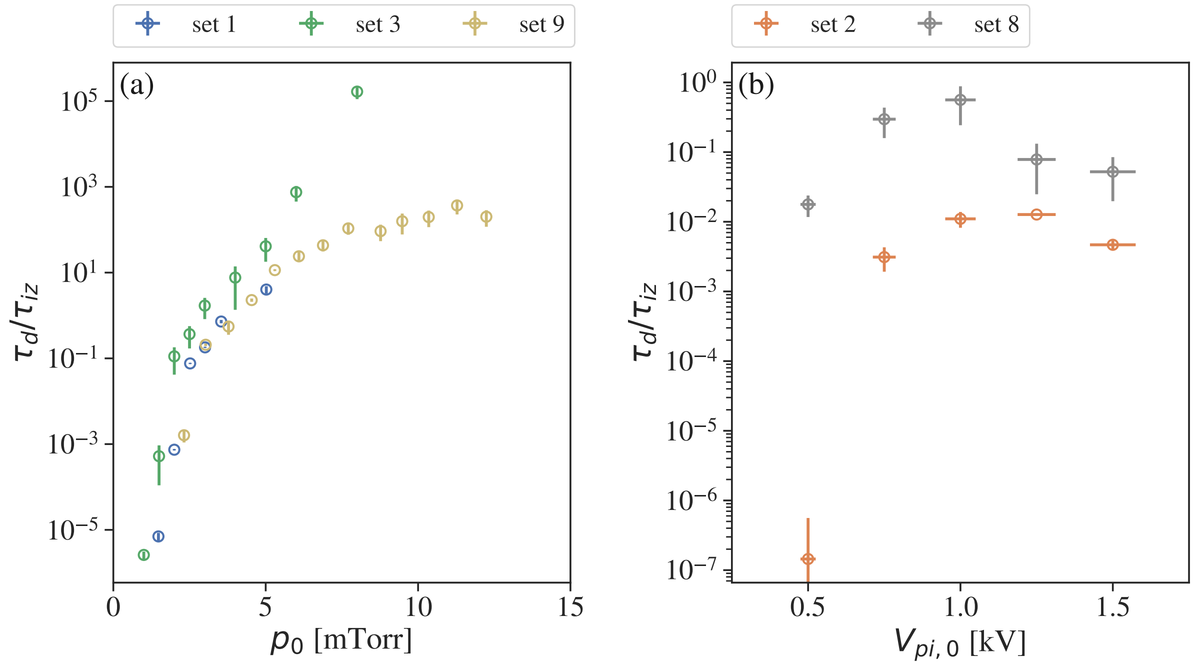

**Figure 4.9:** Variation of the ratio of the diffusive to ionization timescales with (a) fill pressure and (b) initial PI voltage. The fill gas in sets 1, 2, and 9 is argon, while for sets 3 and 8 it is krypton.

in IPPTs. Figure 4.9(b) shows that $V_{pi,0}$ is initially found to increase $\tau_d/\tau_{iz}$ to a point. Previously we have shown that increasing $V_{pi,0}$ leads to an increase in the skin depth and plasma resistivity during the ionization phase as well as a shortening of the ionization phase duration[60]. We postulated this to be due to increased $V_{pi,0}$ ionizing a broader region of gas that was then quenched during the ionization phase, resulting in much higher Ohmic heating during the ionization phase. This in turn causes $\eta_{sd}$ to drop earlier, which we posit initiates an earlier transition to higher $\tau_d/\tau_{iz}$ and allows for increased localization of the current density and improved inductive coupling. As such, the role of PI, beyond breaking down the neutral gas, appears to be to provide a region of moderate resistivity plasma in which Ohmic heating can localize and begin concentrating charge carriers via intense ionization.

As $V_{pi,0}$ continues to increase, however, $\tau_d/\tau_{iz}$ appears to level off or even slightly decline. The exact $V_{pi,0}$ at which this change in trend occurs appears to depend somewhat on the fill gas. We hypothesize that this is due to the region of gas ionized by the PI system broadening as $V_{pi,0}$ increases. As the region of gas broadens, it is expected to encounter background neutrals and undergo quenching. This results in an increase in the peak resistivity and thereby a decrease in $\tau_d/\tau_{iz}$. We note that it may prove possible to circumvent this trend by changing the method of PI. One possibility may be to use a high power RF generator of sufficiently high frequency connected directly to the drive coil[75]. This method of PI might ionize a narrower region of plasma to higher temperatures, potentially providing a region of plasma that already possess a high $\tau_d/\tau_{iz}$ for the main discharge to couple to.

When holding the other parameters approximately constant, changing the gas species from argon to krypton was observed to increase $\tau_d/\tau_{iz}$ in Figure 4.9. This may be due to the ionization rate differing between the two gases. Krypton has a slightly lower ionization energy than argon as well as a larger ionization cross section, which will tend to decrease the ionization timescale. Extrapolating these effects to a gas such as nitrogen, we would expect increased diffusion and reduced ionization which would likely need to be compensated for by other means, such as by raising $p_0$ or increasing $V_{pi,0}$ or $V_{mb,0}$.

While the trends discussed above are insightful, ultimately what we seek is a single equation or metric which connects the primary thruster operating and design parameters to the strength of the current sheet. By combining equations (4.18), (4.25), and (4.24), we find that our scaling parameter $\tau_d/\tau_{iz}$ can be written as a function of several thruster design parameters and the ratio of the electron temperature, $T_e$, to the ionization energy, $U_{iz}$,

$$\frac{\tau_d}{\tau_{iz}} = \mathcal{C}_1 n_{n,0} z_{dc}^2 \left(\frac{T_e}{U_{iz}}\right)^2 \left[1 + 2\left(\frac{T_e}{U_{iz}}\right)\right] \exp\left(-\frac{U_{iz}}{T_e}\right) , \tag{4.28}$$

where $\mathcal{C}_1$ is a constant given by

$$\mathcal{C}_1 = \frac{3}{2}\left(\frac{\mu_0 e^2}{m_e Z^2 \log\left(\Lambda\right)}\right) \approx 3.79 \times 10^{-15} . \tag{4.29}$$

With equation (4.28) in hand, the objective now becomes estimating $T_e$, and thereby $\tau_d/\tau_{iz}$, from some combination of thruster operating and design parameters.

As a starting point, we consider a plasma with a total electron thermal energy described by

$$E_{th,e} = \frac{3}{2} N_e k_B T_e \tag{4.30}$$

where $N_e$ is the total number of electrons in the plasma and $k_B$ is the Boltzmann constant. Note that, following others, e.g., Martin[30], we have treated the electrons as a monatomic ideal gas. We now assume that some fraction of the total initial stored energy, $E_0 = E_{mb,0} + E_{pi,0}$, goes into ionization and heating of the gas. The estimated change in thermal energy due to this energy input is then

$$\Delta \left( k_B T_e \right) = \frac{2}{3} \frac{Q_{\text{heating}}}{N_e} \, , \tag{4.31}$$

where $Q_{\text{heating}}$ is the total heat energy supplied to the plasma.

If we prescribe the region of interest for plasma heating as the volume contained within the decoupling distance of the coil, we can approximate $N_e \approx z_{dc} A_{rz} n_e$, where $A_{rz}$ is the annular area of the drive coil and $n_e$ is the average electron density. Since we are using the approximation of a fully ionized plasma, we can write $n_e \approx n_{n,0}$, where $n_{n,0}$ is the initial neutral density in front of the coil face. If we then express the total heating energy as $Q_{\text{heating}} = X \left( E_0 - E_{iz,\text{eff}} \right)$, where $X$ is an arbitrary scaling factor and $E_{iz,\text{eff}}$ is the effective energy required to ionize all propellant within the decoupling distance, then the resulting electron temperature is

$$T_e = \frac{2}{3} X U_{iz,\text{eff}} \left( \frac{E_0}{E_{iz,\text{eff}}} - 1 \right) \, . \tag{4.32}$$

For simplicity, we have assumed $T_{e,0} \approx 0$ in this derivation. In equation (4.32), $E_{iz,\text{eff}} = N_e U_{iz,\text{eff}}$, where $U_{iz,\text{eff}}$ is the effective ionization energy for a single atom of the propellant species. $U_{iz,\text{eff}}$ is usually several times the nominal first ionization energy, $U_{iz}$[73].

Despite its simplicity, equation (4.32) contains the many of the sought after thruster operational design parameters, such as the discharge energy, decoupling distance, drive coil area, and propellant density and ionization energy. From a thruster design standpoint, equation (4.32) predicts that $T_e$ will increase with discharge energy. Equation (4.32) also shows that selecting a propellant with a lower first ionization energy should increase $T_e$ by way of consuming less of the discharge energy during the ionization process. Recalling that $E_{iz,\text{eff}} = n_{n,0} z_{dc} A_{rz}$, the denominator of equation (4.32) predicts that $n_{n,0}$, $z_{dc}$, and $A_{rz}$ should be decreased to maximize $T_e$. This is due to the relationship of these factors with the total number of particles, with fewer particles for a given input energy resulting in a higher $T_e$ for those particles. For a thruster operating with quasi-steady propellant injection, this is equivalent to predicting a higher $T_e$ for a smaller propellant flow rate.

The scaling factor $X$ is meant to capture, to the degree possible, the complex physics that have been glossed over in this simplified approach. This includes factors such as the degree of inductive coupling between the drive coil and sheet, upstream localization of the Ohmic heating, and energy losses due to ionization and radiation. To determine its value, we can inspect equation (4.32) for predicted trends that differ from what is observed in the data. In our earlier discussion, we found that the $T_e$ estimated directly from the measured skin depth resistivity decreased as $p_0$ (or $n_{n,0}$) was increased. This was attributed to an increase in the upstream localization effect, which led the heating to be concentrated in a narrower volume of plasma. This is opposite to the trend predicted by equation (4.32), which would have $T_e$ decrease with $p_0$. This suggests that $X = f(p_0)$, i.e., that the scaling factor should have an internal pressure dependence. As such, we assume a form

$$X \approx \frac{p_0^d}{b}\,, \tag{4.33}$$

where $b$ and $d$ are constants. Fitting equation (4.32) to the measured data with the form of $X$ given in equation (4.33) given $b \approx 10$ and $d \approx 2$.

A comparison of the measured $T_e$ with that predicted by equation (4.32) using the empirical fitting constants is shown in Figure 4.10. The predicted temperatures shown in Figure 4.10 are generally found to be in agreement with the measured values, indicating that our simplistic model is able to capture the key physics at play to at least some degree. We note, however, that most of the variation in $T_e$ in Figure 4.10 was achieved through changing $p_0$. Sets where $E_0$ was swept, by way of adjusting either $V_{mb,0}$ or $V_{pi,0}$, were generally found

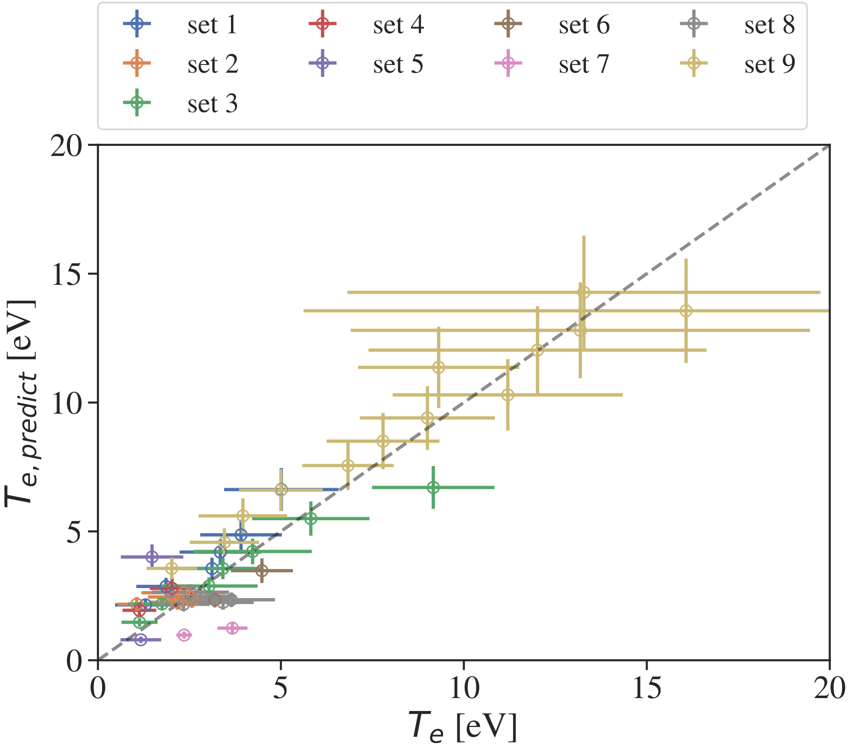

**Figure 4.10:** Comparison of measured $T_e$ to predicted $T_e$ after fitting empirical correction function $X$.

to have a more restrained effect on $T_e$ within the range of values tested. As a result, many of the points for these sets are clustered and, in some cases, the resulting variation in $T_e$ was within the range of uncertainty for the set. As such, the data are generally too ambiguous to conclude whether equation (4.32) accurately represents the changes in $T_e$ due to factors other than $p_0$.

Further examination of equation (4.32), however, suggests that the empirical scaling factor may only be valid over the range of operational parameters tested. Clearly, a compact thruster operated at very high discharge energy and fill pressure would, according to equation (4.32), produce an unphysically large $T_e$. As such, it appears that our simple formulation lacks a regulating mechanism by which to keep $T_e$ in check as the various operational parameters become either large or small. Consequently, the degree to which equation (4.32) extends beyond the present data sets is unknown. Nonetheless, the ability of a simple formulation such as equation (4.32) to predict with reasonable accuracy the electron temperature in the current sheet suggests that it may be possible to more broadly link the strength of the current sheet to the thruster operating and design parameters.

Having obtained an expression for $T_e$ in terms of the thruster design and operational parameters, we return to our original objective of determining how the strength of the current sheet scales with these parameters. We start by simplifying equation (4.32) using the assumption that $E_0/E_{iz,\mathrm{eff}} \gg 1$, i.e., that the discharge energy is significantly larger than the energy required to ionize all propellant within the decoupling distance. We note that this assumption is equivalent to stating that the thruster operates well above the critical specific energy proposed by Mikellides et al.[32, 26] While this condition is satisfied in many of the cases in Table 4.1, there are a few cases where $E_0$ is only slightly larger than $E_{iz,\mathrm{eff}}$. Examples of these are the lower $V_{mb,0}$ case of set 5 and the higher pressure cases in set 7.

Using our simplified version of equation (4.32), we can substitute into equation (4.28) to find

$$\frac{\tau_d}{\tau_{iz}} = \mathcal{C}_1 n_{n,0} z_{dc}^2 \left[\mathcal{E}^2 \left(1 + 2\mathcal{E}\right) \exp\left(-\frac{1}{\mathcal{E}}\right)\right] , \tag{4.34}$$

where

$$\mathcal{E} = \frac{2}{3} X \left(\frac{E_0}{E_{iz,\mathrm{eff}}}\right) . \tag{4.35}$$

To examine the validity of equation (4.34), we compare the values it predicts with those calculated directly from the experimental data using equations (4.18) and (4.25). This comparison is shown in Figure 4.11. While agreement at very small values of $\tau_d/\tau_{iz}$ is found to be poor in some cases, the agreement improves significantly above $\tau_d/\tau_{iz} \approx 1 \times 10^{-3}$ to $1 \times 10^{-2}$. Since it is the higher values of $\tau_d/\tau_{iz}$ that are associated with current sheet formation, Figure 4.11 indicates that the approximate expression given by equation (4.34) remains able to predict when current sheet formation will occur with reasonable accuracy.

Equation (4.34) is an expression for our dimensionless scaling parameter that is a function

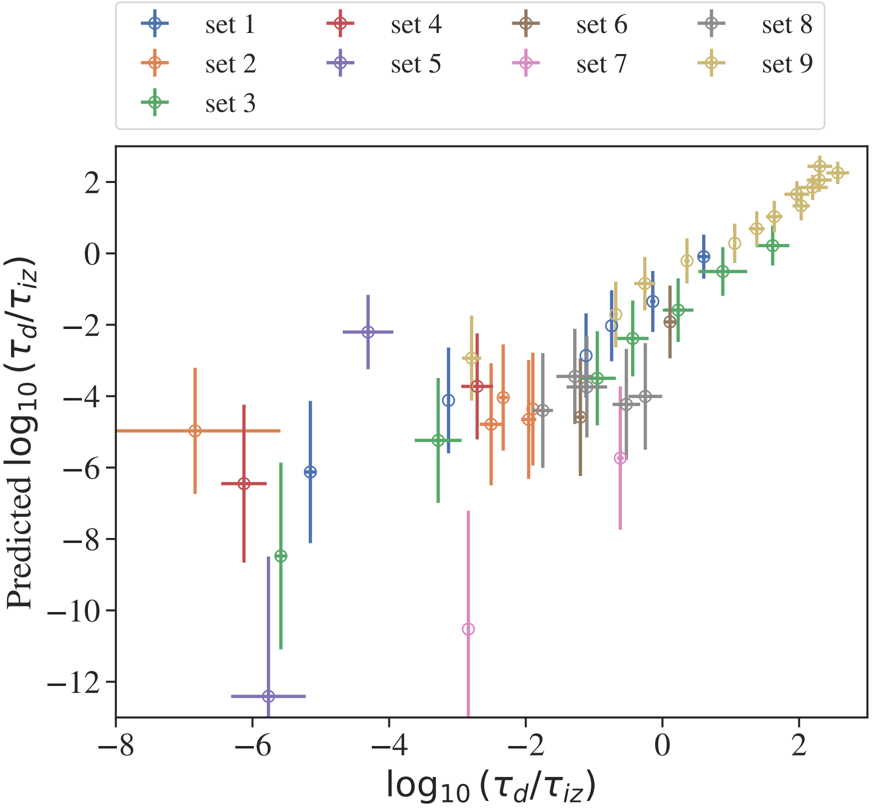

**Figure 4.11:** Comparison of $\tau_d/\tau_{iz}$ predicted by equation (4.34) with values calculated directly from experimental data. Note that it is the $\log_{10}$ of the timescale ratio that is plotted here.

of only thruster design and operational parameters. Specifically, the parameters included are the initial propellant density or pressure ($n_{n,0}$ or $p_0$), electromagnetic decoupling distance ($z_{dc}$), drive coil dimensions ($A_{rz}$), the propellant ionization energy ($U_{iz}$), and the discharge energy ($E_0$). If we now use our critical value of $\tau_d/\tau_{iz} \approx 10$, we arrive at the following inequality which describes the combination of thruster parameters required to form a magnetically impermeable current sheet:

$$\mathcal{C}_1 n_{n,0} z_{dc}^2 \left[\mathcal{E}^2 \left(1 + 2\mathcal{E}\right) \exp\left(-\frac{1}{\mathcal{E}}\right)\right] \gtrsim 10\,. \tag{4.36}$$

To demonstrate the utility of equation (4.36), we can imagine a case where the thruster designer must determine a discharge energy and mass bit at which to operate the thruster. To maximize performance, the thruster should be capable of forming a magnetically impermeable current sheet and accelerating it efficiently. Polzin[28, 16] has shown that the thrust efficiency of a planar IPPT is related to the dynamic impedance parameter

$$\alpha = \frac{E_0\left(CL_c\right)}{m_{\text{bit}} z_{dc}^2}\,, \tag{4.37}$$

where $m_{\text{bit}}$ is the mass bit, $C$ is the bank capacitance, and $L_c$ is the coil inductance. In addition, Polzin found that efficiency was typically optimized at values of $\alpha$ between 1 and 3. Thus to meet the sought after characteristics, the thruster parameters should produce $\tau_d/\tau_{iz} \gtrsim 10$ and $\alpha = 1$ to 3 when input into equations (4.34) and (4.37), respectively.

To determine the optimal values for $E_0$ and $m_{\text{bit}}$, equation (4.34) may be used to construct contours of $\tau_d/\tau_{iz}$. Figure 4.12 shows contours of constant $\tau_d/\tau_{iz}$ as well as the range of parameter space that falls within $1 \le \alpha \le 3$ (dotted lines). Figure 4.12 suggests that magnetically impermeable current sheets are most effectively formed at larger $E_0$ and $m_{\text{bit}}$. When both of these parameters are small, Figure 4.12 predicts that any current sheet that is formed will be highly permeable. In contrast, the dotted lines of constant $\alpha$ indicate that efficient acceleration can occur over a range of $E_0$ and $m_{\text{bit}}$. This is due to the balancing effect between these two parameters in equation (4.37), wherein the effects of increases in $E_0$ can be countered by also raising $m_{\text{bit}}$.

Within the range of $E_0$ and $m_{\text{bit}}$ examined, we observe that there are regions where both effective current sheet formation and efficient acceleration can occur. We note, however, that are also areas where a current sheet can be formed but not efficiently accelerated and vice versa. Figure 4.12 thus shows the importance of considering both current sheet formation and acceleration when selecting the operating regime for an IPPT. Moreover, it suggests that models which take sheet formation as a given are likely to produce inaccurate predictions for certain regions of the parameter space. In particular, we anticipate that models that presume the existence of the current sheet are least accurate in the region of low $E_0$ and

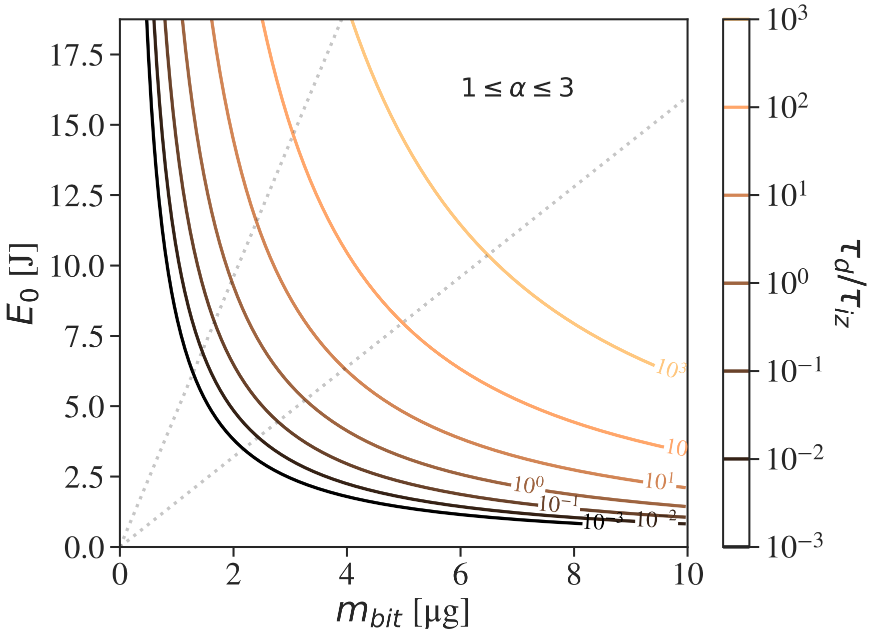

**Figure 4.12:** Contours of $\tau_d/\tau_{iz}$ for a hypothetical range of $E_0$ and $m_{\mathrm{bit}}$. For this plot, $L_c = 375\,\mathrm{nH}$, $C = 1.5\,\mu\mathrm{F}$, $z_{dc} = 3\,\mathrm{cm}$, $A_{rz} = 151\,\mathrm{cm}^2$, and propellant is argon.

$m_{\mathrm{bit}}$; precisely the parameter space where high pulse rate IPPTs are expected to operate. As such, we expect that these models will require modifications to accurately predict the performance scaling of these devices.

## *4.4 Conclusions*

We have applied recently published methods for examining the evolution of the current sheet produced by a planar IPPT to new data collected from a compact, research prototype IPPT operating across a range of conditions. The processed data was then used to investigate how current sheet formation scales in such a device. Two metrics for the strength of the current sheet were proposed, namely the maximum inductive coupling coefficient and a maximum non-dimensional current density. The first represents the degree of inductive coupling at the start of the acceleration phase while the second is a measure of the effectiveness with which current in the drive coil is able to produce a concentrated, localized current in the plasma.

We found that both proposed metrics for current sheet strength scaled well with the ratio of the characteristic diffusion to ionization timescales. We identified a critical value of $\tau_d/\tau_{iz} \approx 10$, above which the current density metric increased rapidly with further increases in the timescale ratio. We also showed that this new scaling parameter describes the competition between resistive diffusion and ionization in the concentration of the electrons which comprise the localized azimuthal current density that is fundamental to the formation of the current sheet. In addition, we have provided preliminary evidence that it is the cross field diffusion of magnetized electrons that is the dominant mechanism by which the plasma current is diffused.

Through our new scaling parameter, we were able to examine how various operational parameters of the thruster affected the formation of the current sheet. Generally, $\tau_d/\tau_{iz}$ was found to scale with $p_0$ and $V_{pi,0}$ although for somewhat different reasons. The increase in localization of the Ohmic heating observed with $p_0$ was found to result in lower resistivities within the heated region, leading to a decrease in diffusion and an increase in the ionization rate. The increase in Ohmic heating during the ionization phase that appears when increasing $V_{pi,0}$ was thought to cause an earlier transition to higher $\tau_d/\tau_{iz}$, allowing more time for electrons to accumulate in the sheet. The propellant species was also found to have an effect, as shown by the increase in $\tau_d/\tau_{iz}$ when changing the gas species from argon to krypton. We hypothesized that the lower ionization energy and ionization cross section of krypton increased the ionization rate.

Finally, an initial attempt was made to link the thruster operational and design parameters to the strength of the current sheet. A simple equation involving many key thruster parameters, including the discharge energy, initial neutral density in front of the coil face, drive coil dimensions, and electromagnetic decoupling distance, was shown to predict $T_e$, and by extension $\tau_d/\tau_{iz}$, in reasonable agreement with the measured values. The validity of the equation obtained, however, appeared to be limited to the range of parameters tested. Nonetheless, the agreement suggests that it may be possible to forge a broader link. While the approach presented here used a combination of first principles and empirical fitting, efforts to expand upon this initial attempt may find success in a more formal dimensional analysis procedure.

The new scaling law presented here addresses a deficiency in the literature in that it describes, for the first time, how the formation of the current sheet itself scales. Previous scaling laws found in the literature largely relied on simplified models of the current sheet and focused on the scaling of thruster performance, assuming *a priori* that a magnetically impermeable current sheet was formed. By connecting our scaling parameter to the operational and design parameters of the thruster, we have identified regions of the operating space where this assumption is likely to be invalidated. Specifically, we have found evidence that effective current sheet formation is difficult in regions where both the discharge energy and mass bit are low. This finding is of particular importance for high pulse rate IPPTs, which are expected to operate in this parameter regime, and indicates that many existing models require modifications to accurately predict the performance scaling of these devices.

# Chapter 5

# CONCLUSIONS AND FUTURE WORK

In this dissertation we have discussed the motivations for developing high pulse rate planar IPPTs despite their numerous inherent complexities and reviewed the existing evidence for their viability. Given that data from a high pulse rate planar IPPT had never been reported in the literature, we set out to conduct experiments exploring three fundamental questions related to the operation of these devices. We then detailed the experiments investigating each of these questions in each of the three subsequent chapters of this dissertation. In this final chapter, we summarize the most important findings as well as make recommendations for future research and development efforts based on those findings.

## *5.1 Conclusions*

In the first chapter of this dissertation we laid out three primary research questions to investigate. We may summarize the main findings of our investigation in the context of these questions:

1. **What might a PPU capable of powering a wide range of high pulse rate IPPTs, including those using inductive energy recapture, look like and how might it scale?**

   We have presented a boost-converter based PPU design capable of supporting IPPT operation at pulse rates up to 10 kHz. The PPU was able to supply power up to 10 kW and had sufficient voltage gain to operate an IPPT from a standard spacecraft bus. Unlike previous PPU developed for high pulse rate FRC thrusters (e.g. [36]), the presented design was compatible with IPPT that implement inductive energy recapture. This enhancements was the result of circuitry that isolated the PPU from the discharge circuit except when charging the discharge circuit capacitor banks, which decoupled the charging and discharging processes. Although the electrical efficiency of the constructed prototype was modest, varying between 54% and 70%, we were able to identify the switching losses as the dominant loss mechanism and propose several solutions to improve efficiency. Finally, we were able to show that our PPU architecture could be readily scaled to higher power levels as a result of its highly modular design. We also showed that this modularity resulted in our PPU to possessing inherent redundancy and robustness to component failures.

2. **How does the current sheet evolve, particularly at lower discharge energies?** We investigated current sheet evolution through measurements of a compact planar IPPT with a maximum discharge energy on the order of a few Joules. We found that current sheet evolution in our IPPT could be described by three phases: ionization, formation, and acceleration. Our results indicated that Ohmic heating was essential in overcoming neutral quenching during the formation of the current sheet, which agreed with simulation results reported by Little et al.[31]. In addition, evidence of localization of the plasma current and Ohmic heating towards the upstream edge of the current sheet was found, suggesting the importance of the interplay between Ohmic heating and the skin depth of the plasma to the formation of the current sheet.

   Higher neutral propellant densities were found to cause the current sheet to form closer to the drive coil due to stronger upstream localization of the current and Ohmic heating. This resulted in current sheets that were less permeable to the driving magnetic fields. Meanwhile, our investigation of PI revealed a substantial rise in Ohmic heating of the plasma early in the discharge as PI was increased, which drove faster current sheet formation. Our results also indicated the existence of a threshold degree of PI below which a current sheet could not be formed, providing experimental evidence for the lower bound on the current rise rate that can produce a current sheet suggested by Polzin[23].

3. **What are the fundamental physical processes influencing current sheet formation and how do they scale with the primary thruster operational parameters?**

   Our measurements indicated that the strength of the current sheet scaled with the ratio of the characteristic magnetic diffusion to ionization timescales. This dimensionless parameter was found to describe the competition between resistive diffusion of the magnetic field and ionization of the propellant in concentrating the electron population responsible for the formation of the current sheet. We then showed that it was possible to form a link between the thruster operating and design parameters and the strength of the current sheet. Within the parameter range investigated, the strength of the sheet was found to scale with discharge energy and propellant flow rate and inversely with thruster size, electromagnetic decoupling distance, and propellant ionization energy. We noted, however, that the derived relationship was likely to only apply to a limited range of parameter space.

   The new scaling law presented here addresses a deficiency in the literature in that it describes, for the first time, how the formation of the current sheet itself scales. Previous scaling laws found in the literature largely relied on simplified models of the current sheet and focused on the scaling of thruster performance, assuming *a priori* that a magnetically impermeable current sheet was formed. By connecting our scaling parameter to the operational and design parameters of the thruster, we have identified regions of the operating space where this assumption is likely to be invalidated. Specifically, we have found evidence that effective current sheet formation is difficult in regions where both the discharge energy and mass bit are low. This finding is of particular importance for high pulse rate IPPTs, which are expected to operate in this parameter regime, and indicates that many existing models, e.g. [27, 18, 28, 29], may require modifications to accurately predict the performance scaling of these devices.

## *5.2 Future Work*

Despite the progress made in this work, much remains before high pulse rate planar IPPTs can be considered a viable EP technology. As we close this dissertation, we identify a few avenues for future development of these devices. For a more comprehensive discussion of the current state-of-the-art and possible advancement paths for IPPTs as a whole, the reader is directed to recent work by Polzin et al.[3].

### *5.2.1 PPU Development*

The prototype PPU for high pulse rate IPPTs reported in this work was intended to serve largely as a proof of concept device. Although it is indeed capable of driving a range of high pulse rate IPPTs from nominal spacecraft bus voltages, significant improvements must be made before it could be considered a mature system. For one, the efficiency is notably lower than the PPU used in Hall or gridded ion thrusters. These PPU have achieved efficiencies of close to 95%, while our prototype PPU had a maximum efficiency of 70%. Given that the efficiency of the presented PPU was found to be constrained by large switching losses in the boost cell IGBTs, implementation of soft switching techniques, such as the use of quasi-resonant switch configurations to achieve ZCS or ZVS at turn-off, may be of interest for future prototypes.

In addition, there are a myriad of CCPS topologies reported in the literature[49, 50, 51, 52, 53]. While our literature review and preliminary SPICE simulations suggested that a boost-topology would perform best among the topologies examined, there are many more that were not included in our investigation. Moreover, only the most standard versions of topologies commonly found in the literature were investigated. This is to say that little to no optimization of the considered topologies was performed, and it is possible that some designs may have performed better in our test cases with modifications. As such, future work may seek to determine if better PPU topologies exist by conducting a more exhaustive analysis of existing designs or by attempting to optimize certain designs to the application.

### *5.2.2 Discharge Circuit*

During the course of testing it became clear that one area for improving the performance of our testbed planar IPPTs was the discharge circuit. In particular, two avenues for improvement were identified. The first was the discharge switch. Much like the PPU, a majority of energy losses in the discharge circuit appear to stem from switching losses. These switching losses can dissipate a significant fraction of the total discharge energy, particularly at lower discharge energies. Several approaches may be fruitful for reducing switching losses in the discharge circuit. One possibility is to replace the IGBT with faster a SiC MOSFET device. Presently, however, this would require the use of several such devices in series, and possibly also parallel, to withstand the voltage, current, and current rise rate requirements of the IPPT discharge circuit.

Another possibility is the use of magnetic switches, also known as saturable reactors. These devices are commonly employed in pulsed power applications to delay current conduction through the switch until it has fully opened, thereby largely eliminating turn-on switching losses. Work by Owens[48] on a pulse compression circuit for IPPTs showed that it was possible for a magnetic switch to meet the requirements for use in the discharge circuit while also achieving a sufficiently low saturated inductance so as to not precipitously increase the stray inductance. This suggests that a similar approach may be viable in other types of discharge circuits as well.

The second avenue for improvement relates to the topology of the discharge circuit itself. While we, as have many others, used a simple $RLC$ topology for our discharge circuit, there is little reason to believe that this is the optimal discharge circuit topology for a planar IPPT. Pulsed thruster theory has shown that for any given thruster geometry and initial propellant distribution, there exists an optimal discharge current waveform that will maximize the efficiency of the acceleration process[1]. In addition, Jahn provided experimental evidence that the shape of the current waveform had a substantial impact on the structure and acceleration of the current sheet[1]. At present, optimization of the current waveform in planar IPPTs has only been studied within the context of *RLC* discharge circuits, where it was been found that underdamped waveforms yield superior acceleration characteristics. It is possible, however, that non-sinusoidal current waveforms may offer improved dynamical efficiency.

It is evident from both theory and experiment that efficient IPPT operation is likely to require large current rise rates. A key drawback of *RLC*-type discharge circuits for high pulse rate IPPTs is that the discharge energy tends to become coupled to the temporal dynamics. In other words, the current rise rate becomes tied to the discharge energy. This occurs largely because of the capacitor bank, which is related to both the total stored energy and the characteristic frequency of the circuit. While the charging voltage can be used to increase the stored energy independently of the circuit dynamics, there are practical limits to this approach.

One approach to circumvent this limitation may be to use a pulsed power discharge circuit. Owens[48] reported a pulse-compression-ring IPPT discharge circuit. This system was measured to produce 20 kA of peak current with a rise rate of 15 kA/µs at a discharge energy of roughly 100 J. Notably, the charging voltage on the main capacitor bank was only 3.3 kV, which is relatively low for an IPPT with that maximum current and current rise rate. As a point of comparison, we examine the current rise rate in the PIT MK Va. From data in Polzin[23], we estimate this rise rate to be approximately 200 kA/µs. If we scale this by the discharge energy of 4 kJ, this gives $50\,\mathrm{kJ/(\mu s \cdot kJ)}$. Performing a similar analysis for the pulse-compression-ring circuit, we find $150\,\mathrm{kJ/(\mu s \cdot kJ)}$. While crude, this analysis shows that the pulse compression circuit has a much higher current rise rate per unit of discharge energy, suggesting that significantly larger current rise rates could be achieved in high pulse rate IPPTs by adopting a pulsed-power discharge circuit topology.

Finally there is the matter of the method of PI. We chose to use a unique 2-stage PI approach where an RF source was used to initiate gas breakdown and then a small capacitor was discharged through the primary drive coil. Although this method proved effective, it is unlikely to be optimal. In particular, the 2nd stage PI presented a number of known, or at least suspected, drawbacks. First, PI performed by discharging a smaller capacitor through the drive coil was reported by Dailey and Lovberg to push the plasma that it formed away from the coil face[13]. If this is also occurring in our device, then there may be a tradeoff when increasing the PI bank charging voltage. Specifically, while more plasma may be produced as $V_{pi,0}$ is increased, it may be getting pushed further away from the drive coil, resulting in weaker initial coupling.

There are two other known limitations that are due to the parallel connection of the 2nd stage PI capacitor with the main bank. Because of this, the main bank switch must be rated to a voltage that is equal to the sum of the PI and main bank charging voltages, i.e., $V_{pi,0} + V_{mb,0}$. Thus the maximum energy that can be stored on the main bank for a given switch voltage rating is significantly reduced by this PI configuration. Furthermore, the parallel connection causes a portion of the main bank discharge energy to be directed into the 2nd stage PI capacitor, rather than going through the drive coil. This is assuming that the PI capacitor is at a lower voltage than the main bank, but this is usually the case since the PI bank is discharged in advance of the main bank. This redirection of energy reduces the initial current and current rise rate in the drive coil, diminishing the ability of the main discharge to drive current in the plasma.

The downsides associated with the present 2nd stage PI are significant enough to warrant consideration of alternative PI methods. One potential candidate is to connect a high power RF source directly to the drive coil. Due to the higher frequencies at which the RF would operate, this method has the potential advantage of creating a plasma very close to the coil face. Direct RF PI was considered by Feldman and Choueiri[75] for use in a conical IPPT but results were only reported for benchtop operation and a plasma was never generated.

### *5.2.3 Quasi-Steady Operation*

All of the work in this dissertation was performed using either single-shots or short bursts of pulses. Eventually, testing will need to include longer sets of pulses so the behavior of the thruster in true quasi-steady operation can be determined. Theoretical modeling by

McCulloh et al.[71] showed that the properties of the current sheets formed during quasi-steady operation differed from those produced in a static fill case. In addition, the current sheet properties were found to evolve from one pulse to the next for the first six or so pulses in the pulse train. It is therefore of interest to repeat for the quasi-steady case the same measurements used to investigate current sheet formation in the static fill case. The aim here would be to examine how the evolution of the current sheet might change between the first few pulses and to determine if interaction between pulses affects current sheet evolution in any significant way.

For the static-fill cases examined in this dissertation, the issue of propellant injection was largely circumvented. In quasi-steady operation, however, care must be taken to ensure that gas is injected uniformly over the coil face and with an axial distribution that does not lead to low dynamical efficiency. While existing injection schemes may have been sufficient for previous low pulse rate designs, it is unclear whether they can be readily adopted by high pulse rate IPPTs. To answer this question, efforts to map the neutral density profile presented to the coil face performed for pulsed gas injection schemes will likely need to be replicated.

From an engineering standpoint, quasi-steady operation will also require consideration of the thermal loads in the system. In single-shot or burst mode operation, thermal management was of little concern due to the short timescales involved. In quasi-steady operation, however, significant cooling of key components in both the PPU and thruster discharge circuit will likely be required. In addition, consideration of the materials in the thruster will also become important in quasi-steady operation. The thruster face in particular is expected to see a significant radiative heat flux in this mode, which will require careful material selection. The thermal management systems and new materials needed for quasi-steady operation will ultimately add to the overall mass of the system and will need to be accounted for to determine an accurate estimate of the specific power for a practical thruster design.

### *5.2.4 Additional Measurements*

The central role of the electron temperature ($T_e$) in determining the ratio of the characteristic diffusion to ionization timescales was highlighted in section . In this work we used a time-averaged $T_e$ that was obtained by using our measured plasma resistivity in the equation for the Spitzer resistivity. Given the importance of $T_e$, however, it is of interest to obtain a more direct measurement of this value that makes fewer assumptions regarding the state of the plasma. The highly transient nature of the plasma in an IPPT likely prevents or at least complicates the use of techniques commonly used for $T_e$ measurement in EP systems.

Nonetheless, several possibilities remain. One is to use a combination of probes that are able to measure the floating and plasma potentials as functions of time. The difference between these potentials may then be used to estimate $T_e$, although perhaps not with great accuracy. Another possibility is the use of a triple Langmuir probe, which is well suited to measurements of time-varying plasmas since, unlike traditional Langmuir probes, it does not need require a bias voltage sweep. It is unclear, however, whether the electron distribution is Maxwellian during current sheet formation; a necessary condition for the use of a triple probe[76, 77]. Finally, a spectral line ratio method may be employed, particularly if a suitable collisional radiative model can be developed.

In addition to $T_e$, it is also of interest to obtain direct measurements of the electron density in the current sheet ($n_{e,cs}$) as it evolves. These measurements, which could be obtained through non-perturbing methods such as interferometry, would provide support for our interpretation of the current sheet evolution data presented in section 3.4. In particular, measurements of $n_{e,cs}$ would inform our hypotheses regarding the ionization processes occurring in the sheet during the various phases. For example, the importance of resonant charge exchange is expected to increase as the ions in the sheet encounter downstream neutrals as the sheet begins to translate. A measurement of the time-variance in $n_{e,cs}$ during the acceleration phase could thus help determine whether ionization or charge exchange is the dominant factor increasing the mass of the sheet in this phase. This, in turn, could aid in the understanding of how the transparency of the sheet to downstream mass evolves as it is accelerated and would provide a useful point of comparison to theoretical modeling predictions, e.g. those of Little et al.[31].

The results in this dissertation provide significant insight into the range of operational parameters over which an impermeable current sheet may be formed. Current sheet formation, however, is only one item on the list of requirements for an efficient IPPT. Moreover, simply forming a magnetically impermeable current sheet does not, on its own, equate to high thrust efficiency. Even in the ideal case where the current sheet is perfectly impermeable, the thruster efficiency can still be low due to dynamical inefficiencies in the acceleration process[1]. In addition, practical factors such as propellant mass utilization must also be taken into account. This is to say that even if a current sheet is formed and accelerated efficiently, it must also have done so while capturing the vast majority of the injected propellant.

Ultimately, performance measurements of high pulse rate IPPTs will be required to determine their practicality. In particular, thrust stand measurements in a suitable vacuum environment will be needed. Given the 1 10kW power range of interest, it is anticipated that the propellant flow rates during these tests will be relatively high. If the IPPT is to be operated in true steady-state, a vacuum facility with large pumping speeds will be needed if excessive facility effects are to be avoided. One possible alternative is to operate the thruster in a "burst mode", wherein the thruster is fired for just long enough that quasi-steady state behavior is achieved. Theoretical work by McCulloh et al.[71] has suggested that this may occur after 6 to 8 pulses in a planar IPPT, indicating that a burst of tens of pulses could be sufficient to achieve this goal. For a sufficiently large chamber, operation in a burst mode could keep the pressure in the chamber low enough that facility effects may be kept to a tolerable amount. As a result, burst mode operation could allow the testing of moderate power, high pulse rate IPPTs in chambers of modest pumping speed.

# BIBLIOGRAPHY

[1] R G Jahn. *Physics of Electric Propulsion.* McGraw-Hill, New York, 1968.

[2] D M Goebel and I Katz. *Fundamentals of electric propulsion: ion and Hall thrusters*, volume 1. John Wiley & Sons, 2008.

[3] Kurt Polzin, Adam Martin, Justin Little, Curtis Promislow, Benjamin Jorns, and Joshua Woods. State-of-the-art and advancement paths for inductive pulsed plasma thrusters. *Aerospace*, 7(8):105, 2020.

[4] Joshua L Rovey, Christopher T Lyne, Alex J Mundahl, Nicolas Rasmont, Matthew S Glascock, Mitchell J Wainwright, and Steven P Berg. Review of multimode space propulsion. *Progress in Aerospace Sciences*, 118:100627, 2020.

[5] James Gilland. Mission impacts of in-situ propellant usage for electric propulsion vehicles. In *41st AIAA/ASME/SAE/ASEE Joint Propulsion Conference & Exhibit*, page 4267, 2005.

[6] Tony Schönherr, Kimiya Komurasaki, Francesco Romano, Bartomeu Massuti-Ballester, and Georg Herdrich. Analysis of atmosphere-breathing electric propulsion. *IEEE Transactions on Plasma Science*, 43(1):287–294, 2014.

[7] Peng Zheng, Jianjun Wu, Yu Zhang, and Biqi Wu. A comprehensive review of atmosphere-breathing electric propulsion systems. *International Journal of Aerospace Engineering*, 2020:1–21, 2020.

[8] K A Polzin. Comprehensive review of planar pulsed inductive plasma thruster research and technology. *Journal of Propulsion and Power*, 27(3):513–531, 2011.

[9] C Dailey. Plasma properties in an inductive pulsed plasma accelerator. In *6th Biennial Gas Dynamics Symposium*, page 637, 1965.

[10] CL Dailey. Investigation of plasma rotation in a pulsed inductive accelerator. *AIAA Journal*, 7(1):13–19, 1969.

[11] C L Dailey and R H Lovberg. Current sheet structure in an inductive-impulsive plasma accelerator. *AIAA Journal*, 10(2):125–129, 1972.

[12] C L Dailey. Pulsed electromagnetic thruster. Technical Report AFRPL-TR-71-107, TRW Systems Group, Redondo Beach, CA, 1971.

[13] C L Dailey and H A Davis. Pulsed plasma propulsion technology. Technical Report AFRPL-TR-73-81, TRW Systems Group, Redondo Beach, CA, 1973.

[14] C L Dailey and R H Lovberg. Pulsed inductive thruster component technology. Technical Report AFAL-TR-87-012, TRW Space and Technology Group, Redondo Beach, CA, 1987.

[15] C L Dailey and R H Lovberg. The PIT MkV pulsed inductive thruster. Technical Report NASA CR 191155, TRW Space & Technology Group, Redondo Beach, CA, 1993.

[16] K A Polzin. *Faraday accelerator with radio-frequency assisted discharge (FARAD)*. PhD thesis, Princeton University, 2006. Thesis number 3147-T.

[17] A K Martin, A Dominguez, R H Eskridge, K A Polzin, D P Riley, and K A Perdue. Design and testing of a small inductive pulsed plasma thruster. In *34th International Electric Propulsion Conference*, 2015. IEPC paper 2015-50.

[18] R H Lovberg and C L Dailey. Large inductive thruster performance measurement. *AIAA Journal*, 20(7):971–977, 1982.

[19] J H Poylio, D Russell, W Goldstein, B Jackson, R H Lovberg, and C L Dailey. Pulsed inductive thruster: Flight-scale proof of concept demonstrator. In *40th AIAA/ASME/SAE/ASEE Joint Propulsion Conference & Exhibit*, 2004. AIAA paper 2004-3640.

[20] R Joseph Cassady, Robert H Frisbee, James H Gilland, Michael G Houts, Michael R LaPointe, Colleen M Maresse-Reading, Steven R Oleson, James E Polk, Derrek Russell, and Anita Sengupta. Recent advances in nuclear powered electric propulsion for space exploration. *Energy Conversion and Management*, 49(3):412–435, 2008.

[21] R H Lovberg and C L Dailey. A PIT Primer. Technical Report TR 005, RLD Associates, Lebanon, PA, 1994.

[22] E Y Choueiri and K A Polzin. Faraday acceleration with radio-frequency assisted discharge. *Journal of Propulsion and Power*, 22(3):611–619, 2006.

[23] K A Polzin. Scaling and systems considerations in pulsed inductive plasma thrusters. *IEEE Transactions on Plasma Science*, 36(5):2189–2198, 2008.

[24] Pavlos G Mikellides and Chris Neilly. Modeling and performance analysis of the pulsed inductive thruster. *Journal of propulsion and power*, 23(1):51–58, 2007.

[25] P G Mikellides and N Ratnayake. Modeling of the pulsed inductive thruster operating on ammonia propellant. *Journal of Propulsion and Power*, 23(4):854–862, 2007.

[26] P Mikellides and J Villarreal. Numerical modeling of a low energy pulsed inductive thruster. In *44th AIAA/ASME/SAE/ASEE Joint Propulsion Conference & Exhibit*, 2008. AIAA paper 2008-4726.

[27] C Dailey and R Lovberg. Large diameter inductive plasma thrusters. In *14th International Electric Propulsion Conference*, page 2093, 1979.

[28] K A Polzin and E Y Choueiri. Performance optimization criteria for pulsed inductive plasma acceleration. *IEEE Transactions on Plasma Science*, 34(3):945–953, 2006.

[29] K A Polzin, K Sankaran, A G Ritchie, and J P Reneau. Inductive pulsed plasma thruster model with time-evolution of energy and state properties. *Journal of Physics D: Applied Physics*, 46(475201), 2013.

[30] A K Martin. Performance scaling of inductive pulsed plasma thrusters with coil angle and pulse rate. *Journal of Physics D: Applied Physics*, 49(2):025201, 2016.

[31] Justin M Little, Gordon I McCulloh, and Cameron Marsh. Ionization and current sheet formation in inductive pulsed plasma thrusters. *Journal of Applied Physics*, 132(9):093301, 2022.

[32] P G Mikellides and C Neilly. Modeling and performance analysis of the pulsed inductive thruster. *Journal of Propulsion and Power*, 23(1):51–58, 2007.

[33] P G Mikellides and J K Villarreal. High energy pulsed inductive thruster modeling operating with ammonia propellant. *Journal of Applied Physics*, 102(10):103301, 2007.

[34] B X Che, M S Cheng, X K Li, and D W Guo. Physical mechanisms and factors influencing inductive pulsed plasma thruster performance: a numerical study using an extended magnetohydrodynamic model. *Journal of Physics D: Applied Physics*, 51(36):365202, 2018.

[35] J Ziemer, E Cubbin, E Choueiri, Daniel Birx, J Ziemer, E Cubbin, E Choueiri, and Daniel Birx. Performance characterization of a high efficiency gas-fed pulsed plasma thruster. In *33rd Joint Propulsion Conference and Exhibit*, page 2925, 1997.

[36] D Kirtley, J Slough, M Pfaff, and C Pihl. Steady operation of an electromagnetic plasmoid thruster. In *7th Joint Army-Navy-NASA-Air Force (JANNAF) Spacecraft Propulsion Subcommittee Meeting*, 2011.

[37] J Slough, D Kirtley, and T Weber. Pulsed plasmoid propulsion: The elf thruster. In *31st International Electric Propulsion Conference*, 2009. IEPC paper 2009-265.

[38] T Weber. *The electrodeless Lorentz force thruster experiment.* PhD thesis, University of Washington, 2010.

[39] D Kirtley, J Slough, M Pfaff, and C Pihl. Steady operation of an electromagnetic plasmoid thruster. In *7th JANNAF Spacecraft Propulsion Subcommittee Meeting*, 2011.

[40] D Kirtley, A Pancotti, J Slough, and C Pihl. Steady operation of an FRC thruster on martian atmosphere and liquid water propellants. In *48th AIAA/ASME/SAE/ASEE Joint Propulsion Conference & Exhibit*, 2012. AIAA paper 2012-4071.

[41] D Kirtley, J Pihl, and C Pihl. Development of a steady operating pulsed power system for FRC and inductive thrusters. In *33rd International Electric Propulsion Conference*, 2013. IEPC paper 2013-361.

[42] D Kirtley, J Pihl, B Bernhard, and J Goff. Development, vibration, and thermal characterization of a steady operating pulsed power system for FRC thrusters. Technical Report AFRL-RQ-ED-TP-2015-139, Air Force Research Laboratory, Edwards AFB, CA, 2015.

[43] M R Patel. *Spacecraft Power Systems.* CRC press, Boca Raton, FL, 2004.

[44] Robert G Jahn and Edgar Y Choueiri. Encyclopedia of physical science and technology. *Academic Press*, 3:125–141, 2002.

[45] Curtis Promislow and Justin Little. Operation and performance of a power processing unit for inductive pulsed plasma thrusters operating at high repetition rates. *IEEE Transactions on Plasma Science*, 50(9):3065–3076, 2022.

[46] A K Martin and R H Eskridge. Electrical coupling efficiency of inductive plasma accelerators. *Journal of Physics D: Applied Physics*, 38(23):4168–4179, 2005.

[47] I Hrbud, M LaPointe, R Vondra, C L Dailey, and R Lovberg. Status of pulsed inductive thruster research. In *AIP Conference Proceedings*, volume 608, pages 627–632, 2002.

[48] T L Owens. A pulse-compression-ring circuit for high-efficiency electric propulsion. *Review of Scientific Instruments*, 79(3):034701, 2008.

[49] Aaron C Lippincott and Robert M Nelms. A capacitor-charging power supply using a series-resonant topology, constant on-time/variable frequency control, and zero-current switching. *IEEE Transactions on Industrial Electronics*, 38(6):438–447, 1991.

[50] M M McQuage, V P McDowell, F E Peterkin, and J A Pasour. High power density capacitor charging power supply development for repetitive pulsed power. In *Power Modulator Symposium, 2006. Conference Record of the 2006 Twenty-Seventh International*, pages 368–371. IEEE, 2006.

[51] P K Bhadani. Capacitor-charging power supply for laser pulsers using a boost circuit. *Review of Scientific Instruments*, 60(4):605–607, 1989.

[52] Ankur Patel, KV Nagesh, Tanmay Kolge, and DP Chakravarthy. Design and development of repetitive capacitor charging power supply based on series-parallel resonant converter topology. *Review of Scientific Instruments*, 82(4):045111, 2011.

[53] Hong-Je Ryoo, Suk-Ho Ahn, Ji-Woong Gong, and Sung-Roc Jang. Design and comparison of capacitor chargers for solid-state pulsed power modulator. *IEEE Transactions on Plasma Science*, 41(10):2675–2683, 2013.

[54] Kuang Sheng, Barry W Williams, and Stephen J Finney. A review of IGBT models. *IEEE Transactions on Power Electronics*, 15(6):1250–1266, 2000.

[55] HB Brooks. Design of standards of inductance and the proposed use of model reactors in the design of air-core and iron-core reactors. *Bureau Standards J. Res*, 7:298–328, 1931.

[56] Semiconductor Devices—Discrete Devices—Part 9. IEC 60747-9: Insulated-gate bipolar transistors (IGBTs). *IEC Standard*, pages 60747–9, 2007.

[57] Fred C Lee. High-frequency quasi-resonant converter technologies. *Proceedings of the IEEE*, 76(4):377–390, 1988.

[58] Gang Yao, Alian Chen, and Xiangning He. Soft switching circuit for interleaved boost converters. *IEEE Transactions on Power Electronics*, 22(1):80–86, 2007.

[59] Dominic Gerber and Jürgen Biela. 40kW, 3kV soft-switching boost converter for ultra precise capacitor charging. In *Proc. of the 4th Euro-Asian Pulsed Power Conference*, 2012.

[60] Curtis L Promislow and Justin M Little. Current sheet evolution in a planar inductive pulsed plasma thruster. *Journal of Physics D: Applied Physics*, 57(20):205205, 2024.

[61] Steven P Berg and Joshua L Rovey. Assessment of high-power electric multi-mode spacecraft propulsion concepts. In *33rd International Electric Propulsion Conference*, 2013.

[62] T E Markusic. *Current Sheet Canting in Pulsed Electromagnetic Accelerators.* PhD thesis, Princeton University, 2002. Thesis number 3102-T.

[63] RH Lovberg. Investigation of current-sheet microstructure. *AIAA Journal*, 4(7):1215–1222, 1966.

[64] Kurt A Polzin, Ashley K Hallock, Kamesh Sankaran, and Justin M Little. *Circuit Modeling of Inductively-Coupled Pulsed Accelerators.* CRC Press, 2022.

[65] Cameron Marsh. *Diagnostics and Exploration of Current Sheet Formation in the High-Pulse-Rate Pulsed Inductive Thruster (HiPeR-PIT).* University of Washington, 2022.

[66] Kurt A Polzin, Carrie S Hill, Peter J Turchi, Rodney L Burton, Sarah Messer, Ralph H Lovberg, and Ashley K Hallock. Recommended practice for use of inductive magnetic field probes in electric propulsion testing. *Journal of Propulsion and Power*, 33(3):659–667, 2017.

[67] Heinz E Knoepfel. *Magnetic fields: a comprehensive theoretical treatise for practical use.* John Wiley & Sons, 2008.

[68] Norden E Huang, Zhaohua Wu, Steven R Long, Kenneth C Arnold, Xianyao Chen, and Karin Blank. On instantaneous frequency. *Advances in adaptive data analysis*, 1(02):177–229, 2009.

[69] Arvindh R Sharma, Curtis L Promislow, and Justin M Little. Rotating spokes and self-organization in an inductive pulsed plasma thruster. *Plasma Sources Science and Technology*, 32(2):025008, 2023.

[70] TE Markusic, EY Choueiri, and JW Berkery. Measurements of current sheet canting in a pulsed electromagnetic accelerator. *Physics of plasmas*, 11(10):4847–4858, 2004.

[71] Gordon I McCulloh, Curtis L Promislow, Cameron W Marsh, and Justin M Little. Modeling and testing a compact planar inductive pulsed plasma thruster in a finite neutral backfil. In *37th International Electric Propulsion Conference*, pages IEPC paper IEPC–2022–563, 2022.

[72] Ashley K Hallock, Edgar Y Choueiri, and Kurt A Polzin. Current sheet formation in a conical theta pinch faraday accelerator with radio-frequency assisted discharge. In *30th International Electric Propulsion Conference*, number IEPC-2007-165, 2007.

[73] Michael A Lieberman and Alan J Lichtenberg. *Principles of Plasma Discharges and Materials Processing*. John Wiley & Sons, 2005.

[74] R H Lovberg, B R Hayworth, and T Gooding. The use of a coaxial plasma gun for plasma propulsion. Technical Report TR AE62-0678, Convair/General Dynamics, San Diego, CA, 1962.

[75] Matthew Feldman and Edgar Choueiri. Single stage faraday accelerator with radio-frequency assisted discharge (ss-farad). In *31st International Electric Propulsion Conference*, 2011. IEPC-2011-220.

[76] Robert B Lobbia and Brian E Beal. Recommended practice for use of langmuir probes in electric propulsion testing. *Journal of Propulsion and Power*, 33(3):566–581, 2017.

[77] Kurt A Polzin, Emma Blumhagen, Alicia C Sherrod, and Trevor Moeller. Behavior of triple langmuir probes in non-equilibrium plasmas. In *AIAA Propulsion and Energy 2019 Forum*, page 3990, 2019.